# Lawrence Berkeley National Laboratory

**Title**
Electron energy spectra, fluxes, and day-night asymmetries of boron-8 solar neutrinos from the 391-day salt phase sno data set

**Permalink**

**Authors**
Aharmim, B.
Ahmed, S.N.
Anthony, A.E.
et al.

**Publication Date**
2005-02-25

# Electron Energy Spectra, Fluxes, and Day-Night Asymmetries of $^8$B Solar Neutrinos from the 391-Day Salt Phase SNO Data Set

B. Aharmim,[5] S.N. Ahmed,[11] A.E. Anthony,[13] E.W. Beier,[10] A. Bellerive,[3] M. Bergevin,[4] S.D. Biller,[9] J. Boger,[2, a]
M.G. Boulay,[7] M.G. Bowler,[9] T.V. Bullard,[15] Y.D. Chan,[6] M. Chen,[11] X. Chen,[6, b] B.T. Cleveland,[9] G.A. Cox,[15]
C.A. Currat,[6] X. Dai,[3, 9] F. Dalnoki-Veress,[3] H. Deng,[10] P.J. Doe,[15] R.S. Dosanjh,[3] G. Doucas,[9] C.A. Duba,[15]
F.A. Duncan,[11] M. Dunford,[10] J.A. Dunmore,[9, c] E.D. Earle,[11] S.R. Elliott,[7] H.C. Evans,[11] G.T. Ewan,[11] J. Farine,[5, 3]
H. Fergani,[9] F. Fleurot,[5] J.A. Formaggio,[15] K. Frame,[9, 3, 7] W. Frati,[10] B.G. Fulsom,[11] N. Gagnon,[15, 7, 6, 9] K. Graham,[11]
D.R. Grant,[3] R.L. Hahn,[2] J.C. Hall,[13] A.L. Hallin,[11] E.D. Hallman,[5] W.B. Handler,[11] C.K. Hargrove,[3] P.J. Harvey,[11]
R. Hazama,[15, d] K.M. Heeger,[6] L. Heelan,[3] W.J. Heintzelman,[10] J. Heise,[7] R.L. Helmer,[14, 1] R.J. Hemingway,[3] A. Hime,[7]
C. Howard,[11] M.A. Howe,[15] M. Huang,[13] P. Jagam,[4] N.A. Jelley,[9] J.R. Klein,[13, 10] L.L. Kormos,[11] M.S. Kos,[7, 11] A. Krüger,[5]
C. Kraus,[11] C.B. Krauss,[11] A.V. Krumins,[11] T. Kutter,[8, 1] C.C.M. Kyba,[10] H. Labranche,[4] R. Lange,[2] J. Law,[4] I.T. Lawson,[4]
K.T. Lesko,[6] J.R. Leslie,[11] I. Levine,[3, e] J.C. Loach,[9] S. Luoma,[5] R. MacLellan,[11] S. Majerus,[9] H.B. Mak,[11] J. Maneira,[11, f]
A.D. Marino,[6, g] N. McCauley,[10] A.B. McDonald,[11] S. McGee,[15] G. McGregor,[9, g] C. Mifflin,[3] K.K.S. Miknaitis,[15]
B.A. Moffat,[11] C.W. Nally,[1] M.S. Neubauer,[10, h] B.G. Nickel,[4] A.J. Noble,[11, 3, 14] E.B. Norman,[6, i] N.S. Oblath,[15] C.E. Okada,[6]
R.W. Ollerhead,[4] J.L. Orrell,[15, j] S.M. Oser,[1, 10] C. Ouellet,[11, k] S.J.M. Peeters,[9] A.W.P. Poon,[6] K. Rielage,[15]
B.C. Robertson,[11] R.G.H. Robertson,[15] E. Rollin,[3] S.S.E. Rosendahl,[6, 1] V.L. Rusu,[10, m] M.H. Schwendener,[5] S.R. Seibert,[13]
O. Simard,[3] J.J. Simpson,[4] C.J. Sims,[9] D. Sinclair,[3, 14] P. Skensved,[11] M.W.E. Smith,[15] N. Starinsky,[3, n] R.G. Stokstad,[6]
L.C. Stonehill,[15] R. Tafirout,[5, o] Y. Takeuchi,[11, p] G. Tešić,[3] M. Thomson,[11] M. Thorman,[9] T. Tsui,[1] R. Van Berg,[10]
R.G. Van de Water,[7] C.J. Virtue,[5] B.L. Wall,[15] D. Waller,[3] C.E. Waltham,[1] H. Wan Chan Tseung,[9] D.L. Wark,[12, q]
J. Wendland,[1] N. West,[9] J.F. Wilkerson,[15] J.R. Wilson,[9, r] P. Wittich,[10] J.M. Wouters,[7] A. Wright,[11] M. Yeh,[2] and K. Zuber[9]

(SNO Collaboration)

[1] *Department of Physics and Astronomy, University of British Columbia, Vancouver, BC V6T 1Z1, Canada*
[2] *Chemistry Department, Brookhaven National Laboratory, Upton, NY 11973-5000*
[3] *Ottawa-Carleton Institute for Physics, Department of Physics, Carleton University, Ottawa, Ontario K1S 5B6, Canada*
[4] *Physics Department, University of Guelph, Guelph, Ontario N1G 2W1, Canada*
[5] *Department of Physics and Astronomy, Laurentian University, Sudbury, Ontario P3E 2C6, Canada*
[6] *Institute for Nuclear and Particle Astrophysics and Nuclear Science Division, Lawrence Berkeley National Laboratory, Berkeley, CA 94720*
[7] *Los Alamos National Laboratory, Los Alamos, NM 87545*
[8] *Department of Physics and Astronomy, Louisiana State University, Baton Rouge, LA 70803*
[9] *Department of Physics, University of Oxford, Denys Wilkinson Building, Keble Road, Oxford OX1 3RH, UK*
[10] *Department of Physics and Astronomy, University of Pennsylvania, Philadelphia, PA 19104-6396*
[11] *Department of Physics, Queen's University, Kingston, Ontario K7L 3N6, Canada*
[12] *Rutherford Appleton Laboratory, Chilton, Didcot OX11 0QX, UK*
[13] *Department of Physics, University of Texas at Austin, Austin, TX 78712-0264*
[14] *TRIUMF, 4004 Wesbrook Mall, Vancouver, BC V6T 2A3, Canada*
[15] *Center for Experimental Nuclear Physics and Astrophysics, and Department of Physics, University of Washington, Seattle, WA 98195*

Results are reported from the complete salt phase of the Sudbury Neutrino Observatory experiment in which NaCl was dissolved in the $D_2O$ target. The addition of salt enhanced the signal from neutron capture, as compared to the pure $D_2O$ detector. By making a statistical separation of charged-current events from other types based on event-isotropy criteria, the effective electron recoil energy spectrum has been extracted. In units of $10^6$ cm$^{-2}$ s$^{-1}$, the total flux of active-flavor neutrinos from $^8$B decay in the Sun is found to be $4.94^{+0.21}_{-0.21}$(stat)$^{+0.38}_{-0.34}$(syst) and the integral flux of electron neutrinos for an undistorted $^8$B spectrum is $1.68^{+0.06}_{-0.06}$(stat)$^{+0.08}_{-0.09}$(syst); the signal from $(\nu_x,e)$ elastic scattering is equivalent to an electron-neutrino flux of $2.35^{+0.22}_{-0.22}$(stat)$^{+0.15}_{-0.15}$(syst). These results are consistent with those expected for neutrino oscillations with the so-called Large Mixing Angle parameters, and also with an undistorted spectrum. A search for matter-enhancement effects in the Earth through a possible day-night asymmetry in the charged-current integral rate is consistent with no asymmetry. Including results from other experiments, the best-fit values for two-neutrino mixing parameters are $\Delta m^2 = (8.0^{+0.6}_{-0.4}) \times 10^{-5}$ eV$^2$ and $\theta = 33.9^{+2.4}_{-2.2}$ degrees.

PACS numbers: 26.65.+t, 14.60.Pq, 13.15.+g, 95.85.Ry

## I. INTRODUCTION

Results from the completed second phase of the Sudbury Neutrino Observatory (SNO) [1] are presented in this paper. The second phase began in June of 2001 with the addition of ~2000 kg of NaCl [2] to SNO's ~1000 tonnes of $D_2O$, and ended in October 2003 when the NaCl was removed. The addition of the salt enhanced SNO's ability to detect solar $^8$B neutrinos in three ways. First, the neutron capture efficiency increased by nearly three-fold, allowing a statistically pre-

cise measurement of the neutral-current (NC) disintegration of deuterons by solar neutrinos. Second, the total energy of the $\gamma$-rays from the neutron capture on $^{35}$Cl is 2.32 MeV above the energy of the single $\gamma$ from the capture on deuterons. This higher $\gamma$-ray energy approximately corresponds to a 1 MeV upward shift in the observed energy peak for neutrons and allows a precise measurement that is well above the low energy radioactive backgrounds to be made. Lastly, and perhaps most importantly, the isotropy of the photomultiplier tube (PMT) hit distribution on the geodesic array from multiple $\gamma$-rays emitted after neutron capture on $^{35}$Cl is significantly different from that produced by Cherenkov light emitted by a single relativistic electron. Hence, neutrons from the NC reaction and electrons from the charged-current (CC) interaction can be separated statistically without any assumptions about the underlying neutrino energy spectrum.

Results from the first SNO phase [3–5], using pure $D_2O$ in the target volume, confirmed earlier measurements [6–9] of an observed deficit of solar electron-type neutrino flux compared to solar model expectations [10, 11] but additionally demonstrated, through measurement of the total active $^8$B solar flux, that neutrinos undergo flavor transformation in transit to terrestrial detectors.

Initial measurements of the total active $^8$B solar flux, based on the first 254.2 live days of the salt data set, have been published [12] and confirm and improve on results from the first $D_2O$ phase measurements [3–5]. In particular, the statistical discrimination of CC and NC events with salt enabled an independent measure of the total active $^8$B flux. The measured flux is in very good agreement with solar model calculations [10, 11, 13, 14] .

The favored interpretation of these results is that neutrinos undergo oscillations between flavor states given by linear combinations of the non-degenerate mass eigenstates as described in the Maki-Nakagawa-Sakata-Pontecorvo (MNSP) framework [15]. For the case of $^8$B solar neutrinos, the measurements support the Mikheyev-Smirnov-Wolfenstein (MSW) [16] hypothesis of matter enhanced oscillation, where electron neutrinos experience an additional interaction, compared with muon or tau neutrinos, in the presence of matter that can enhance neutrino oscillations. The SNO data, when combined with other solar neutrino measurements and reactor antineutrino results from the KamLAND experiment [17], show that neutrino oscillations are the dominant cause of flavor transformation and significantly restrict the allowed range of the relevant neutrino mixing parameters.

In terms of neutrino mass and mixing parameters $\Delta m^2$ and $\tan^2 \theta$, solar neutrino data favor the so-called Large Mixing Angle (LMA) region. Maximal mixing is ruled out with a high-degree of confidence.

The present paper extends the analysis to a total of 391 live days of SNO data from the salt phase, provides new results for the integral fluxes, and provides the CC energy spectrum and day-night spectral asymmetries. The values for $\tan^2 \theta$ and $\Delta m^2$ are updated using a two-neutrino oscillation analysis. The paper also provides a more detailed description of the full data analysis process for the SNO salt phase.

The layout of the paper is as follows: Sec. II of the pa-per describes details of the detector hardware and software simulation. The data set, live time determination and event selection are discussed in Sec. III.

The following sections discuss detector response and backgrounds, along with their associated systematic uncertainties on the neutrino measurements. Detailed systematic uncertainty evaluations are presented in the discussions of optical and energy calibration in Sec. IV, event vertex and direction reconstruction and isotropy in Sec. V, and neutron response in Sec. VI. Complete analyses of the many potential background sources are given in Sec. VII followed by the evaluation of specific systematic uncertainties associated with the day-night asymmetry measurement in Sec. VIII.

The procedure for analyzing the solar neutrino signal is discussed in Sec. IX. Solar neutrino results are presented with particular emphasis on the CC energy spectrum with the evaluation of differential energy systematic uncertainties in Sec. X, integral flux in Sec. XI, and day-night asymmetry in Sec. XII. Interpretation of the results in the context of the MSW framework for SNO data only and for the combined solar and reactor analysis can be found in Sec. XIII. A summary provided in Sec. XIV concludes the paper.

## II. SNO DETECTOR AND SIMULATION

### A. Detector

The Sudbury Neutrino Observatory is a real time heavy water Cherenkov detector located in the Inco Ltd., Creighton mine near Sudbury, Ontario, Canada. The center of the detector is at a depth of 2092 m, or 6010 meters of water equivalent. At this depth, approximately 65 muons enter the detector per day. The neutrino target is 1000 tonnes of 99.92% isotopically pure $D_2O$ contained inside a 12-m diameter acrylic vessel (AV). An array of 9456 20-cm Hamamatsu R1408 PMTs, which is mounted on an 18-m diameter stainless steel geodesic structure, is used to detect Cherenkov radiation in the target. A non-imaging light concentrator is mounted on each PMT to increase the effective photocathode coverage by the complete array to approximately 54% of $4\pi$.

To minimize the effects of radioactive backgrounds on the detection of solar neutrinos, materials with low intrinsic radioactivity were selected for the construction of the detector. The acrylic vessel and the geodesic sphere are immersed in ultra-pure $H_2O$ to provide shielding against radioactive backgrounds from the geodesic structure and the cavity rock. An additional 91 PMTs are mounted looking outwards on the geodesic sphere and 23 PMTs are suspended facing inwards in the outer $H_2O$ volume to act as cosmic veto counters. Four PMTs that are installed in the neck region of the acrylic vessel provide veto signals to reject certain classes of instrumental background events (Sec. VII). Further details of the detector can be found in [1]. Note that for analysis purposes Cartesian coordinates are defined such that the center of the vessel is at $(x,y,z) = (0,0,0)$, and the neck region is located symmetrically about the positive $z$ axis.

The SNO experiment detects solar neutrinos through the

charged-current (CC) and neutral-current (NC) interactions on the deuteron, and by elastic scattering (ES) on electrons:

$$\text{CC:} \quad \nu_e + d \rightarrow p + p + e^- - 1.442\,\text{MeV}$$
$$\text{NC:} \quad \nu_x + d \rightarrow p + n + \nu_x - 2.224\,\text{MeV}$$
$$\text{ES:} \quad \nu_x + e^- \rightarrow \nu_x + e^-$$

where $\nu_x$ refers to any active flavor of neutrinos. The NC channel has equal sensitivity to all active neutrinos, while the ES channel is sensitive primarily to electron-neutrinos. Hence, the NC measurement can determine the total active solar neutrino flux even if electron-neutrinos transform to another active flavor [18].

In the first phase of the experiment with pure $D_2O$, NC interactions were observed by detecting the 6.25-MeV $\gamma$-ray following capture of the neutron by the deuteron. For the second phase of data taking, (0.196±0.002)% by weight of purified NaCl was added to the $D_2O$ in May 2001 to increase the capture and the detection efficiencies of the NC neutron. The thermal neutron capture cross section of $^{35}$Cl is 44 b, which is significantly higher than that of the deuteron at 0.5 mb. When a neutron captures on $^{35}$Cl, the total energy released is 8.6 MeV. The combination of the increased cross section and the higher energy released results in a larger neutron detection efficiency at the same analysis threshold.

Neutron capture on $^{35}$Cl typically produces multiple $\gamma$-rays (~2.5 per capture), while the CC and ES reactions produce single electrons. Each $\gamma$-ray predominantly interacts through Compton scattering, producing an energetic electron. The Cherenkov light from neutron capture events, compared to that from CC and ES events, is more isotropic as the light is typically from several electrons rather than one. This greater isotropy, together with the strong directionality of ES events, allows good statistical separation of the event types.

A precise measurement of the total active solar neutrino flux can be made through the NC channel without assumptions about the underlying neutrino energy spectrum. This is relevant because the neutrino energy spectrum can be distorted from the generated $^8$B spectrum via oscillation effects.

### B. SNO Monte Carlo Simulation

The **SNO M**onte Carlo and **an**alysis (SNOMAN) code is used for off-line analysis of the SNO data and provides an accurate model of the detector for simulating neutrino and background events. The Monte Carlo (MC) processor in SNOMAN provides processors for the generation of different classes of events, propagation of the primary particles and any secondary particles (such as Compton electrons) that are created, detection of the signal by the PMTs and simulation of the electronics response. With the exception of a few physics simulations (such as optical photon propagation), widely used packages such as EGS4 [19], MCNP [20] and FLUKA [21] are used in SNOMAN to provide accurate propagation of electromagnetic showers, neutrons, and hadrons.

Detailed models of all the detector components and calibration sources are implemented in SNOMAN. Generators

TABLE I: Tabulation of detector operational status.

| Data | Percentage of run period |
|---|---|
| Detector maintenance, $\nu$ runs rejected by data quality checks, or elevated Rn or $^{24}$Na levels | 22.6 |
| Calibration activities | 20.2 |
| Detector off | 6.2 |
| Selected $\nu$ runs for analysis | 51.0 |

for neutrino and calibration source signals, radioactive backgrounds and cosmic rays are also provided. Input parameters such as optical attenuation coefficients are determined from detector calibration. Calibration and detector parameters are input to SNOMAN and probability density functions (PDFs), used in the neutrino analysis, are generated. These features allow a direct assessment of the systematic uncertainties in physics measurements by comparing the detector responses for various calibration sources with the predictions of SNOMAN.

For the analysis of SNO data, SNOMAN provides various processors to unpack the data, to provide charge and time calibration of the PMT hits for each event, to reconstruct event position and direction, and to estimate the event energy.

### III. DATA SET AND EVENT SELECTION

#### A. Data Set and Live Time

The measurements reported here are based on analysis of 391.432 ± 0.082 live days of data recorded between July 26, 2001 and August 28, 2003. As described below, 176.511 days of the live time were recorded during the day and 214.921 days during the night.

The selection of solar neutrino data runs for analysis is based upon the evaluation of detector operation logs and outputs from an automated off-line data evaluation processor in SNOMAN. The automated processor checks the validity of event times, the trigger thresholds, the status of the electronics channels, and other detector parameters to ensure the quality of the runs selected for analysis. In addition, neutrino runs that are known to have elevated levels of radioactive background were removed from the data set. For instance, some neutrino runs have an elevated level of Rn ingress while others contain residual $^{24}$Na radioactivity resulting from neutron activation during detector calibration.

The bulk of the time that the detector was not live for neutrino data acquisition was used for detector calibration and maintenance activities. Table I provides a tabulation of the detector operational status.

The raw live time of the data set is calculated using a GPS synched 10 MHz clock on a run-by-run basis from the difference in times between the first and last triggered events in each run. These calculated time intervals are verified by comparing

the results against those measured independently with the 50 MHz detector system clock. Separate day and night live times are determined by splitting each run based on solar zenith angle $\theta_z$ where $day \equiv (\cos\theta_z > 0)$ and $night \equiv (\cos\theta_z < 0)$. The ratio of day to night live times is 0.82128 with an uncertainty of less than $5 \times 10^{-7}$.

Several data selection cuts remove small periods of time from the data set. These include time intervals following high-energy cosmic-ray events and intervals containing time-correlated instrumental events To calculate the final live time for the neutrino data set, the total time removed by the full set of data selection cuts is subtracted. Data selection cuts remove a combined total of 1.8% of the raw live time for the neutrino data set. The dominant effect is caused by the cosmic ray veto cut.

The live time calculation, including the corrections due to data selection cuts, is checked with an analysis of data from the detector diagnostic trigger. This pulsed global trigger (PGT) is a detector-wide trigger issued at a frequency of 5Hz based on timing from the 50 MH clock. Systematic uncertainties in live time are evaluated by comparing the PGT measurement to the 10MHz clock measurement, and by analyzing electronics and data acquisition effects that could prevent the detector from being live to neutrino data for short times. The total live time uncertainty is calculated to be $\pm 0.021\%$.

## B. Event Selection

The first step in selecting the solar neutrino candidate events involves the rejection of instrumental backgrounds and residual backgrounds from cosmic rays. A typical data rate was ~20 Hz, which was dominated by low-energy radioactive backgrounds in the detector and the PGT. The primary contributors to the instrumental backgrounds include events generated by static discharge inside the PMTs, known as flashers, events produced when light is emitted from the neck region of the acrylic vessel, known as neck events, and electronic pickup events. The typical combined rate for these events is approximately one per minute compared to the ~10 per day rate of solar neutrino events. These instrumental background events are identified and removed based on analysis of the charge and timing distributions of the triggered PMTs, event geometry in detector and in electronics space, signals from the cosmic veto counter outward-looking PMTs, PMTs installed to identify neck events, and time between events. Additional cuts using reconstruction information, referred to here as "high-level" cuts (Sec. VII), are used to remove events that do not possess the timing and isotropy characteristics of Cherenkov light from either single or multiple $\beta$s.

After the instrumental background and high-level cuts, two cuts are applied to remove cosmic-ray events. The first cut removes events that occur in a 20 s time interval after each event identified as a muon. The principal feature of muon identification is the requirement that there be at least 5 PMT hits in the outward-looking PMTs and 150 PMT hits (equivalent to ~20 MeV) in the inner detector. A second, simpler cut removes any event following within 250 ms of any event with
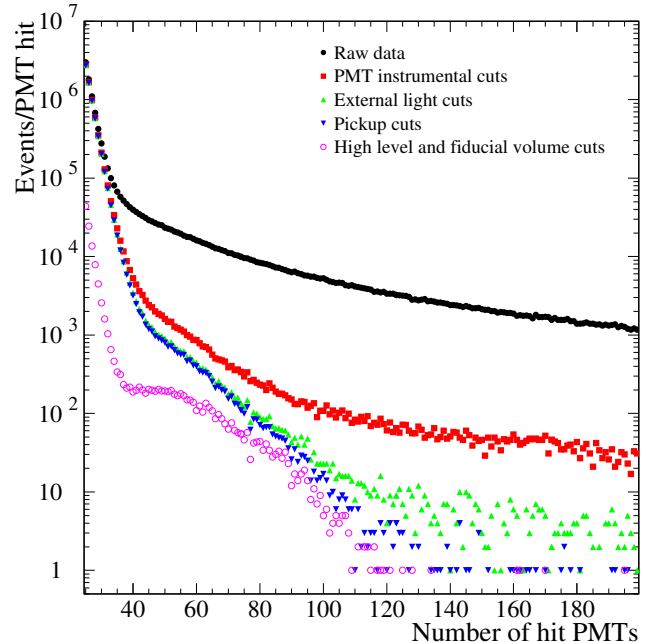


FIG. 1: Reduction of the data set as successive cuts are applied. The PMT instrumental, external light and pickup cuts remove instrumental backgrounds originating from the detector hardware. The high-level cuts (Sec. VII) further reduce the instrumental backgrounds by rejecting events that do not possess the characteristics of Cherenkov light emission from single or multiple $\beta$s. The fiducial volume cut, which selects events reconstructed with $\rho < 0.77$, removes most of the radioactive background events that originate outside the $D_2O$ target.

at least 150 PMT hits. This cut removes neutrons from muons missed by muon identification and neutrons induced by most atmospheric neutrino interactions inside the detector.

The primary background sources are low in energy and external to the $D_2O$ volume. Hence, to minimize the systematic uncertainties associated with backgrounds, all events selected for the results described here are required to have a reconstructed vertex position within 550 cm of the center of the detector. In terms of the volume-weighted variable $\rho \equiv (R/R_{AV})^3$, where $R_{AV}$=600.5 cm is the radius of the acrylic vessel that contains the $D_2O$, the fiducial volume cut is $\rho < 0.77$. Candidate events are required to have an effective electron kinetic energy $T_{eff}$ (see Sec. IV) greater than 5.5 MeV. Details of all background sources are provided in Sec. VII.

The results of sequentially applying the cuts to the data set are shown in Fig. 1. The instrumental cuts are applied in steps to show the removal of various classes of backgrounds. The application of the high-level cuts then reduces the data set further, leaving the set of neutrino candidates. Some of the cuts remove individual events based upon their characteristics, while others remove periods of time from the data set.

TABLE II: Signal loss of the instrumental and high-level cuts for each signal class. These measurements are averaged over the energy spectra above $T_{eff} = 5.5$ MeV. For CC and ES signals an undistorted $^8$B neutrino spectrum has been assumed.

| Signal Class | Signal Loss, % |
|---|---|
| Charged current | $0.57^{+0.16}_{-0.11}$ |
| Neutrons | $0.68^{+0.16}_{-0.11}$ |
| Elastic scattering | $0.86^{+0.21}_{-0.17}$ |

The efficiency of the event-based cuts is measured independently for electron and neutron events. For neutrons, a software tagging approach (Sec. VI) is used to select neutron events from a $^{252}$Cf fission source. These tagged neutron events are then used to measure the efficiency of all cuts. For electrons, the efficiencies of the instrumental cuts and high-level cuts are measured independently. The efficiency of the instrumental cuts is measured using tagged $\beta$ events from a $^8$Li source [22], while 6.13-MeV $\gamma$-rays from a tagged $^{16}$N source [23] are used to measure systematic uncertainties. The efficiency of the high-level cuts is established by MC simulations. Tagged $^{16}$N events are again used to measure systematic uncertainties and corrections. The estimated signal loss for each class of event, integrated over the expected distributions, is shown in Table II.

Signal loss as a function of energy for CC electrons is shown in Fig. 2. This figure shows separately the systematic uncertainties that are correlated between energy bins and those that are independent.

Neutrons produced by cosmic-ray muons and atmospheric neutrinos are used to measure the day-night asymmetry in the cut efficiency. Because muon-induced neutrons are generated throughout the live time of the experiment, they correctly sample any variations in cut efficiency as a function of time. Candidate neutron events are identified by selecting events with a reconstructed vertex radius less than 550 cm, energy in the range from 6 to 10 MeV, and inside a time window between $4\,\mu$s to 40 ms after any muon. Note that the mean neutron capture time is 5.3 ms at the center of the detector and essentially all neutrons are captured by 40 ms.

The instrumental background cuts are applied to produce a clean sample of muon-induced neutrons, and the efficiency of the high-level cuts is estimated for the sample. Alternatively, the high-level cuts are applied and the cut efficiency of the instrumental background cuts on the remaining events is estimated. The loss of neutron events from all cuts, as measured with muon-induced neutrons, is $0.94\pm0.17\%$ and is consistent with the results from neutron calibration sources. The measured day-night asymmetry, defined as the difference between the night and the day signal loss divided by their average, is $0.18 \pm 0.33$.

After all data selection cuts have been applied, including the energy threshold and fiducial volume cuts, 4722 candidate neutrino events remain.
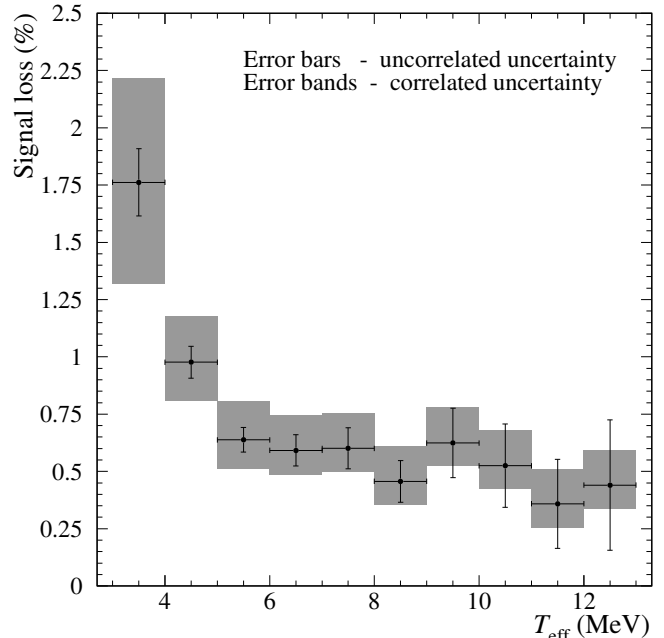


FIG. 2: Signal loss as a function of energy for CC electrons assuming an undistorted $^8$B spectrum. Signal loss uncertainties are divided into two classes: uncorrelated (error bars) and correlated (error bands). Correlated uncertainties arise from systematic uncertainties in the measurement of signal loss and uncorrelated uncertainties arise from statistical uncertainties in the calibration data used in this measurement.

## IV. DETECTOR CALIBRATION

Interpretation of SNO's signals requires measurement and calibration of the detector components and response. Many of the details of the calibration of the detector components are described in [1] and will not be discussed here.

A variety of calibration sources are deployed in the heavy and light water regions to characterize the detector response. Source deployment is achieved with a manipulator system [1] that is able to maneuver sources to various positions in two orthogonal planes within the $D_2O$ and along 6 vertical lines in the $H_2O$. The positional accuracy of the manipulator system is ~2 cm along the central axis and ~5 cm off-axis in the $D_2O$. In the $H_2O$ the accuracy is ~2 cm.

Table III lists the primary calibration sources used. These include pulsed nitrogen laser light for optical calibration and PMT timing, $^{16}$N $\gamma$-rays to produce a reliable energy calibration, $^8$Li for energy and reconstruction calibration, a $^3$H$(p, \gamma)^4$He source ("pT source") to test linearity of the energy scale, $^{252}$Cf and Am-Be sources of neutrons, and U, Th, Rn, neutron activated $^{24}$Na, and $^{88}$Y to test detector response to backgrounds. Note that the "Rn spike" was a controlled release of a measured quantity of Rn gas into the $D_2O$.

The following section describes the optical and energy cal-

ibrations and our evaluation of the systematic uncertainties associated with these assessments. Later sections provide details on event reconstruction, and determination of the detector response to neutrons and backgrounds.

TABLE III: Primary calibration sources.

| Calibration source | Details | Calibration | Ref. |
|---|---|---|---|
| Pulsed nitrogen laser | 337, 369, 385, 420, 505, 619 nm | Optical & timing calibration | [1] |
| [16]N | 6.13-MeV $\gamma$-rays | Energy & reconstruction | [23] |
| [8]Li | $\beta$ spectrum | Energy & reconstruction | [22] |
| [252]Cf | neutrons | Neutron response | [1] |
| Am-Be | neutrons | Neutron response | |
| [3]H($p, \gamma$)[4]He ("pT") | 19.8-MeV $\gamma$-rays | Energy linearity | [24] |
| U, Th | $\beta - \gamma$ | Backgrounds | [1] |
| [88]Y | $\beta - \gamma$ | Backgrounds | |
| Dissolved Rn spike | $\beta - \gamma$ | Backgrounds | |
| *In-situ* [24]Na activation | $\beta - \gamma$ | Backgrounds | |

### A. Optical Calibration

The detector optical response parameters are required for MC simulations and for the energy reconstruction processor. The optical parameters are determined by analyzing the detector response to photons generated with a pulsed nitrogen laser. Laser light is transmitted from the laser through optical fibers to a diffusing ball that can be positioned at various locations in the detector.

A complete optical scan typically consists of measurements taken at approximately $\sim$ 40 different positions and at six wavelengths (337, 369, 385, 420, 505, and 619 nm). This set of wavelengths spans SNO's detectable Cherenkov light spectrum.

The laser plus diffuser ball system produces short (0.8 ns) pulses of light in the detector. For any given position of the diffuser ball, the PMT array measures a time distribution of light. The difference between the measured time of each PMT hit and the expected time-of-flight from the source position to PMT is called the "time-residual." The time-residual distribution exhibits a large peak originating from "prompt", or unscattered, light. The full width at half maximum of this peak, after all timing corrections have been applied, is $\sim$ 1.8 ns. Smaller peaks occur between 10 and 100 ns later. These "late" peaks arise from light reflected from various surfaces within the detector and from late pulsing of the PMTs. The optical model analysis is restricted to a $\pm4$ ns window centered on the prompt peak to reduce sensitivities to the complicated structure of the late light distribution. Additional analyses with a $\pm10$ ns prompt peak window are conducted to verify the results and evaluate sensitivities to the timing window cut.

The optical model is used to predict the number of prompt PMT counts in each laser calibration run based on operational parameters of the laser source and the detector optical parameters. The relevant operational parameters of the laser source are its light intensity and angular distribution. The optical parameters of the detector are the $D_2O$ attenuation length, the combined acrylic and $H_2O$ attenuation length, and the relative efficiency of the PMT-reflector assembly as a function of incidence angle. These optical parameters are extracted by fitting the data collected during a multi-position scan in the $D_2O$ using a $\chi^2$ minimization method. Note that the fits return the inverse of the attenuation lengths or "attenuation coefficients". This technique is not sensitive to the separate AV and $H_2O$ attenuation coefficients, only the combined AV+$H_2O$ attenuation coefficients. The AV attenuation coefficients, given in Table IV, were obtained from *ex-situ* measurements [25]-[26] and the $H_2O$ attenuation coefficients are determined from the difference between the AV attenuation coefficients and the measured sum.

TABLE IV: Acrylic vessel attenuation coefficients.

| Wavelength (nm) | Attenuation coefficient ($10^{-3}$ cm$^{-1}$) |
|---|---|
| 337 | 56.4 |
| 369 | 23.0 |
| 385 | 12.2 |
| 420 | 7.70 |
| 505 | 7.09 |
| 619 | 7.09 |

The measured $D_2O$ and $H_2O$+acrylic attenuation coefficients include the effect of Rayleigh scattering which removes a fraction of the light from the prompt time window. Because the MC simulation must model both absorption and scattering, the scattering contribution is subtracted from the measured coefficient and the resulting absorption coefficient is used as an input to the MC. The scattering coefficient is determined using laserball data taken with a collimating mask over the ball and measuring the hit probabilities for PMTs outside of the angular acceptance of the collimated beam.

Figure 3 shows sample $D_2O$ and $H_2O$ attenuation coefficients, measured at 369 nm and 420 nm respectively, for six scans taken during the salt phase. The $H_2O$ coefficients are constant within the accuracy of the measurements, while the $D_2O$ values exhibit a steady increase until late in the salt phase. For both MC simulation and energy reconstruction, the $D_2O$ attenuation coefficients are determined, based on the date at which the given run was taken, from a linear fit to the measured attenuation coefficients as a function of time.

Chemical assays of the $D_2O$ indicate that the change in attenuation can be attributed to trace levels of contaminants. In particular, the possible presence of organic complexes in the salt phase, as well as measured increases in Mn contamination, likely associated with the $MnO_X$ assays discussed below, are correlated with the increase in the attenuation coefficients. As described below, the changing response was independently measured by the laser and the [16]N sources, and was corrected for in the data processing. Following desalination by reverse osmosis and water purification after completion of the salt phase, the attenuation levels returned to those measured in June 2000 prior to salt deployment.

In addition to the attenuation coefficients, the relative average response of the PMT-reflector assemblies as a function of photon incidence angle is measured. A typical angular re-
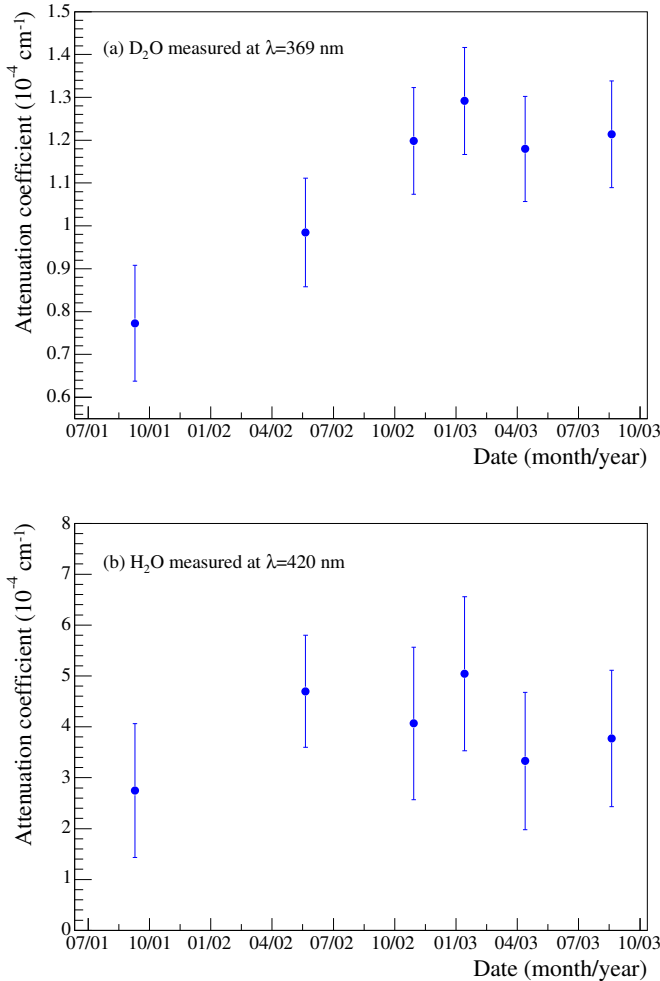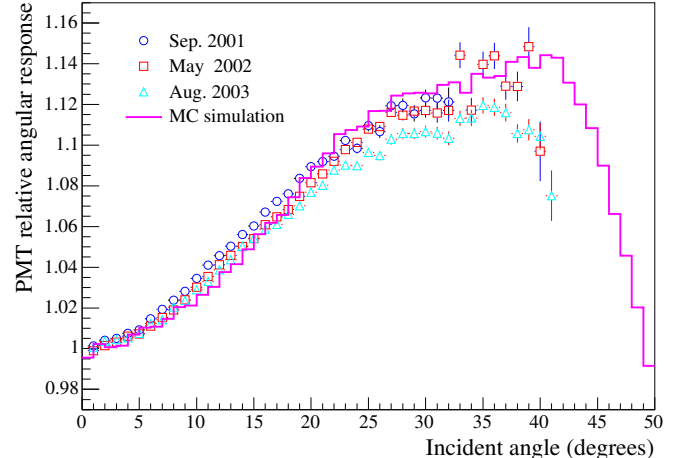
FIG. 4: Measured angular response curves for PMT-reflector assemblies from three optical scans taken at 385 nm during the salt phase of operation. The incident angle for photons originating from the fiducial volume ($\rho < 0.77$) is confined to less than 35 degrees. The average response from all the laser scans is used as the input to the MC simulation. Note that the y axis zero is suppressed.

FIG. 3: Attenuation coefficients of (a) $D_2O$ and (b) $H_2O$ as a function of date for 369 and 420 nm pulsed laser scans. The data points are correlated by systematics that are common to each of the measurements. Note that the $H_2O$ values are determined by subtracting the acrylic vessel *ex-situ* measured attenuation coefficients from the measured $H_2O$+acrylic values.

sponse distribution, given in Fig. 4, presents angular response measurements for 385-nm light from three laser scans taken during the salt phase. The response is normalized to unity at normal incidence angle and, as can be seen, the response increases by $\sim 12\%$ at $35°$. The angular response curves are reasonably constant over the salt running period and the average of the response functions from all laser scans is used as input to the MC simulation and the energy reconstruction.

### B. Energy Calibration

Once the optical calibration constants are determined, the energy calibration and systematic uncertainty evaluations are carried out.

The simplest energy estimator in SNO is the number of PMTs that trigger in an event ($N_{hits}$). However, for a given

event energy, the corresponding mean number of triggered PMTs varies with event position and direction owing primarily to the effects of the $D_2O$, AV, and $H_2O$ attenuation coefficients and the varying PMT angular response.

The late light, described above, is difficult to accurately model. In order to minimize systematic uncertainties associated with the late light, only the number of PMTs that fire within the "prompt" range of $\pm10$ ns centered on the time-residual peak is used to estimate the event energy. Figure 5, produced from $^{16}N$ events generated at the center of the detector, illustrates the shape of a typical time-residual distribution for Cherenkov light.

The number of prompt PMT hits ($N_{prompt}$) is corrected for noise ($N_{noise}$), optical response ($\epsilon_{response}$) relative to response at the detector center ($\epsilon_0$), and for the fraction of working PMTs at the time of the event ($PMT_{working}$) compared to the total number of PMTs ($PMT_{total} = 9456$) to produce the corrected variable $N_{corrected}$:

$$N_{corrected} = \frac{(N_{prompt} - N_{noise})}{\epsilon_{response}/\epsilon_0} \frac{PMT_{total}}{PMT_{working}}. \qquad (1)$$

This is the effective number of prompt PMT hits that would have fired in an ideal detector with the event vertex at the center of the $D_2O$ volume. During the salt phase of operation, the number of working PMTs was generally between 8800 and 8600. The correction for PMT dark noise, measured typically to be ~0.1 hits/event, is small when compared to the average response for 5.0-MeV kinetic energy electrons of ~35 corrected hits/event.

The optical response function corrects for the relative effects of path length through $D_2O$, AV, and $H_2O$ and for incidence angle onto the PMT-reflector assembly compared to an event at the center of the detector. The response function is
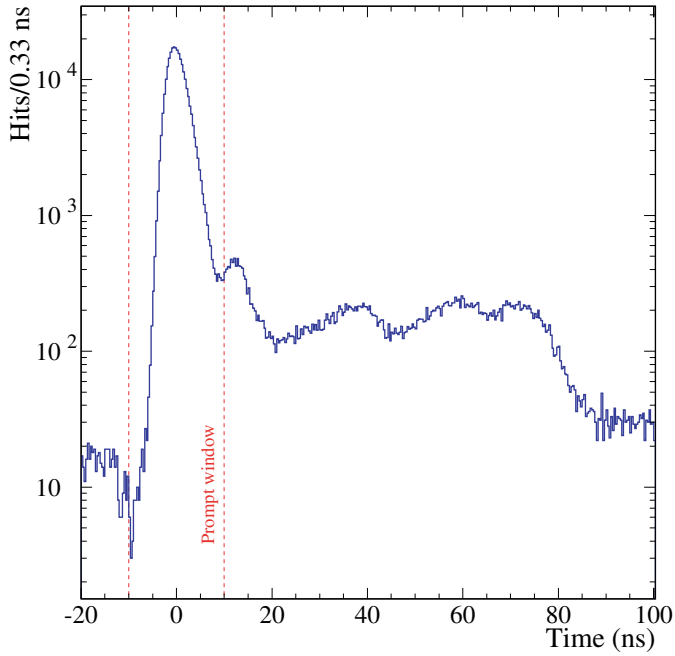
FIG. 5: PMT time-residual spectrum for a $^{16}$N run taken with the source positioned at the center of the detector. The time residual is calculated without any walk correction to the PMT hit time. Only hit PMTs with time residuals within the 20-ns "prompt window" centered at the "prompt peak" are used to estimate the energy of an event.
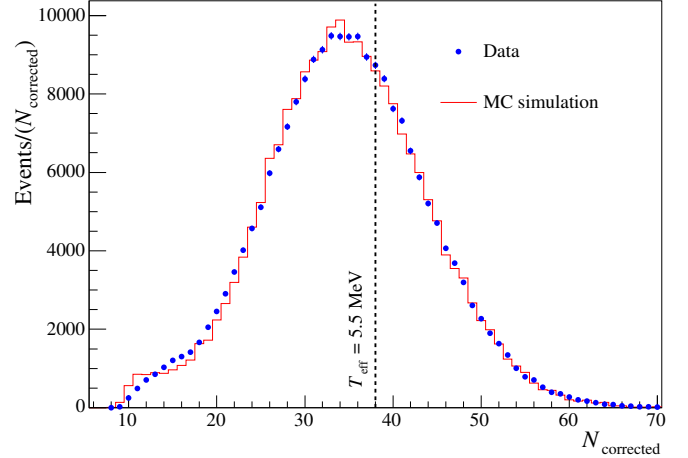


FIG. 6: $N_{\text{corrected}}$ distributions for data (points) and MC (histogram) for a $^{16}$N run taken with the source positioned at the center of the detector. The dashed line corresponds to the energy threshold cut of $T_{\text{eff}} = 5.5$ MeV.

given by

$$
\begin{aligned}
\epsilon_{\text{response}} = & \sum_{\theta'} \sum_{\phi'} \sum_{\lambda} \frac{\epsilon_{PMT}(\lambda)}{\lambda^2} P(r, \theta, \theta', \phi', \lambda) \qquad (2) \\
& \times M(r, \theta', \phi') g(\theta', \phi') e^{-\mu_1 d_1} e^{-\mu_2 d_2} e^{-\mu_3 d_3}
\end{aligned}
$$

where the sums are over 10 polar ($\theta'$) and 10 azimuthal ($\phi'$) angle bins relative to the reconstructed event vertex and direction ($\theta'=0$), and wavelengths $\lambda$ in a range (220-710 nm) that encompasses the wavelengths to which the detector is sensitive. $\epsilon_{PMT}(\lambda)$ is the average wavelength response of the PMT-reflector assembly, $P(r, \theta, \theta', \phi', \lambda)$ represents the angular response function, $g(\theta', \phi')$ the Cherenkov light weighting distribution, $M(r, \theta', \phi')$ a correction for multiple photon hits in the PMTs, and $e^{-\mu_i d_i}$ are $\lambda$ dependent attenuation factors for the three media (1 ≡ D$_2$O, 2 ≡ AV, 3 ≡ H$_2$O).

The next step in the energy calibration is to translate $N_{\text{corrected}}$ into an energy. A combination of data and MC simulated high-rate ($\sim$ 200 Hz) 6.13-MeV $\gamma$-ray events from the $^{16}$N source and MC simulated electrons are utilized for this purpose.

First, MC simulated $^{16}$N events are generated with the source at the center of the detector. The optical constants described above are used as inputs to the simulation, leaving an overall global PMT efficiency factor free which is tuned by matching the mean of the MC simulated $N_{\text{corrected}}$ distribution to the corresponding distribution for $^{16}$N data, as shown in Fig. 6. This sets the MC simulated $N_{\text{corrected}}$ scale to that of the SNO detector.

With the global efficiency set, electron MC events are then generated at a series of fixed energies to produce a "look-up" table that translates $N_{\text{corrected}}$ into equivalent electron kinetic energy $T_{\text{eff}}$.

## C. Systematic Uncertainties

Among the most important systematic uncertainties on the measured fluxes and energy spectra are the detector energy scale and energy resolution uncertainties. Near the analysis energy threshold of $T_{\text{eff}} = 5.5$ MeV, these uncertainties are extracted from comparisons between $^{16}$N data and MC simulations. $^{16}$N data are recorded at regular intervals throughout the salt phase. This consists of approximately monthly deployments at the center of the vessel and periodic scans throughout the $x$-$z$ and the $y$-$z$ planes in the D$_2$O volume. Determinations of energy scale and energy resolution systematics are tested and extended with analyses of $^8$Li source data taken during the salt phase and pT source measurements taken during the D$_2$O phase.

The factor $PMT_{\text{total}}/PMT_{\text{working}}$ in equation 1 directly affects the energy scale and requires accurate identification of PMTs exhibiting normal working behavior. Normal PMT operation is assessed from analysis of PMT charge and timing distributions from high-statistics laser calibration runs. Analysis of PMT occupancy distributions from $^{16}$N data is used evaluate the average fraction of improperly functioning PMTs missed in analysis of the laser data. The estimated energy scale uncertainty associated with misidentification of improperly working PMTs is conservatively estimated to be 0.20%

The energy scale response of the detector is sensitive to the electronic threshold and PMT gain. Cross-talk measurements and the shape of PMT charge distributions are both sensitive to such changes and are evaluated with $^{16}$N calibration data.

Special $^{16}$N runs were taken during the salt phase in which the PMT high voltages were varied, and separately with the data acquisition threshold settings varied, to simulate the effects of gain and threshold changes on the charge and cross-talk distributions. Comparison to the standard set of $^{16}$N data places limits on possible threshold and gain effects on the energy scale of 0.20% and 0.40% respectively.

Differences in the detector response as a function of event rate can directly affect comparisons between $^{16}$N source runs (high-rate) and neutrino data (low-rate). $^{16}$N runs, with the source event rate tuned to simulate the neutrino mode rate, are recorded at approximately monthly intervals. Rate effects are evaluated by comparing low-rate and high-rate $^{16}$N data and are estimated to be less than 0.1%. Additional energy scale uncertainties associated with timing resolution are evaluated to be less than 0.1%.

The data span approximately two years of detector operation. To accurately extract the integral flux and day-night energy spectra, it is critical to evaluate and model the time-dependence of the detector state. As indicated above, the D$_2$O attenuation coefficients increased slowly throughout most of the salt phase.

For each $^{16}$N data and MC simulated run, estimates of the mean and width of the $N_{corrected}$ and energy distributions are generated by fitting a Gaussian function to the central portion of the spectra. Figure 7 shows the distributions of mean $N_{corrected}$ and reconstructed energy as functions of date for $^{16}$N runs with the source positioned at the center of the detector. The MC simulated runs have been generated with D$_2$O attenuation coefficients increasing as shown in Fig. 3. As is seen, the decreasing MC simulated response in $N_{corrected}$ matches the slope observed in the $^{16}$N data.

During the final period of the salt phase, no MnO$_X$ assay (Sec. VII) was taken and measurements indicate that the detector energy response also ceased to change. The mean energy distributions shown in Fig. 7(b) have been corrected for the changing attenuation. The run-by-run differences between data and MC simulation mean and width estimates are taken as the temporal stability systematic uncertainties on energy scale and resolution respectively.

The energy scale uncertainty arising from the temporal stability evaluation is 0.15%. The energy resolution stability uncertainty is determined to be 1.8% and is dominated by an average offset between the data and the MC simulation. This offset is attributed to a combination of effects from electronic cross-talk and from tube-to-tube variation in PMT efficiencies not modeled in the MC simulation.

Modeling the detector and the calibration sources involves a variety of simplifications and uncertainties. For the $^{16}$N source, uncertainties in the $^{16}$N decay branching ratios, minor differences between pure D$_2$O and the salt brine in the production and propagation of Cherenkov light, exact details in describing the source geometries, the finite step size in the EGS4 simulation, neglecting the minor velocity dependencies in the wavelength spectra of Cherenkov light, and the wavelength dependence of the index of refraction are estimated, in total, to contribute a 0.65% systematic uncertainty to the energy scale.
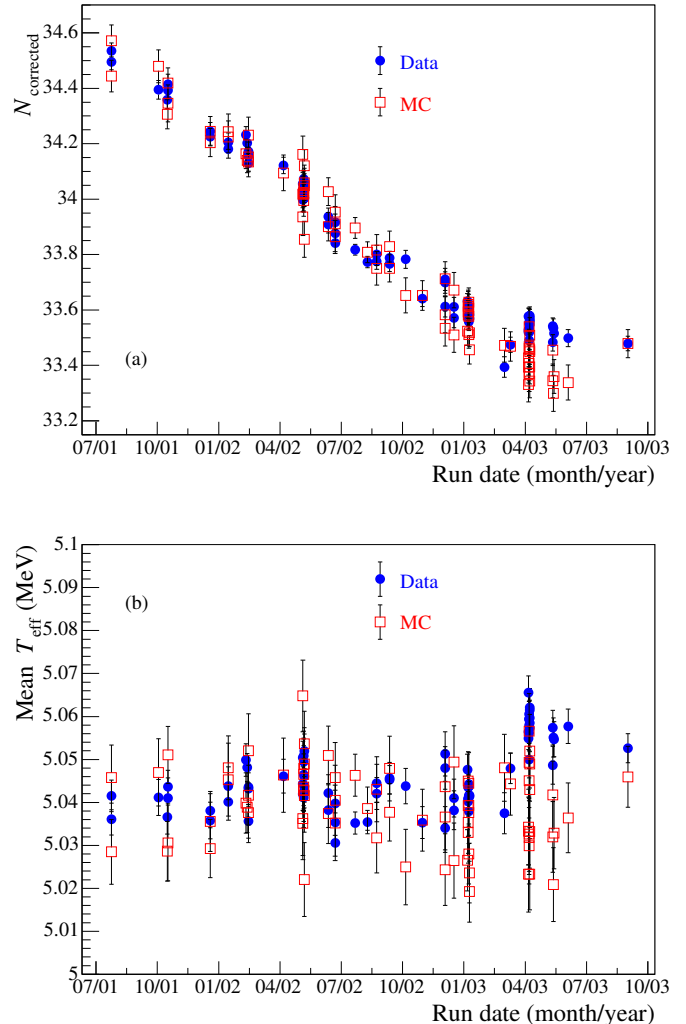


FIG. 7: (a) Mean $N_{corrected}$ and (b) mean $T_{eff}$ versus date for data and MC high-rate $^{16}$N calibrations runs with the source at the center of the detector. Note that the full $y$-axis ranges are ∼ 4% and ∼ 2% of the average $N_{corrected}$ and $T_{eff}$ values respectively. Error bars are statistical only, and the spread of the variation between data and Monte Carlo provides the measure of the energy scale uncertainty arising from temporal variations in detector response.

Significant contributions to the energy scale uncertainty arise from evaluations of the radial response and detector asymmetries. Figure 8 shows data and MC simulation mean energy values and their ratio versus source radial position $\rho$. The volume-weighted mean difference between data and MC simulation of 0.45% is taken as the radial response energy scale uncertainty contribution.

The detector asymmetry component means point-to-point non-uniformities in detector response due to asymmetric detector features such as support ropes and the neck of the AV. It is evaluated by determining the volume-weighted average standard deviation in each of seven radial bins of the data/MC simulation $T_{eff}$ ratio distribution and is calculated to be 0.59%. The corresponding energy resolution radial and de-
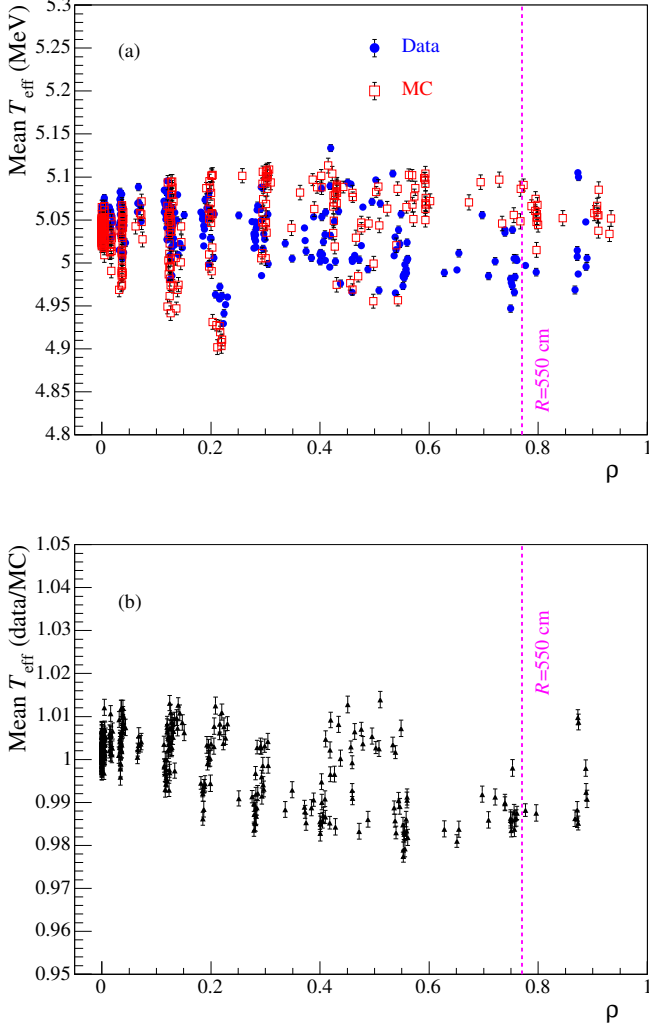
the $^{16}$N source. The effects of cross-talk and noise on the energy scale are estimated to be $< 0.25\%$. The energy resolution uncertainty was determined from pT data to be 10% at 19.8 MeV. Hence the energy resolution uncertainty is applied as the function

$$T_{\text{eff}} < 5 \text{ MeV} \quad : \quad \Delta\sigma_T = 3.4\% \tag{3}$$

$$T_{\text{eff}} > 5 \text{ MeV} \quad : \quad \Delta\sigma_T = [3.4 + 0.478(T_{\text{eff}} - 5)]\%. \tag{4}$$

The energy response for electrons was characterized as a Gaussian function with resolution $\sigma_T = -0.131 + 0.383\sqrt{T_e} + 0.03731 T_e$, where $T_e$ is the true electron kinetic energy in MeV. Table V summarizes all contributions to energy scale and resolution systematic uncertainties. Energy scale contributions are added in quadrature giving a total uncertainty of 1.15%. The radial and detector-asymmetry energy resolution components are added together in quadrature and then added linearly to the data-MC offset to produce a 3.4% total uncertainty.

TABLE V: Summary of energy scale and resolution systematic uncertainties.

| Scale uncertainty | |
|---|---|
| Source | Uncertainty |
| Detector PMT status | 0.20% |
| Electronics threshold | 0.20% |
| Electronics gain | 0.40% |
| Electronics rate effects | 0.10% |
| Time calibration | 0.10% |
| Time drift/stability: data-MC | 0.15% |
| Radial distribution: data-MC | 0.45% |
| Detector asymmetry | 0.59% |
| $^{16}$N source modeling | 0.65% |
| Cross-talk/pickup non-linearity | 0.25% |
| Total | 1.15% |
| Resolution uncertainty | |
| Source | Uncertainty |
| Central $^{16}$N runs: data-MC | 1.8% |
| Detector asymmetry | 1.4% |
| Radial dependence | 0.8% |
| Total | 3.4% |



FIG. 8: (a) Data and MC mean energy versus $\rho$ distributions and (b) the run-by-run ratio of data to MC mean energy versus $\rho$ are shown for $^{16}$N calibration runs. The dashed vertical line corresponds to the fiducial volume cut at $R = 550$ cm. Points at the same value of $\rho$ can have differing energy response in data or Monte Carlo due to local point-to-point non-uniformities in detector response.

tector asymmetry systematic uncertainties are evaluated in an analogous fashion and found to be 1.4% and 0.78% respectively.

These estimates of energy scale and resolution uncertainties are obtained near the detector threshold. The cross-talk and multiphoton effects of higher energy events are probed with high-intensity pulsed laser data. In addition, the pT source, which generates 19.8 MeV $\gamma$-rays, enables a direct test of the higher energy scale systematic uncertainties. However, high-rate of neutrons emanating from the pT source precluded its deployment during the salt phase of the experiment. Comparison of the pure $D_2O$ and salt laser runs indicate no additional unmodeled effects and supports the application of the pT data to the salt data set. It is found that the energy scale uncertainty, evaluated from pT data, is not greater than that evaluated with

## V. EVENT RECONSTRUCTION

For each event, PMT trigger times and positions are used to reconstruct the event vertex, direction, and isotropy. The following sections outline the algorithms and the determination of systematic uncertainties associated with these reconstructed variables.

### A. Event Vertex and Direction

Event positions and directions are reconstructed by analysis of the times and positions of triggered PMTs in each event.

The time-of-flight corrected PMT trigger time is used to define the PMT time-residual

$$T_i^{\mathrm{res}} = t_i - t_{\mathrm{fit}} - \frac{|\vec{r}_{\mathrm{fit}} - \vec{r}_i|}{u_{\mathrm{eff}}} \qquad (5)$$

where $t_i$ and $\vec{r}_i$ are the trigger time and the position of the $i^{th}$ PMT in the event, and $t_{\mathrm{fit}}$ and $\vec{r}_{\mathrm{fit}}$ are the fit time and the reconstructed position of the event vertex. The effective photon velocity, $u_{\mathrm{eff}} = 21.87$ cm/ns, is the group velocity of the mean detected photon wavelength at 380 nm in $D_2O$.

For each event a likelihood is constructed from the PMT time-residual probabilities where MC simulated events are used to derive the reference PDF. The PDF is approximated as a constant for time-residual greater than 15 ns because the time peaks associated with reflected photons strongly depend on the event location. A time cut of ±50 ns relative to the median PMT hit time is imposed to reduce the effects of reflected photons and PMT dark noise. Seed vertices are chosen randomly from the detector volume and the negative log likelihood function is minimized with respect to $t_{\mathrm{fit}}$ and $\vec{r}_{\mathrm{fit}}$ until a global minimum is found.

Event direction is reconstructed independently after the best-fit vertex has been found. It is estimated based on the assumption that the events produce Cherenkov light emitted in the characteristic cone shaped pattern. A likelihood is constructed based on the distribution of directions from the reconstructed event position to the triggered PMTs relative to the corresponding MC calculated distribution for Cherenkov light events. A "prompt" time cut (±10 ns) on the time-residual distribution excludes most Rayleigh scattered and reflected photons. The negative log likelihood is minimized to determine the best fit direction. For multiple electron events the reconstructed direction tends to be weighted towards the direction of the most energetic electron(s) in the event.

Vertex reconstruction uncertainties are evaluated by comparing average reconstructed event positions of $^{16}N$ calibration data with $^{16}N$ MC simulations and by comparing the average reconstructed source position to manipulator estimated position for $^{16}N$ calibration data. The manipulator source position measurement is most accurate when operating in single axis mode along the $z$-axis of the detector. Figure 9 shows the difference between mean reconstructed $x$, $y$, and $z$ positions and manipulator estimated source position as functions of $\rho$. These figures indicate that the $x$ and $y$ vertex reconstruction uncertainties are not more than 2 cm. A larger difference in $z$ is apparent and the $z$ vertex reconstruction uncertainty is taken to be 6 cm.

In addition to coordinate shifts, fiducial volume uncertainty is also evaluated. Radial scaling bias could occur through reconstruction biases or timing calibration uncertainty. Reconstructed radial distributions of events from calibration and neutrino signal data near the AV are compared to MC simulations to evaluate this uncertainty. The radial uncertainty is estimated to be 1.0% of the radius (i.e., 5.5 cm at 550 cm).

Angular response uncertainty is determined from analysis of $^{16}N$ data and $^{16}N$ MC simulated events. The $\gamma$-rays produced by the $^{16}N$ source travel an average of 30 cm in $D_2O$ before a Compton scatter occurs. The vector from the $^{16}N$ $\gamma$-
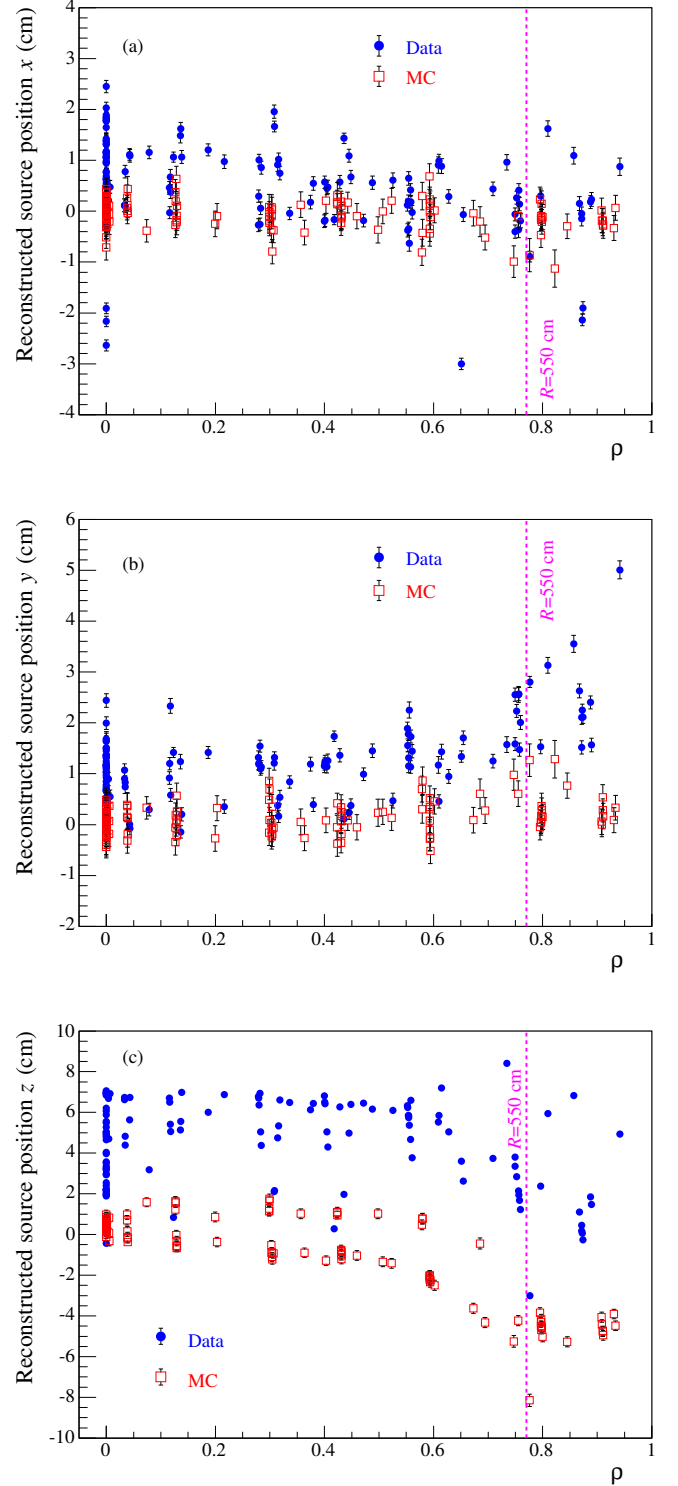


FIG. 9: Difference between mean reconstructed (a) $x$, (b) $y$, and (c) $z$ coordinates and the coordinates of the deployed $^{16}N$ source versus $\rho$. The $^{16}N$ source was deployed along the central ($z$) axis for the data shown in this figure. From these data, systematic uncertainties on $x$ and $y$ coordinate vertex reconstruction are evaluated to be 2 cm and the uncertainty on $z$ coordinate vertex reconstruction is evaluated to be 6 cm.

FIG. 10: Data and MC distributions of the cosine of the angle between generated event direction and reconstructed direction for a $^{16}$N source located at the center of the detector are shown. The events are selected such that the reconstructed vertex is at least 120 cm away from the source position.
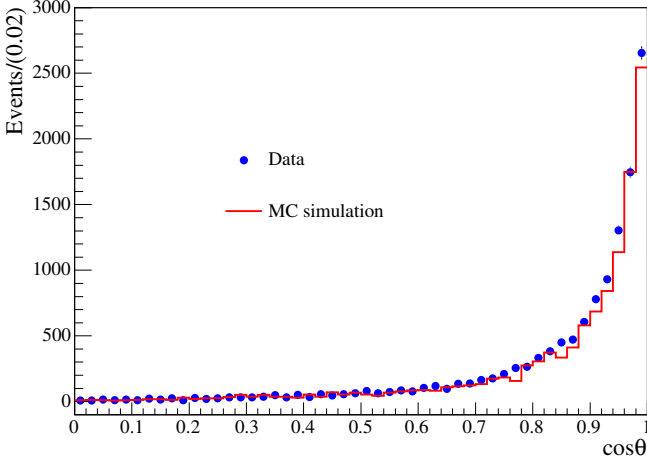
ray source to the reconstructed event vertex provides a good estimate of the generated electron direction, since for events above $T_{\mathrm{eff}} = 5.0$ MeV the Cherenkov light is dominated by that from Compton electrons that are forward-peaked. Gammas that travel at least 120 cm from the source before scattering are employed to ensure the estimate of the event direction is reliable. For each data and MC simulated $^{16}$N run, the distribution of the cosine of the angle $\theta$ between the electron direction and the reconstructed direction is fit with the function

$$R = N[e^{\beta_S(\cos\theta - 1)} + \alpha_M e^{\beta_M(\cos\theta - 1)}] \quad (6)$$

where N is the overall normalization, $\beta_S$ parametrizes the distribution for electrons scattered only a small amount, $\beta_M$ accounts for those scattered through large angles, and the ratio of these components is $\alpha_M$. Shown in Fig. 10 are sample data and MC simulated distributions of $\cos\theta$ for an $^{16}$N run at the center of the detector. The angular resolution systematic uncertainty, determined by comparing the average difference between data and MC simulation fit parameters for all $^{16}$N runs taken during the salt phase, is 16% of $\beta_S$.

## B. Event Isotropy

In the context of SNO event analysis and signal extraction, isotropy refers to the uniformity of the distribution of triggered PMTs on the PMT array.

For data collected during the SNO pure $D_2O$ phase, the CC and ES signal events produced a single primary electron while the NC events produced a single 6.25-MeV capture $\gamma$-ray. For a NC event above $T_{\mathrm{eff}} = 5.0$ MeV the Cherenkov light is dominated by that from a single forward-scattered Compton electron, so all signal event types in the pure $D_2O$ phase had similar isotropy distributions. With salt added to the SNO

detector the characteristic response to neutrons is multiphoton. Event isotropy is measured from the spatial distribution of triggered PMTs and is an effective signal separation tool in this circumstance.

Several variables constructed to measure isotropy are found to have comparable separation power between the single electron (CC and ES) and the neutron (NC) signals. The variable used, which could be simply parameterized and facilitate systematic uncertainty evaluations, is $\beta_{14} \equiv \beta_1 + 4\beta_4$ where

$$\beta_l = \frac{2}{N(N-1)} \sum_{i=1}^{N-1} \sum_{j=i+1}^{N} P_l(\cos\theta_{ij}). \quad (7)$$

In this expression $P_l$ is the Legendre polynomial of order $l$, $\theta_{ij}$ is the angle between triggered PMTs $i$ and $j$ relative to the reconstructed event vertex, and $N$ is the total number of triggered PMTs in the event.

Initial comparisons of the isotropy distributions for $^{16}$N data and MC simulated $^{16}$N showed that the mean value of $\beta_{14}$ for $^{16}$N data was ~2.5% larger than for the $^{16}$N MC simulation. This was caused primarily by approximations used in the description of electron scattering in the MC simulation. Electron transport is handled within the MC simulation by EGS4 [19] in which elastic collisions with atomic nuclei are modeled using Molière's theory of multiple-scattering as formulated by Bethe [27]. This neglects the effect of the spin of the electrons which slightly reduces the amount of large-angle scattering. The MC simulation therefore overestimates the amount of Cherenkov light emitted in the backward hemisphere, producing a light distribution which is slightly too isotropic, i.e., a $\beta_{14}$ slightly too small. There are also other approximations in the treatment of multiple-scattering in EGS4, that affect the distribution, but the effect of spin is the most significant.

Including the effect of spin multiplies the Rutherford cross section by a factor $M(\theta, \beta, Z)$, first calculated by Mott [28], given by [29]:

$$M(\theta, \beta, Z) = 1 - \beta^2 \sin^2\frac{\theta}{2} + \pi\beta\frac{Ze^2}{\hbar c}\sin\frac{\theta}{2}(1 - \sin\frac{\theta}{2}), \quad (8)$$

where $\theta$ is the single scattering angle, $\beta$ is the electron speed divided by $c$, and $Z$ is the charge of the scattering nucleus. In EGS4, an electron is propagated a step length $x$ at which point its direction is changed by an angle $\varphi$. This angle is drawn from a probability density distribution for electrons multiple-scattered by a screened Coulomb potential without the Mott terms. A simple MC program was written to evaluate the probability density distributions with and without the Mott terms, and correction constants were generated giving the amount $\Delta\varphi$ to be subtracted from the EGS4 angle $\varphi$ for a number of different step lengths and electron kinetic energies. For large angles the correction is approximately step length independent and close to that obtained when assuming single scattering dominates, while for small angles and longer step lengths it is smaller.

This correction to the EGS4 multiple-scattering angles was parameterized as a function of energy using the average EGS4 step length for a given energy. The fraction of electrons that scatter into the forward hemisphere after passing through a
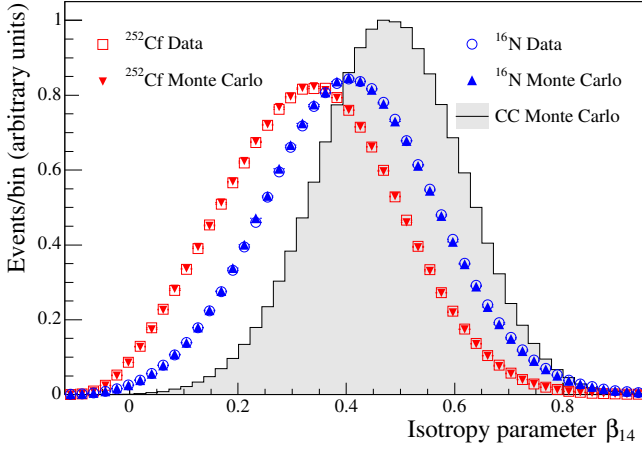
FIG. 11: $\beta_{14}$ isotropy distributions for $^{252}$Cf data and MC, $^{16}$N data and MC, and simulated CC events.

layer of water was compared to that obtained with the updated version of EGS4, EGSnrc [30] which includes the Mott terms as well as other improvements. For electrons with a kinetic energy of 5.0 MeV passing through 1 cm of water, the percentage increase in the fraction that scatters into the forward hemisphere over that obtained with EGS4 is 0.9% when applying the average step length correction, and 1.2% using EGSnrc. The correction to EGS4 was tuned to give the same percentage as EGSnrc.

Figure 11 shows distributions of $\beta_{14}$ using data from $^{252}$Cf and $^{16}$N sources and from corresponding MC simulations. Also shown is a MC simulated distribution for CC events. The $^{252}$Cf and CC events have an imposed kinetic energy threshold of 5.5 MeV, while the $^{16}$N events have kinetic energies between $\sim 4$ MeV and $\sim 6$ MeV. The $^{16}$N source emits 6.13-MeV $\gamma$-rays, which undergo Compton scattering and produce more than one lower energy electron. The CC electrons undergo relatively less multiple-scattering per unit path length than the Compton scattered electrons from the $^{16}$N source, as the CC electrons have higher energy. The average $\beta_{14}$ for $^{16}$N events is therefore smaller (more isotropic) than for CC events.

The $\beta_{14}$ parameter is correlated with event energy and to a lesser extent with radius. Multi-dimensional PDFs are therefore used in the analysis, as described in the signal extraction section.

Systematic uncertainties for $\beta_{14}$ are evaluated through data-MC comparisons of $^{252}$Cf and $^{16}$N calibration runs. For mono-energetic data, $\beta_{14}$ can be well approximated by a Gaussian function. Calibration data for $^{252}$Cf and $^{16}$N and the corresponding MC simulated distributions are fit run-by-run. The difference in the extracted means and widths of the fits is used to characterize the uncertainties. Temporal stability is measured with runs taken with the sources at the center of the detector. Radial uncertainty is determined from multi-axis scans. Figure 12 shows the distributions of $\beta_{14}$ width for $^{252}$Cf data and MC as a function of $\rho$, and $\beta_{14}$ mean for $^{16}$N data and MC versus $\rho$. The average temporal and volume-weighted radial data-MC differences are evaluated separately and then added
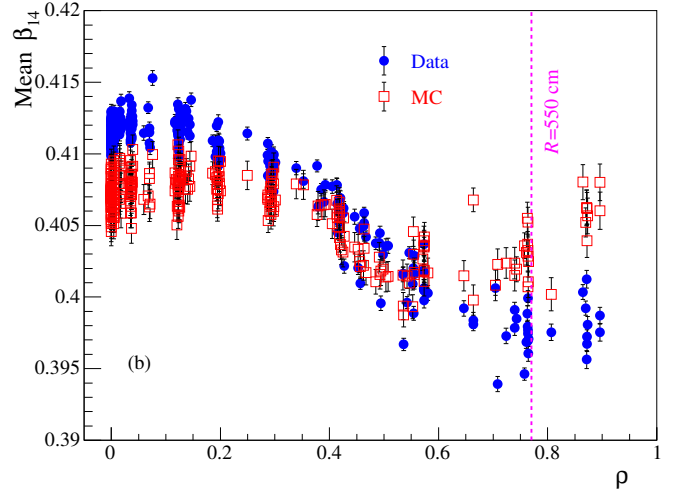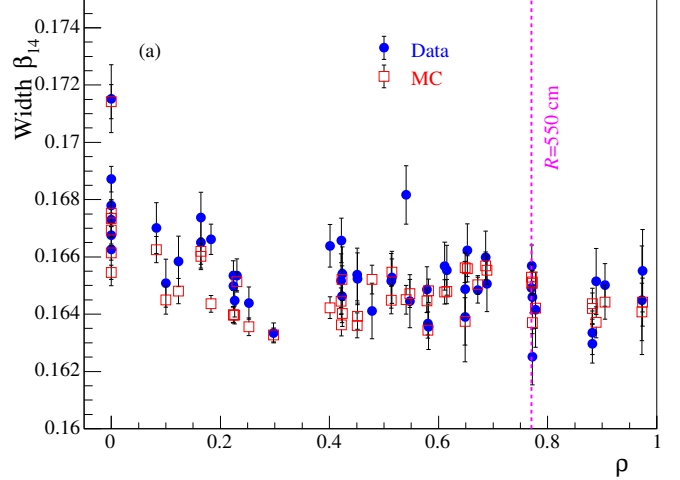


FIG. 12: $\beta_{14}$ isotropy distributions of (a) $^{252}$Cf data and MC width versus $\rho$ and (b) $^{16}$N data and MC mean versus $\rho$. Systematic effects observable in the distributions are attributed to temporal and spatial non-uniformities in detector response and give the estimates on the $\beta_{14}$ systematic uncertainties.

in quadrature. Table VI gives the estimated systematic mean and width $\beta_{14}$ uncertainties from both $^{252}$Cf and $^{16}$N sources. These uncertainties are propagated through the signal extraction by shifting the means and smearing the $\beta_{14}$ PDFs.

TABLE VI: Summary of $\beta_{14}$ scale and resolution systematic uncertainties.

|  | Uncertainty | |
| --- | --- | --- |
| Source | Scale | Resolution |
| $^{252}$Cf | 0.48% | 0.67% |
| $^{16}$N | 0.85% | 0.94% |

The energy dependence of the systematic uncertainty on $\beta_{14}$ for CC events was evaluated using $^{8}$Li calibration data in ad-

FIG. 13: Neutron energy response during the $D_2O$ (dashed) and salt (solid) running periods. The vertical line represents the analysis energy threshold of $T_{eff}$ = 5.5 MeV in the salt period. For the $D_2O$ period the analysis energy threshold was $T_{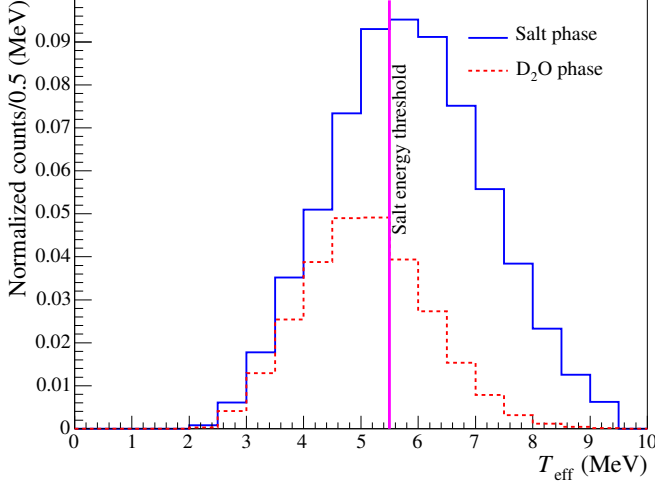eff}$ = 5.0 MeV. The distributions shown here are normalized to the neutron detection efficiency in the two phases for R< 550 cm.

dition to $^{16}$N.

## VI. NEUTRON RESPONSE

With salt added to the $D_2O$ volume, neutron capture is dominated by capture on $^{35}$Cl and losses due to capture on $^{1}$H and $^{17}$O are significantly reduced. For a $^{252}$Cf source at the center of the detector, the probabilities of neutron capture are 90%($^{35}$Cl), 4% ($^{2}$H), 2.5%($^{1}$H ), with the remaining 3.5% absorbed by oxygen, sodium or other isotopes (only 0.3% capture on $^{37}$Cl). In $D_2O$ with no salt additive, the capture probabilities are 49% ($^{2}$H) and 30%($^{1}$H), with 14.5% absorbed by oxygen isotopes in the heavy water and the remaining 6.5% escaping the $D_2O$ volume. For neutrons generated uniformly in the heavy water, the probability of capture on $^{35}$Cl in the salt phase is about three times larger than that of capture on deuterium in the absence of salt.

Not only is the capture efficiency increased, but the energy deposited in the detector is also increased. As shown in Fig. 13, the peak of the energy distribution moves to higher energy so that, for the same energy cut, the salt phase has improved neutron detection efficiency compared to the $D_2O$ phase. This allowed a higher energy threshold for the salt phase and hence less low-energy background contamination.

Neutron response is calibrated primarily with neutrons produced by a $^{252}$Cf source with secondary checks made by analysis of neutrons generated by an Am-Be source and by MC simulations. To determine the neutron detection efficiency using the $^{252}$Cf fission source, the absolute neutron production rate (source strength) has to be determined. Shown in Table VII are the results of four different techniques used to evaluate the source strength and presented as inferred strength of
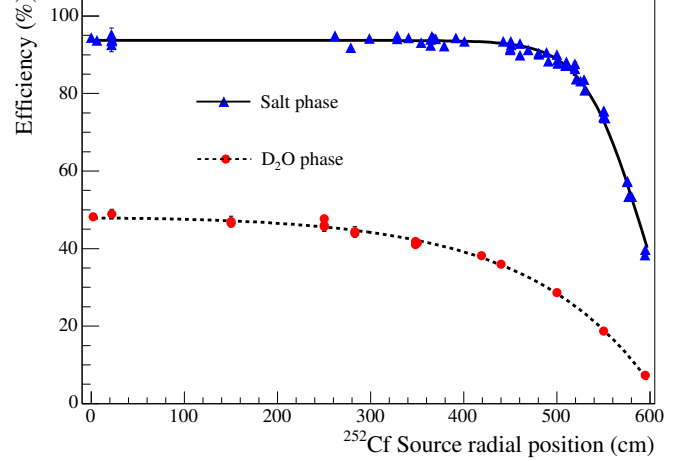


FIG. 14: Neutron capture efficiency versus radial position of the $^{252}$Cf source for the pure $D_2O$ and salt phase. The solid line is a fit of the salt phase data to Eq. (10), and the dotted line is a fit of the $D_2O$ phase data to a neutron diffusion model.

the source on June 12, 2001. The $^{252}$Cf activity decays with a half-life of 2.645 years, and this decay, together with that of a small $^{250}$Cf contamination, is taken into account in evaluating the source strength at the time of a given calibration run.

The Frisch Grid and triggered Si(Li) methods both use an array of calibrated $^{3}$He detectors to detect neutrons with the Si(Li) method being triggered on the fission daughter products of $^{252}$Cf. These methods provide independent measures of the source strength prior to deployment in the SNO detector.

*In-situ* measurements of the source strength and efficiency have also been made in the $D_2O$ and dissolved-salt phases. The $D_2O$ multiplicity method is an *in-situ* method used in the pure $D_2O$ phase of SNO operation to determine the detection efficiency and fission rate. In this method the distribution of the number of neutrons detected in 2-second time windows is plotted and then fit to the multiplicity function. For a model in which the neutron capture time is negligible compared to this time window, the probability of detecting $d$ neutrons in a given time window for $l$ neutrons generated is given by

$$P(d) = e^{-\lambda T}\delta_{d,0} \quad + \sum_{l=d}^{\infty} \frac{l!}{d!(l-d)!}\epsilon^d(1-\epsilon)^{l-d}$$
$$\times \sum_{N=1}^{\infty} \frac{e^{\frac{-(l-N\mu)^2}{2N\sigma^2}}}{(2\pi N\sigma^2)^{1/2}}e^{-\lambda T}\frac{(\lambda T)^N}{N!}. \quad (9)$$

The neutron detection efficiency $\epsilon$ and the fission rate $\lambda$ are the free parameters in the fit. The factor $\delta_{d,0}$ is 1 for $d = 0$ and is 0 otherwise. The time window is $T$. The multiplicity of the $^{252}$Cf source, $\mu$, is taken to be 3.7676±0.0047 neutrons per fission, and the width of the multiplicity distribution, $\sigma$, is 1.57 [31]. The corrections due to the finite neutron capture lifetime in the $D_2O$ volume were estimated by MC simulations.

A time-series method was used in the salt phase to extract the neutron detection efficiency and the fission rate by using

the time separation between fission daughter $\gamma$-rays and neutrons in a 5-parameter fit to an analytical distribution that generalizes the model on which Eq. (9) is based to explicitly include the neutron capture lifetime and the effect of detecting a small fraction of the fission $\gamma$-rays that accompany neutron production. As can be seen in Table VII, the various techniques are in agreement and we calculate a weighted mean as our best estimate of the neutron source strength.

TABLE VII: Results of the various methods for determining the $^{252}$Cf source strength. The source strength is determined for June 12, 2001. The $\chi^2$ for the tabulated source strengths is 5.6.

| Method | Source strength (neutrons per second) |
|---|---|
| LANL Frisch Grid | 16.75 ± 0.14 |
| LANL triggered Si(Li) | 17.08 ± 0.43 |
| D$_2$O multiplicity | 16.33 ± 0.18 |
| Salt time-series | 16.46 ± 0.12 |
| Weighted mean | 16.55 ± 0.08 |

The neutron efficiency is determined by comparing the number of neutrons detected to the number produced, as a function of the position of the $^{252}$Cf source and the energy threshold. In this comparison it is important to take into account events from fission $\gamma$-rays that are emitted in the spontaneous decay of $^{252}$Cf. First the small fraction due to $\gamma$-rays above $T_{\text{eff}} = 6.5$ MeV is determined; then the neutron energy spectrum in the salt phase (Fig. 13) is used to extrapolate down to zero threshold to give the capture efficiency (Fig. 14), and to $T_{\text{eff}} = 5.5$ MeV (Fig. 13) to give the detection efficiency.

To extract the shape of the $^{252}$Cf $\gamma$ spectrum above $T_{\text{eff}} = 6.5$ MeV, a $^{252}$Cf source run was recorded, during the short pure D$_2$O phase following the removal of salt. In D$_2$O, neutrons can be separated easily from the source $\gamma$-rays by requiring that neutron candidate events reconstruct more than 150 cm from the source. The fission $\gamma$-ray energy distribution is then obtained by subtracting the energy distribution of the selected neutron events from the energy distribution of the events that reconstruct within 150 cm of the source. The $\gamma$-ray energy distribution obtained from this measurement and the neutron energy distribution obtained from the salt phase (see below) are then fit to the raw $^{252}$Cf energy distribution in salt with the scaling on the neutron and $\gamma$ distributions left as free parameters to obtain the $\gamma$ background correction above $T_{\text{eff}} = 6.5$ MeV. The time series analysis also gives an independent estimate for the gamma fraction. The combined result from these two methods yields $(1.34^{+1.05}_{-0.56})\%$.

To determine the neutron energy spectrum in the salt phase, a clean neutron sample is required. As the capture distance for neutrons in the salt phase is similar to the attenuation length of fission $\gamma$-rays, a radial cut cannot be used to select neutron events from the calibration data. Instead a "burst cut" was developed to select neutron events from calibration data using the coincidence between fission $\gamma$-rays and neutrons. In salt, the mean capture time for neutrons from $^{252}$Cf data at the detector center is measured to be $5.29 \pm 0.05$ ms and after approximately 40 ms almost all neutrons have been captured. The mean time between fission bursts for the $^{252}$Cf

source used in SNO is about 250 ms. In the burst cut a fission $\gamma$-ray candidate event is selected by choosing events with no preceding events within a 50-ms time interval, and events in a time interval of 40 ms after the selected first event are tagged as neutrons. The burst cut has a selection efficiency for neutrons of 40%, but less than 0.1% of the selected neutron candidate events are estimated to be fission $\gamma$-rays above the threshold ($T_{\text{eff}} = 5.5$ MeV) used in this analysis.

The capture efficiency is obtained for each $^{252}$Cf run with source radial position $r$ (start radius of the neutrons). These point source efficiency results are fit to the empirical model

$$\epsilon(r) = A \{\tanh[B(r-C)] - 1\}, \qquad (10)$$

where $\epsilon(r)$ is the neutron capture efficiency at source position $r$ and requiring neutrons to be captured (reconstructed vertex) inside R< 550 cm. $A$, $B$, and $C$ are the fit parameters of the model. The volume-weighted capture efficiency $\overline{\epsilon}$ is then obtained from the ratio of integrals

$$\overline{\epsilon} = \frac{\int_0^{R_{\text{AV}}} r^2 \epsilon(r) dr}{\int_0^{R_{\text{AV}}} r^2 dr}, \qquad (11)$$

where $\epsilon(r)$ is plotted in Fig. 14.

Figure 15 shows the comparison between detection efficiency distributions obtained from calibration data and from the NC MC simulation as functions of $\rho$ after the $T_{\text{eff}} > 5.5$ MeV selection criterion has been applied. The neutron detection efficiency along with its uncertainty derived from $^{252}$Cf calibration data are shown as the shaded band in this figure. The ratio of the neutral current MC simulation efficiency to the efficiency obtained from calibration data is within 2.2% of one; which is within the estimated systematic uncertainty.

A list of corrections applied to the $^{252}$Cf efficiency measurement is summarized in Table VIII. Apart from the gamma fraction correction discussed previously, these corrections are calculated through MC simulation studies The source sampling correction is needed due to detector asymmetry. The $^{252}$Cf calibration data were predominantly collected with the source positioned in the bottom half of the detector, and therefore do not sample the whole detector. This correction is calculated by doing MC simulation studies at the same $^{252}$Cf source positions as the data, and comparing the efficiency from the point source MC simulation studies with the efficiency derived from a MC simulation study of $^{252}$Cf neutrons uniformly distributed in the detector. The uncertainty on this correction is included in Table IX. A correction is applied to the calibration efficiency measurement to account for the $^2$H$(n,2n)^1$H reaction with fission energy neutrons. This correction is determined from a MC simulation study. The $\gamma$ fraction correction is the previously discussed correction to account for $^{252}$Cf fission $\gamma$-rays contaminating the $^{252}$Cf neutron data. A correction is also applied to account for the $^{16}$O$(n,\alpha)^{13}$C reaction with fission energy neutrons. Finally, a source geometry correction is applied to account for neutron captures on the steel and acrylic of the source holder.

The systematic uncertainties on the $^{252}$Cf neutron detection efficiency measurement are listed in Table IX. Some of the
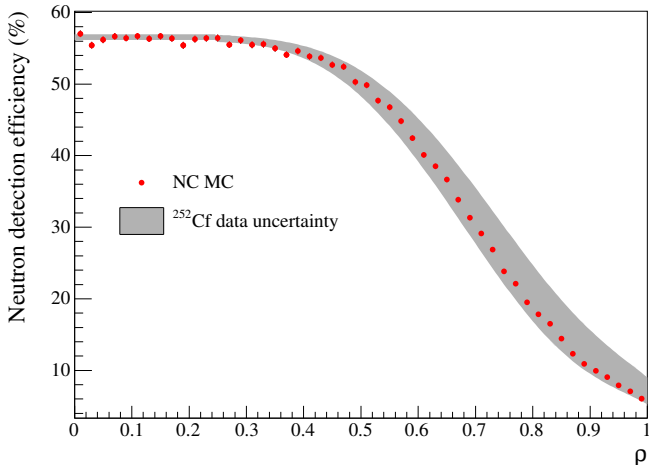
FIG. 15: Comparison of neutron detection efficiency ($T_{\rm eff}$ > 5.5 MeV) for MC simulated NC events (data points) and that derived from $^{252}$Cf calibration data (shaded band) as a function of volume-weighted radius $\rho$. The band represents the statistical and systematic uncertainties summarized in Table IX. An additional 1.0% radial reconstruction uncertainty that is assigned to the solar neutrino flux is also included in the band. The volume-weighted NC MC efficiency is within the systematic uncertainty assigned to the $^{252}$Cf measurement.

uncertainties arise from the corrections listed in Table VIII. The source strength uncertainty is derived from the results summarized in Table VII. Source position uncertainty is obtained by shifting the estimated source positions by ±2 cm or ±10 cm in radius, depending on the detector region, and then re-calculating the volume-weighted efficiency. The AV position uncertainty is taken from a ±6 cm $z$ shift in the acrylic vessel position. An estimate of the uncertainty in the interpolation shown in Fig. 14 was taken as the difference between a high-order polynomial fit and the empirical fit to the data. The volume-weighted neutron detection efficiency for the analysis threshold of $T_{\rm eff}$ = 5.5 MeV and a fiducial volume of 550 cm after applying the corrections listed above is (40.7 ± 0.5 $^{+0.9}_{-0.8}$)% where the first uncertainty is statistical and the second the combined systematic uncertainty. This is the efficiency for detecting neutrons uniformly generated within the whole AV and with reconstructed vertex less than $\rho$ = 0.77.

TABLE VIII: Corrections applied to the neutron efficiency measurement from the calibration data.

| Source | Correction, % |
|---|---|
| Source sampling | −(2.4 ± 1.0) |
| (n,2n) | −(0.58 ± 0.10) |
| (n,$\alpha$) | +(0.66 ± 0.13) |
| Gamma fraction | −(1.34$^{+0.56}_{-1.05}$) |
| Source geometry | +(2.03±0.53) |
| Total | −1.73$^{+1.3}_{-1.6}$ |

TABLE IX: Systematic uncertainties on the neutron efficiency measurement from the calibration data.

| Source | Uncertainty, % |
|---|---|
| Source strength | ±0.5 |
| Source position | +1.7, −1.0 |
| Gamma fraction | +0.56, −1.05 |
| AV position | ±0.3 |
| (n,2n) | ±0.10 |
| (n,$\alpha$) | ±0.13 |
| Empirical fit - polynomial fit | +0.4 |
| Source sampling | ±1.0 |
| Source geometry | ±0.53 |
| Total uncertainty | +2.3, −2.0 |

## VII. BACKGROUNDS

Several sources of backgrounds are present in the data. These include instrumental backgrounds, backgrounds from the natural $^{232}$Th and $^{238}$U radioactivity chains, and backgrounds associated with products of cosmic muon spallation and atmospheric neutrino interactions in the detector. While some of these background types can be eliminated by analysis cuts, most cannot be distinguished from the solar neutrino signals. Table X provides a summary of the estimated contributions from these backgrounds. In the following subsections, the identification and the determination of the contributions of these backgrounds is discussed.

### A. Instrumental Backgrounds

A significant portion of the events comprising the raw data are the instrumental backgrounds discussed in Sec. III B. The instrumental background cuts and the high-level cuts are very efficient at removing these events. The residual contamination of instrumental backgrounds in the data set is measured by using a bifurcated analysis [32]. In this analysis, each set of cuts is used to calibrate the acceptance for background of the other set, allowing the leakage through the combination of both sets to be calculated. The two sets of cuts must be orthogonal (uncorrelated) for the bifurcated analysis to work and are chosen appropriately. Orthogonality is demonstrated using a technique known as "relaxing the box" in which the bifurcated analysis correctly estimated the increase in residual background as cuts are relaxed when applied to the data set.

The bifurcated analysis provides an upper limit on the residual instrumental contamination of 3.0 events in the neutrino data which is treated as a 68% CL limit in subsequent analyses. This analysis is represented in Fig. 16 where the distribution of the high-level cut parameters is presented for the neutrino data set before application of these cuts, and for instrumental backgrounds rejected by the instrumental cuts. In this figure, the two parameters are the isotropy of the light distribution $\beta_{14}$ and the fraction of PMT hits within the prompt light time window.

TABLE X: Summary of backgrounds. The second column gives the event rate in the SNO detector $D_2O$ volume (r=600.5 cm) when an average production rate was used. The last column gives the estimated number of events remaining in the 391-day salt phase data set after cuts. The internal neutron and $\gamma$-ray backgrounds are determined from independent information and constrained in the analysis. The external-source neutrons are extracted along with the signal estimated from the energy-unconstrained signal extraction fit. For backgrounds for which only an upper limit can be determined, the 68% CL upper limit is used as a 1-standard-deviation uncertainty in the error propagation.

| Source | Average rate | | Counts in data set |
|---|---|---|---|
| Neutrons generated inside $D_2O$: | | | |
| $^2$H photodisintegration [U, Th] | | | $91.3^{+30.4}_{-31.5}$ |
| $^2$H photodisintegration [$^{24}$Na] | | | $10.2 \pm 2.5$ |
| n from fission [U] | 0.43 | n $\mu$g$^{-1}$U y$^{-1}$ | $0 \pm 0$ |
| $^2$H($\alpha,\alpha$n)$^1$H [Th] | 1.9 | n $\mu$g$^{-1}$ Th y$^{-1}$ | $0.93 \pm 0.50$ |
| $^2$H($\alpha,\alpha$n)$^1$H [$^{222}$Rn] | 0.80 | n $\mu$g$^{-1}$ U y$^{-1}$ | $2.89 \pm 0.47$ |
| $^{17,18}$O($\alpha$,n)$^{20,21}$Ne [Th] | 0.09 | n $\mu$g$^{-1}$ Th y$^{-1}$ | $0.03 \pm 0.02$ |
| $^{17,18}$O($\alpha$,n)$^{20,21}$Ne [$^{222}$Rn] | 0.20 | n $\mu$g$^{-1}$ U y$^{-1}$ | $0.72 \pm 0.12$ |
| n from atmospheric $\nu$ | | | $15.8^{+21.3}_{-4.6}$ |
| $^{24}$Na from muons | 0.33 | n y$^{-1}$ | $0.14 \pm 0.14$ |
| muons in SNO | 11240 | n y$^{-1}$ | $\leq 1$ |
| muons in rock | 0.14 | n y$^{-1}$ | $0.08 \pm 0.01$ |
| $\overline{\nu}_e$ "ccp" | 0.03 | n y$^{-1}$ | $0.01 \pm 0.01$ |
| $\overline{\nu}_e$ "ccd" | 1.43 | n y$^{-1}$ | $0.6 \pm 0.1$ |
| $\overline{\nu}_e$ "ncd"-reactor | 3.24 | n y$^{-1}$ | $1.4 \pm 0.3$ |
| $\overline{\nu}_e$ "ncd"-terrestrial | 1.2 | n y$^{-1}$ | $0.5 \pm 0.1$ |
| CNO $\nu$ | 1.0 | n y$^{-1}$ | $0.4 \pm 0.4$ |
| *Total internal-source neutrons* | | | $125.1^{+37.3}_{-32.0}$ |
| $\gamma$-rays generated uniformly inside $D_2O$: | | | |
| $\gamma$ from fission [U] | 0.04 | $\gamma$ $\mu$g$^{-1}$U y$^{-1}$ | $0 \pm 0$ |
| $\gamma$ from atmospheric $\nu$ | | | $3.2^{+4.6}_{-4.4}$ |
| *Total internal-source $\gamma$-rays* | | | $3.2^{+4.6}_{-4.4}$ |
| Decays of spallation products throughout $D_2O$: | | | |
| $^{16}$N following muons | | $^{16}$N y$^{-1}$ | $< 1.3$ |
| Other spallation | 1.2 | $^A$Z y$^{-1}$ | $\leq 0.8$ |
| Cherenkov events from radioactivity inside $D_2O$: | | | |
| $\beta\gamma$ decays (U,Th,$^{24}$Na) | | | $3.6^{+1.0}_{-0.9}$ |
| Backgrounds produced outside $D_2O$: | | | |
| Externally generated neutrons (from fit) | | | $128.5 \pm 42.4$ |
| $\beta\gamma$ decays (U, Th) in AV, $H_2O$, PMTs | | | $< 18.5$ |
| Instrumental contamination | | | $<3$ |
| Isotropic acrylic vessel events | | | $< 6.55$ |

One key point regarding the bifurcated analysis is that both sets of cuts must be sensitive to each background class in order for that class to be included in the background estimate. This is true of all known instrumental backgrounds, except for the isotropic events from the acrylic vessel. For this reason a separate estimate of this background is required.
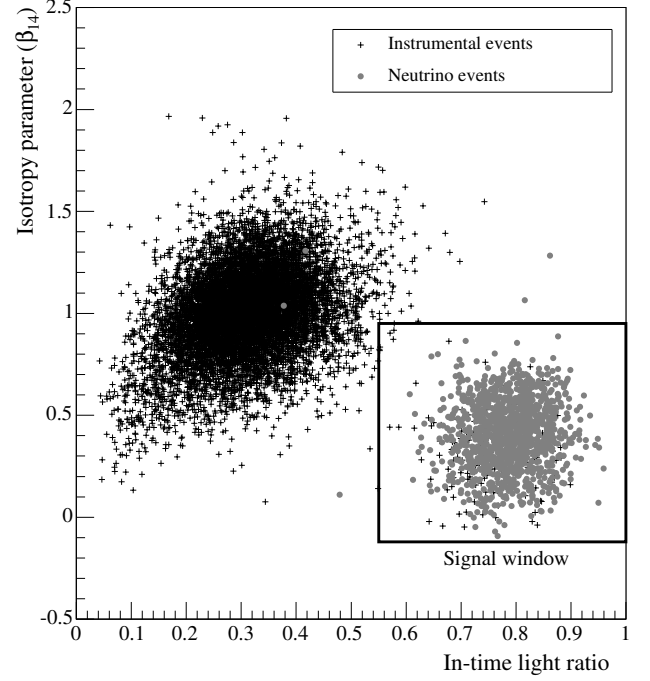


FIG. 16: The distribution of high-level cut parameters for instrumental backgrounds and neutrino candidates. The two cut parameters are the isotropy $\beta_{14}$ and the fraction of PMT hits within the prompt time window. The $^{16}$N calibration source was used to generate the sample "neutrino candidate" events and thereby establish the signal window for Cherenkov events and to calibrate the cut efficiency.

### B. Isotropic Acrylic Vessel Background

A class of background events of uncertain origin was identified in the $D_2O$ phase. These events reconstruct near the acrylic vessel and are characterized by a nearly isotropic light distribution. They may result from triboluminescence as stresses are relieved in acrylic. In the analysis of the data from the $D_2O$ phase, the events were removed by the isotropy and fiducial volume cuts. However, the isotropy cut has been relaxed for the salt phase because it would eliminate too many neutrons, whose Cherenkov light distribution is more isotropic in the presence of salt.

Two independent analyses were performed to estimate the background remaining after the fiducial volume selection cut of $R <550$ cm was applied. In the first analysis the isotropy distribution of the salt data was fit to the expected shapes for neutrons and electrons. The difference between this fit result and the actual signal in the high-isotropy region of the spectrum was attributed to isotropic background events in the data set.

In the second method, a cut was applied on the isotropy parameter to the pure $D_2O$ data set, where the neutrino signals are clearly defined. The difference between the actual number of events removed by the cut and the predicted loss of neutrino

events yields an estimate of the background in the $D_2O$ data set. This estimate was then scaled to obtain a limit for the salt data.

The combination of the analyses gives a 68% upper limit of 6.55 events inside the fiducial volume of $R \leq 550$ cm and with a kinetic energy above 5.5 MeV in the salt data set. The same analyses were repeated separately on the day and night data sets, yielding a day-night asymmetry, defined as the difference between the night and the day signal rates normalized by their average, of 0.68±0.31.

### C. Photodisintegration Backgrounds from Internal Radioactivity

The deuteron can be dissociated by a $\gamma$-ray above the binding energy of 2.22 MeV. The $\beta - \gamma$ decays of $^{208}$Tl and $^{214}$Bi from the $^{232}$Th and $^{238}$U chains emit $\gamma$-rays that are above this binding energy. Neutrons produced through photodisintegration are indistinguishable from those produced by the NC reaction, therefore measurement of the levels of backgrounds inside the detector is crucial for an accurate measurement of the total $^8$B flux. A concentration of $3.8 \times 10^{-15}$ g Th/g$D_2O$ or $30 \times 10^{-15}$ gU/g$D_2O$ in the heavy water would each contribute one photodisintegration neutron per day.

Two independent approaches were developed to measure these backgrounds, which can be classified as *ex-situ* and *in-situ* techniques.

Three *ex-situ* techniques have been developed to assay precursor radioisotopes of $^{208}$Tl and $^{214}$Bi in the $D_2O$ and the $H_2O$. The decays of the parent Rn and Ra isotopes are counted in a system external to the SNO detector. Two of these techniques extract $^{224}$Ra and $^{226}$Ra using beads coated with manganese oxide (MnO$_X$) [33] or membranes loaded with hydrous titanium oxide (HTiO) [34]. Radioassays typically involve the circulation of 500 tonnes of $D_2O$ of which approximately 400 tonnes is flowed through these media. In the MnO$_X$ technique, Rn daughters from the Ra decays are identified by $\alpha$ spectroscopy. In the HTiO technique, the extracted Ra atoms are concentrated and identified by $\beta - \alpha$ coincidences of their decay products. Because the ingress of long-lived (T$_{1/2}$= 3.8 d) $^{222}$Rn (e.g., by emanation from materials or ingress from laboratory air) breaks the equilibrium with $^{226}$Ra, this background in the water is obtained by degassing and cryogenically concentrating the dissolved gas from assays of approximately 5 tonnes of water [35]. The $^{222}$Rn decays are subsequently counted in a ZnS(Ag) scintillation cell.

Over the entire salt phase, 16 MnO$_X$ and 6 HTiO assays were conducted at regular intervals. The addition of salt to the heavy water affected the radium assay techniques in two ways: 1) a somewhat reduced radium extraction efficiency was observed on MnO$_X$ (81% compared to 95% in pure $D_2O$) and 2) dissolved manganese steadily increased from a constant 2 ppb in pure $D_2O$ to 12 ppb at the end of the salt phase, causing interference with the measurement of the concentration of radium in the HTiO assays. During the salt phase, the manganese could not be removed by the reverse osmosis method, as that would have also removed the salt. Since the MnO$_X$

TABLE XI: $^{224}$Ra assay results for elements of the $D_2O$ systems, compared to the total activity measured in the complete system. These measurements do not include the small piping section in the detector.

| Element of heavy water system | Th bkgd. ($^{224}$Ra/day) |
|---|---|
| Ultrafiltration unit (assay system) | $28^{+27}_{-23}$ |
| Heat exchanger | $233^{+50}_{-48}$ |
| Ultrafiltration unit (main stream) | $78^{+37}_{-31}$ |
| Main recirculation pump | $72^{+33}_{-30}$ |
| Process degasser | $75^{+31}_{-29}$ |
| Filtration unit (main stream) | $< 36$ |
| Piping | $330 \pm 184$ |
| Complete system | $816 \pm 165$ |

technique did not suffer from interference with dissolved manganese in the $D_2O$, its results were used as the *ex-situ* measurement of the $^{224}$Ra concentration.

A small amount of activity was observed in all the elements outside the acrylic vessel and corresponded to a total production rate of $816 \pm 165$ $^{224}$Ra atoms per day, with approximately a quarter of these produced before the columns. This activity caused a correction of $0.65 \times 10^{-15}$ gTh/g$D_2O$ to the *ex-situ* measurements. An assay showed no significant change in activity when the salt was added to the $D_2O$ and after the salt was removed most of the activity in the elements outside the acrylic vessel went away. The increase in the salt phase (from an upper limit of 16 $^{224}$Ra atoms per day in the $D_2O$ phase) is interpreted as primarily due to a displacement of the equilibrium between radium in solution and radium bound to its Th sources in the water system, arising from the presence of Na$^+$ ions in the $D_2O$. The time constant associated with the removal of this activity showed that it originated from flowing as well as stagnant segments of the water circulation and assay systems. Components of the systems can be isolated and the $^{224}$Ra contribution from each component was measured by circulating the enclosed water over a MnO$_X$ column. Table XI provides a summary of the measured production rate of $^{224}$Ra in various components in the assay and water circulation systems. The amount in the piping outside the AV is the difference between the total and the sum of the other individual elements. The piping within the AV is substantially shorter and thinner than that outside and any contribution from this section was assumed negligible.

During a normal assay, the activity measured on the MnO$_X$ assay columns is the sum of contributions from the $D_2O$ and from the piping leading to the columns. The effect of this source of Th on the levels in the heavy water target over time was modeled, given the source distribution in the water piping and the water circulation paths and times. The model divided the piping external to the acrylic vessel into sections, and traced the amount of $^{224}$Ra activity added during the assays.

The mean level of Th concentration in the $D_2O$ target was

$(1.76^{+0.41}_{-0.68}) \times 10^{-15}$ gTh/gD$_2$O, where the quoted uncertainty reflects the possible distribution of this background activity. Combining this in quadrature with the systematic uncertainties associated with the MnO$_X$ assay technique of $^{+32}_{-37}$% gives $(1.76 \pm 0.44(\text{stat})^{+0.70}_{-0.94}(\text{syst})) \times 10^{-15}$ gTh/gD$_2$O for the *ex-situ* analysis.

The *in-situ* technique uses pattern recognition on the Cherenkov light distribution to determine the equivalent concentration of $^{232}$Th and $^{238}$U in the water. The decays of $^{208}$Tl produce a more isotropic light distribution than $^{214}$Bi decays because of a more complex decay scheme. In the energy window $4 < T_{\text{eff}} < 4.5$ MeV, decays of $^{208}$Tl and $^{214}$Bi in the Th and the U chains are the dominant components of the Cherenkov signal. By studying events that reconstruct with $R < 450$ cm, $^{208}$Tl and $^{214}$Bi are separated statistically by their differences in the light isotropy $\beta_{14}$. In this energy interval, the Cherenkov light from $^{214}$Bi decays is primarily from the direct ground state $\beta$ decay with an endpoint of 3.27 MeV, while almost every $^{208}$Tl decay emits a 2.614-MeV $\gamma$, accompanied by one or more low-energy $\gamma$-rays and a $\beta$ with an endpoint energy up to 1.8 MeV. Therefore $^{208}$Tl decays produce a more isotropic light distribution than $^{214}$Bi decays. The *in-situ* technique also has the advantage of providing direct determination of the background levels during data taking without any assumptions regarding temporal variation between assays.

The statistical separation of the $^{208}$Tl and $^{214}$Bi decay signals using $\beta_{14}$ is shown in Fig. 17, where the probability density functions (PDFs) used in the maximum likelihood analysis were determined from MC simulations. Solar neutrino and $^{24}$Na signals, which are backgrounds to the *in-situ* analysis, were constrained in this analysis (an undistorted $^8$B neutrino spectrum was assumed). Some of the background $^{24}$Na was produced by neutron activation of the D$_2$O target during the deployment of calibration sources. Data runs that were known to have significant levels of $^{24}$Na and Rn ingress were removed in the run selection process described in Sec. III A. Additional $^{24}$Na was produced in the D$_2$O in the chimney region of the acrylic vessel, in a buffer tank used in the circulation of D$_2$O, and in the water circulation pipes. These regions are not well shielded from fast neutrons and $\gamma$-rays emitted from the rock in the underground laboratory. The residual contributions from these sources of $^{24}$Na were tallied, and the photodisintegration neutron production rate was found to be $0.064 \pm 0.016$ d$^{-1}$. The $^{24}$Na background contribution introduced by water circulation was calculated using a water flow model and constrained in the maximum likelihood fit. The $\beta_{14}$ PDFs were calibrated by $^{222}$Rn and $^{24}$Na calibration spikes in the D$_2$O. The latter has a $\beta_{14}$ distribution similar to $^{208}$Tl decays.

The amplitudes of the $^{208}$Tl and $^{214}$Bi signals determined from the *in-situ* analysis were converted to the equivalent concentration of $^{232}$Th and $^{238}$U under secular equilibrium. The equivalent concentrations integrated over the solar neutrino data set are found to be $0.85^{+0.44}_{-0.42}(\text{stat})$ $^{+0.42}_{-0.44}(\text{syst}) \times 10^{-15}$ gTh/gD$_2$O and $8.28^{+0.83}_{-0.81}(\text{stat})$ $^{+1.10}_{-1.94}(\text{syst}) \times 10^{-15}$ gU/gD$_2$O respectively.

Results from the *ex-situ* and the *in-situ* analyses of the D$_2$O are shown in Fig. 18. They are consistent with each other. The
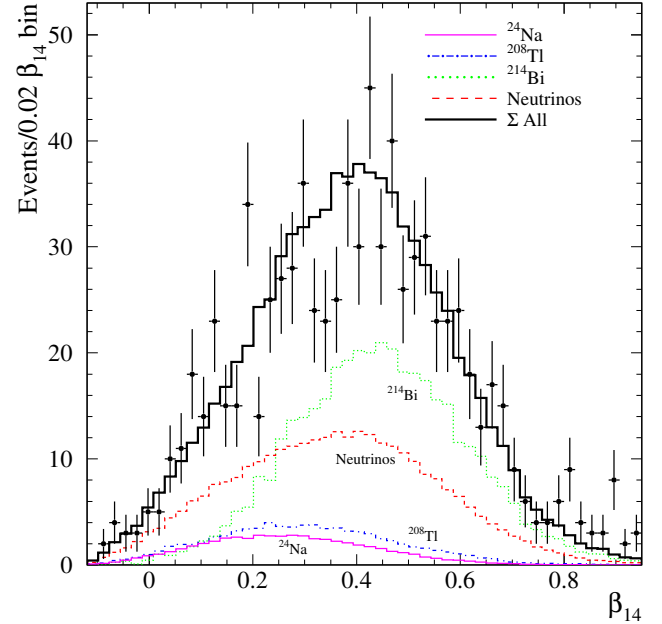


FIG. 17: *In-situ* determination of the low-energy background in the D$_2$O. The data points represent low-energy events selected by the criteria described in the text. The data isotropy ($\beta_{14}$) distribution is fit to a combination of $^{208}$Tl and $^{214}$Bi distributions. Also shown are the $^{24}$Na background and solar neutrino contributions that were constrained in the fit. The fit result is shown as the sum histogram.

*ex-situ* and the *in-situ* techniques are independent and their systematic uncertainties were independently assessed. To obtain the best measurement of the equivalent concentration of $^{232}$Th in the D$_2$O target during the 391-day live time period, the weighted mean of the two techniques is used as the background input to the integral neutrino flux measurement described in Sec. XI. The $^{238}$U chain activity is dominated by Rn ingress which is highly time dependent. In addition, only an upper limit could be obtained for the weighted average of the *ex-situ* measurements because of intermittent backgrounds in the radon extraction process. Therefore the *in-situ* determination was used for the estimate of this activity as it provides the appropriate weighting by neutrino live time. The photodisintegration neutron production rates from the natural chains were calculated by MC simulations, which show that the equivalent of 3.79 $\mu$g $^{232}$Th or 29.85 $\mu$g $^{238}$U produces one photodisintegration neutron per day in the D$_2$O target.

The photodisintegration neutron production rates from decays in the $^{232}$Th and $^{238}$U chains in the current data set are summarized in Table XII. To determine the temporal variation of the internal backgrounds, the data set was divided into four time bins. An *in-situ* determination was performed in each of the time periods, and the equivalent concentrations of $^{232}$Th and $^{238}$U were found to be relatively constant. The *in-situ* analysis was repeated for the day and the night data

TABLE XII: Photodisintegration neutron production rate from decays of daughters in the $^{232}$Th and $^{238}$U chains in the D$_2$O. The rates from the *ex-situ* and the *in-situ* techniques are consistent with each other. The total rate from the last row is used for all the solar neutrino analyses that do not depend on the solar zenith angle. The day (D) and night (N) *in-situ* results are used as inputs to the day-night solar neutrino flux asymmetry analysis.

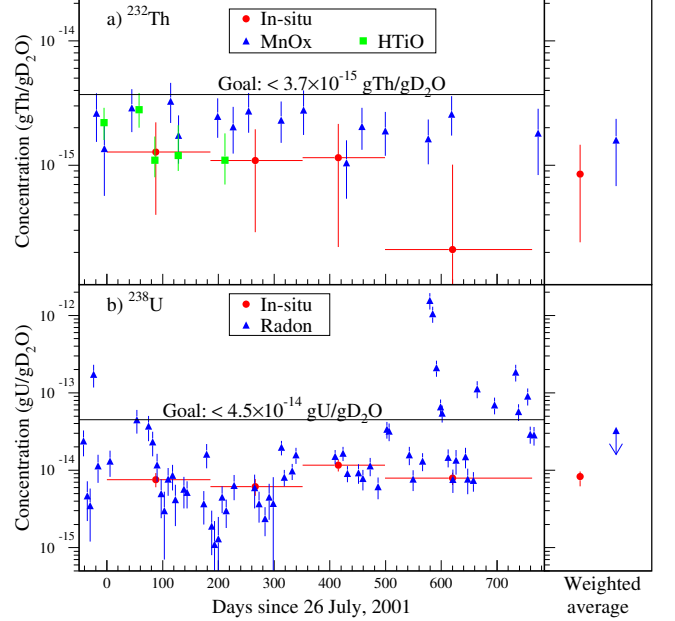| | $^{232}$Th (n d$^{-1}$) | $^{238}$U (n d$^{-1}$) |
|---|---|---|
| *in-situ* (D) | $0.15^{+0.23}_{-0.18}$ | $0.32^{+0.05}_{-0.05}$ |
| *in-situ* (N) | $0.36^{+0.25}_{-0.25}$ | $0.26^{+0.06}_{-0.06}$ |
| *in-situ* (D+N) | $0.22^{+0.16}_{-0.16}$ | $0.28^{+0.04}_{-0.07}$ |
| *ex-situ* (D+N) | $0.42^{+0.23}_{-0.17}$ | $< 1$ |
| Total (D+N) | $0.29^{+0.18}_{-0.18}$ | $0.28^{+0.04}_{-0.07}$ |



FIG. 18: (a) Thorium and (b) uranium backgrounds (equivalent equilibrium concentrations) in the D$_2$O deduced by *in-situ* and *ex-situ* techniques. The MnO$_x$ and HTiO radiochemical assay results, the Rn assay results, and the *in-situ* Cherenkov signal determination of the backgrounds are presented for the period of this analysis on the left-hand side of frames (a) and (b). The right-hand side shows time-integrated averages including an additional sampling systematic uncertainty for the *ex-situ* measurement. The large $^{222}$Rn excess near day 580 is the decay of Rn that was added for calibration purposes, and was excluded in calculating the mean *ex-situ* results. The weighted average of the *ex-situ* $^{222}$Rn measurements appear as an upper limit only. This is due to intermittent background appearing in the radon extraction process.

set, and the results are also summarized in Table XII. In the day-night asymmetry measurement of the neutrino flux, the internal background asymmetry was determined from the *in-situ* analysis of the day and the night data sets, as this gives the proper temporal variation.

Both the *ex-situ* and *in-situ* techniques were also applied to the determination of radioactive backgrounds in the H$_2$O. Throughout the salt phase, 86 radon, 30 MnO$_X$ and 13 HTiO radioassays of the H$_2$O were performed. Results from the radon assays performed on the same day were averaged. The MnO$_X$ and HTiO results were consistent with one another and the weighted average, taking into account the neutrino live time, was used to determine the mean concentration of radioisotopes. The activities were found to be $5.2^{+1.6}_{-1.6} \times 10^{-14}$ gTh/gH$_2$O and $20.6^{+5.0}_{-5.0} \times 10^{-14}$ gU/gH$_2$O by the *ex-situ* techniques.

In the *in-situ* analysis of the H$_2$O background, a monitoring window for events with $4 < T_{\rm eff} < 4.5$ MeV in the H$_2$O region ($650 < R < 680$ cm) was utilized, and the equivalent $^{232}$Th and $^{238}$U concentrations were determined by fitting the isotropy distribution. The radioactive backgrounds in the H$_2$O deduced from the *in-situ* technique were $6.1^{+4.1}_{-1.6} \times 10^{-14}$ gTh/gH$_2$O and $19.1^{+11.1}_{-4.5} \times 10^{-14}$ gU/gH$_2$O, which are consistent with the results from the *ex-situ* technique. As is discussed below, the neutron background due to radioactivity external to the D$_2$O target is determined in the fit of the solar neutrino fluxes (Sec. IX). The photodisintegration background arising from activity in the H$_2$O is part of this external neutron background.

### D. Cherenkov Backgrounds

The broad energy resolution of the detector allows a small fraction of the $\beta - \gamma$ decays in the natural radioactive chains to appear in the neutrino data sample, even though their $Q$ values are lower than the $T_{\rm eff} = 5.5$-MeV neutrino analysis threshold. The number of these *internal Cherenkov* events originating within the D$_2$O target is kept small primarily by ensur-

ing low radioactivity levels. Outside the heavy water volume, however, the acrylic vessel, the light water, and in particular the PMT array and support structure have higher levels of radioactivity. Most of these *external Cherenkov* events are eliminated by imposing a 550-cm fiducial volume cut. These events can "leak" into the fiducial volume in two ways: $\gamma$-rays can travel unscattered from their external origin inward and events whose origin is outside the volume can have a mis-reconstructed vertex located inside.

The internal Cherenkov background was determined from MC simulations and calibration with a controlled injection of $81\pm4$ Bq of $^{222}$Rn (a 'radon spike') into the D$_2$O target. In the analyses of the internal Cherenkov background, the ratio between the number of internal Cherenkov events and the number of detected photodisintegration neutrons above the neutrino analysis threshold was determined for backgrounds from the $^{232}$Th and the $^{238}$U chains. This ratio was then normalized by the measured number of photodisintegration neutrons produced and the neutron detection efficiency in the fiducial
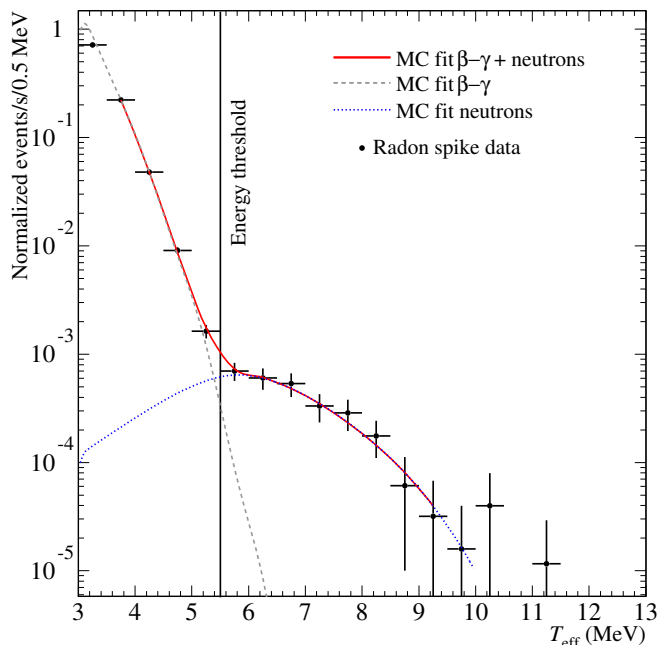
FIG. 19: Fitted MC prediction to the radon spike data, with the steeply falling background Cherenkov spectrum and neutron peaks shown separately.

volume (described above). For $^{208}$Tl decays in the Th chain and $^{24}$Na, MC simulations of their Cherenkov signals were used. The systematic uncertainties were determined by performing 10 000 simulated experiments, with the scale and resolution of the energy response, vertex reconstruction, and $\beta_{14}$ drawn from distributions estimated by the respective analyses. All analysis cuts applied to the neutrino data sample were also applied here, and their individual uncertainties included in the measurement. For the $^{214}$Bi decays in the U chain, the energy-differential uncertainties of the Rn spike energy spectrum were first determined by 1000 simulated experiments. Each of the simulated experiments assumed a different spatial distribution of radioactivity within the detector, constrained by the reconstructed position of low-energy events in the neutrino data set. Uncertainties associated with the time variation of the detector response over the course of the neutrino data set were taken from the calibration analyses. The Cherenkov-to-photodisintegration neutron ratio was determined by fitting the energy distribution of the Rn spike (with its uncertainties determined from the simulated experiments) to the simulated Cherenkov background and neutron spectra. The parameters which were allowed to float in the fit included the energy scale, the energy resolution, and the amplitudes of both the Cherenkov events and the associated photodisintegration neutrons. Figure 19 shows the resultant fit. The energy scale and resolution uncertainties were both consistent with the analyses of $^{16}$N and $^{252}$Cf data. The systematic uncertainties on the ratio were determined by varying all the parameters over their allowed uncertainties, including all covariances.

At $T_{\rm eff} > 5.5$ MeV, the ratio of the number of Cherenkov

events to detected photodisintegration neutrons was found to be $0.011^{+0.005}_{-0.002}$ for $^{208}$Tl, $0.090^{+0.024}_{-0.018}$ for $^{24}$Na and $0.053^{+0.011}_{-0.013}$ for $^{214}$Bi, which correspond to a total of $3.6^{+1.0}_{-0.9}$ observed events in the 391-day data set. Since the multiplicative factors used to scale the photodisintegration neutron amplitude to the number of internal Cherenkov events are independent of the solar zenith angle, the internal Cherenkov backgrounds in the day and the night data set are obtained by scaling the *in-situ* results in Table XII.

The analysis methods for the internal Cherenkov backgrounds are not directly applicable to the external Cherenkov backgrounds. Outside the fiducial volume, the detector is not as well calibrated because of greater optical complexity and limited accessibility for the primary optical and energy calibration sources. To model the radioactivity in this region, Th and U sources were deployed at various locations external to the fiducial volume and used to generate volume-weighted radial distributions for low-energy backgrounds originating from the acrylic vessel, the $H_2O$, and the PMT support structure. The radial distributions were utilized since they are relatively insensitive to Th and U differences. For the acrylic vessel and the PMT support structure, the $\rho$ distributions were based on a Th source encapsulated in acrylic. For the $H_2O$ region, a calibrated $^{222}$Rn spike was used. Events with $T_{\rm eff} > 4.5$ MeV and $1.1 < \rho < 2.5$ in the neutrino data set were fit by a maximum likelihood technique with radial PDFs generated with the same energy threshold as the source data. Figure 20 shows the results of this fit, where the width of the band in the figure represents the systematic uncertainties. These uncertainties include spatial and temporal dependence of the reconstruction, subtraction of contributions from photodisintegration neutrons near the acrylic vessel, and the difference between the $\rho$ distributions of the decays of U and Th daughters. Due to limited statistics in the source PDFs, the fit to the $\rho$ distribution for the neutrino data set could not be done at the solar neutrino analysis energy threshold of $T_{\rm eff} > 5.5$ MeV. Therefore, the $\rho$ distributions for the source data with $T_{\rm eff} > 5.5$ MeV were normalized by the amplitudes obtained in the fit to the data with $T_{\rm eff} > 4.5$ MeV and extrapolated inside the fiducial volume to estimate the number of background events in the signal window. This analysis was repeated for the day and night data sets. At the neutrino analysis energy threshold, the extrapolated contributions of the backgrounds from different detector regions are consistent with zero. For the 391-day salt data set, the 68% upper limit for the acrylic vessel, $H_2O$, and the PMT background contributions are 7, 3, and 11 events respectively with a combined upper limit of the total external Cherenkov background of 18.5 events. The day-night asymmetry of this external background is -0.10±0.16.

### E. Other Backgrounds

In addition to the main contributions stemming from deuteron photodisintegration and low-energy Cherenkov events from $\beta - \gamma$ decays, there are other sub-dominant backgrounds that must be assessed. These backgrounds include
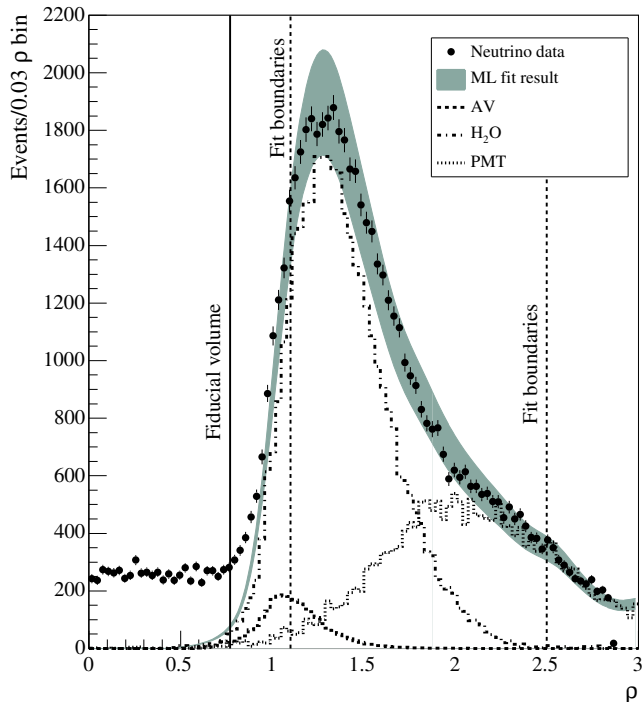
FIG. 20: Maximum likelihood fit of the data $\rho$ distribution (data points) to the PDFs constructed from Th or U calibration sources. Because the external Cherenkov backgrounds are small for the solar neutrino analysis threshold ($T_{\mathrm{eff}} > 5.5$ MeV) and fiducial volume ($\rho < 0.77$), this fit is performed for $T_{\mathrm{eff}} > 4.5$ MeV in the region $1.1 < \rho < 2.5$ in order to enhance the statistics. Contributions of these backgrounds are then obtained from extrapolating the fit results to the solar neutrino signal window. The band represents the systematic uncertainties in this analysis.

contributions from $\alpha$ reactions on elements in the water target and the construction materials, $^{238}$U fission, cosmic ray spallation, and reactor and atmospheric neutrinos.

A small source of neutrons can come from $\alpha$ reactions on $^2$H, $^{17}$O, and $^{18}$O. The $\alpha$s produced in the uranium and thorium decay chains. Neutrons can also be produced from the spontaneous fission of $^{238}$U, which has a half-life of $(8.2\pm0.1)\times10^{15}$ years. The concentration of $^{238}$U has been measured using *ex-situ* HTiO radioassays. Results from the assays indicate a negligible contribution of neutrons and $\gamma$-rays from the spontaneous fission of $^{238}$U in the D$_2$O.

Backgrounds from atmospheric neutrino interactions were estimated with the aid of the NUANCE [36] neutrino Monte Carlo simulation package. Atmospheric neutrino interactions can contribute to the production of neutrons without other energy deposits to tag the event, or via the production of untagged photons from the de-excitation of $^{16}$O from neutral-current neutrino-nucleon scattering. The NUANCE simulation provides a comprehensive estimate of various neutrino interactions and includes final state intranuclear interactions. The estimated contribution to this data set from such events passing all selection cuts is $15.8^{+21.3}_{-4.6}$ neutrons and $3.2^{+4.6}_{-4.4}$ $\gamma$-rays.

Events that produce two or more neutrons within short time intervals can serve as a test of the background contributions from atmospheric neutrinos, spontaneous fission, and $^2$H$(n, 2n)^1$H. Analysis of burst data taken from the full data set compared to Monte Carlo predictions show an excess of high-multiplicity bursts in the neutrino data. A burst is defined as two or more events, passing all neutrino selection criteria, that occur within a 50 ms time interval. A likelihood calculation indicates that, if the MC accurately describes the data, the probability of obtaining a worse likelihood is 1.6%. Uncertainties in hadron transport and intranuclear reactions for atmospheric neutrino interactions are considered the likely cause of the deficit of high-multiplicity events in the MC prediction. In estimating the uncertainty associated with the single neutron events from atmospheric neutrino interactions, the upper uncertainty has been conservatively taken to encompass the difference between the data and the Monte Carlo prediction.

Neutrons and $\gamma$-rays produced at the acrylic vessel and in the light water can propagate into the fiducial volume. During construction of the acrylic vessel, Rn progeny accumulated on its surfaces. These daughters can initiate ($\alpha$,n) reactions on $^{13}$C, $^{17}$O, and $^{18}$O. External $\gamma$-rays originating from ($\alpha, n\gamma$) and ($\alpha, p\gamma$) processes and radioactivity in the construction material of the detector and the rock cavity can enter the D$_2$O target and photodisintegrate deuterons. The radial distribution of these neutron sources differs from those of the NC signal and of photodisintegration neutrons produced from radioactivity in the D$_2$O target. The enhanced neutron detection efficiency of the salt phase makes it possible to extract the external-source neutron contribution in the neutrino signal window by including an additional radial distribution function in the statistical analysis of the solar neutrino flux. Details of the extraction of this background can be found in Sec. IX. Additional tests, including direct counting of the $\alpha$ activity on the surface of the acrylic and the search for coincident events generated by specific nuclear reactions associated with the ($\alpha$,n) reaction, were performed. The main source of coincidence events is the $e^+e^-$ pairs from the excited state at 6.05-MeV in $^{16}$O, in coincidence with a fraction of the neutrons produced by $^{13}$C$(\alpha,n)^{16}$O. A weaker source is the two neutrons from $^2$H$(n, 2n)^1$H induced by fast neutrons from ($\alpha$,n) reactions.

The results of these measurements are limited by statistics. The sum of this $\alpha$-induced neutron background and the photodisintegration neutron background produced by radioactivity in the H$_2$O and the AV is consistent with the results from the radial fit technique.

At the depth of SNO, only neutrinos and muons from cosmic rays survive. Neutrons and other cosmogenic activity are produced from muon capture, muon electrodisintegration, and from muon nuclear spallation. The 20-second veto following a tagged muon event removes most subsequent activity. However, longer-lived spallation products, such as $^{16}$N, can survive this cut. A limit of less than 1.3 $^{16}$N events (68% CL) was determined by analysis of long-lived activity present within 50 seconds after a muon event. Activity from other spallation products is estimated to contribute less than one event in the

data set.

A small number of neutrons can also be created by $\bar{\nu}_e$ reactions from nuclear reactors. The estimate of this background is based on the average power output of all commercial reactors within 500 km of SNO and an average reactor $\bar{\nu}_e$ spectrum. Electron antineutrinos from terrestrial radioisotopes do not contribute significantly to the background because their energies are below threshold for the CC reaction on $^2$H ("ccd") and can only initiate CC reactions on $^1$H ("ccp") and NC reactions on $^2$H ("ncd"). The total estimated background contributions from reactor and terrestrial $\bar{\nu}_e$ interactions are 2.0±0.3 and 0.5±0.1 detected neutrons, respectively.

SNO is slightly sensitive to solar CNO neutrinos generated by the electron capture decay of $^{15}$O and $^{17}$F, and this contributes 0.4 ± 0.4 neutrons [37].

None of the backgrounds discussed in this section depend on the solar zenith angle. Thus, the contribution of these backgrounds to the day and the night data sets can be determined by normalizing to the respective live times.

## VIII. SYSTEMATICS ASSOCIATED WITH THE DAY-NIGHT ASYMMETRY MEASUREMENT

Differences in day and night neutrino fluxes are a prediction of matter-enhanced neutrino oscillations. Day-night results are reported as asymmetry ratios in the measured neutrino fluxes. The asymmetry ratio for a flux is defined as $A = 2(\phi_N - \phi_D)/(\phi_N + \phi_D)$. An advantage of the asymmetry ratio is that most systematics cancel and only systematic effects that scale day and night fluxes by different factors need to be considered.

Day-night systematics can be divided into four general classes. *Diurnal systematics* are variations in detector response over a 24-hour timescale, such as might be caused by diurnal changes in the laboratory environment. Because the SNO detector is located far underground, it is isolated from many diurnal effects. Day-night differences in detector response are therefore not expected, but limits must be placed on their size. *Directional systematics* arise because the SNO detector is not completely spherically symmetric, and because the directions of electrons from CC or ES neutrino interactions are correlated with the time of day. ES events in particular are highly directional, and so ES events at night will preferentially illuminate the upper half of the detector, while during the day they illuminate the bottom half. If there are differences in the up-down response of the detector, these directional differences can create effective differences in the day and night rates. Directional systematics are expected to be important for ES events, but are greatly suppressed for CC events, which have only a weak directional correlation with the direction from the Sun. Directional systematics do not produce day-night systematic effects for directionally isotropic events such as neutrons or backgrounds. *Miscellaneous systematics* include possible day-night differences in cut acceptance, uncertainties in the live time calculation, and long-term variations in detector response. These can produce differences in the time-averaged day and night detector responses if the long-term

TABLE XIII: Day-night differences for selected muon-induced neutron distributions.

| Quantity | Night value | Day value | Asymmetry ratio (%) |
|---|---|---|---|
| Event rate (day$^{-1}$) | 3.50 ± 0.09 | 3.56 ± 0.10 | −1.83 ± 3.81 |
| Mean energy (MeV) | 5.78 ± 0.06 | 5.67 ± 0.06 | 1.96 ± 1.49 |
| Energy width (MeV) | 1.47 ± 0.06 | 1.47 ± 0.06 | 0.00 ± 4.69 |
| Mean isotropy ($\beta_{14}$) | 0.311 ± 0.004 | 0.312 ± 0.005 | −0.24 ± 2.03 |
| Capture time (ms) | 4.9 ± 0.3 | 4.6 ± 0.3 | 7.27 ± 8.36 |

variations are correlated with the seasonal variations in the day-night live time exposure. *Background systematics* reflect uncertainties in the magnitude and day-night asymmetries of the various background sources. The following sections describe how each class of systematics is measured.

### A. Diurnal Systematics

Diurnal systematics are variations in detector response with a 24-hour periodicity. A strictly hypothetical example would be diurnal variations in the laboratory's temperature, which in principle could change the response of the SNO electronics if there were uncompensated temperature dependencies. Because the timescale for diurnal variations is much shorter than the average interval between calibrations, diurnal stability must be evaluated using classes of events that are continually present in the detector. These primarily consist of secondary neutrons produced in the $D_2O$ by through-going muons and Cherenkov events from low-energy $\beta$-$\gamma$ decays.

Muons traversing the acrylic vessel can produce secondary neutrons by a variety of processes, including photodisintegration of deuterons and nuclear spallation. These neutrons are produced uniformly throughout the $D_2O$ and at an essentially constant rate on a diurnal timescale, and so mimic the solar NC signal in spatial and temporal distributions. Small diurnal and seasonal variations of a few percent in the predicted muon rate, expected as a result of variations in the scale height of the atmosphere, are neglected. Secondary neutrons from muons are selected by identifying bursts of events inside the $D_2O$ that occur within a time window of 50 $\mu$s - 20 ms following a tagged muon event. Spallation events can occasionally produce very large bursts of neutrons. To prevent such bursts from biasing the spatial or temporal distributions of the neutrons, a multiplicity selection requiring less than 15 events in the bursts is applied to the neutron selection.

Table XIII shows the mean day and night values for various distributions of muon-induced secondary neutrons. The event rate, mean event energy, width of the neutrons' energy distribution, mean value of the $\beta_{14}$ isotropy parameter, and neutron capture time are all consistent between day and night. The left side of Fig. 21 shows the day-night asymmetry on each measured quantity.

While muon-induced secondary neutrons demonstrate the diurnal stability of the detector, they are statistically limited

TABLE XIV: Combined day-night asymmetries for various background regions. The asymmetry ratio is formed by combining the measured day-night asymmetries for each run with both day and night data.

| Background region | Combined asymmetry ratio |
|---|---|
| $D_2O$ | $-0.045 \pm 0.070$ |
| AV hot spot | $-0.022 \pm 0.048$ |
| Shell around AV | $-0.023 \pm 0.022$ |
| $H_2O$ | $0.003 \pm 0.016$ |
| PMTs | $0.009 \pm 0.011$ |

by the low muon rate ($\sim 3$/hour). Better limits on most parameters may be obtained from studies of intrinsic detector radioactivity. These include Cherenkov events from $\beta$-$\gamma$ decays of low-energy radioactivity in the $D_2O$, acrylic, $H_2O$, or PMTs.

A localized region of higher-than-average background radioactivity was discovered on the upper surface of the acrylic vessel. The origin of this "AV hot spot" is uncertain, but it was presumably introduced by radioactive contamination during construction. If composed of Th, the total amount is approximately 10 $\mu$g, and is not a significant neutron source given the location. However, this hot spot provides an excellent check of position reconstruction for a point source of events. Comparisons of the reconstructed day and night positions of the AV hot spot show that its position is stable to within $\pm 0.3\%$ in radius between night and day, and indicate that the vertex resolution for a point source differs by no more than $\pm 1.26$ cm between night and day.

Because low-energy background events have steeply falling energy spectra near and below the analysis threshold, small variations in energy scale or energy resolution produce large changes in the observed rate inside a low-energy window. Measurements of diurnal rate stability for low-energy radioactivity can thus be used to limit diurnal variations in energy scale and energy resolution.

In order for this procedure to work, the actual level of radioactivity must be diurnally constant. Radioactivity inside the PMTs or acrylic is immobile, and presumed to be constant except for possible slow decay. Radioactivity in the $D_2O$ and $H_2O$ can fluctuate over time due to radon ingress, as is seen in the *in-situ* radioactivity measurements, but the timescale for these changes is generally long compared to the 12-hour differences being sought in this analysis. These longer-term variations in radioactivity can be mitigated by calculating a day-night asymmetry for each individual run that includes both day and night live time (implicitly assuming that the radioactivity is constant over the several hour duration of a typical run). Assuming the real radioactivity level does not vary significantly over this short time period, any observed rate variation would indicate a diurnal difference in detector response. The run-by-run asymmetries can be combined in a weighted average using a maximum likelihood technique to determine an overall limit on the rate asymmetry of each source.

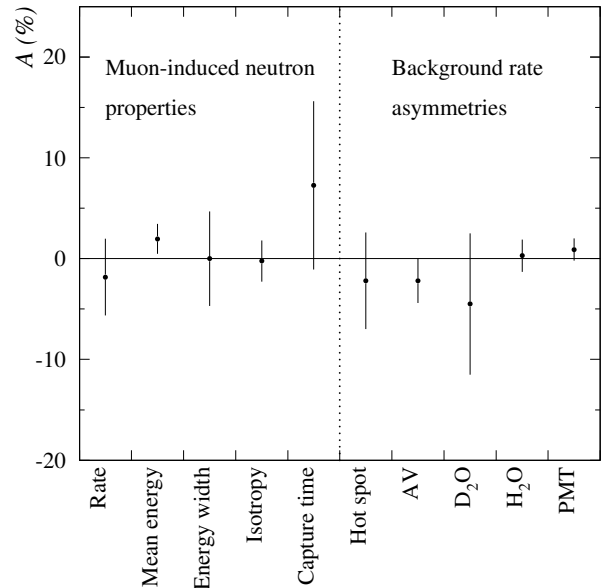The right side of Fig. 21 shows the combined run-by-run



FIG. 21: Day-night asymmetries of selected muon-induced neutron properties and background rates. The day-night asymmetries for the muon-induced neutron properties are calculated for events in the full day and night data sets. The day-night asymmetries of the background rates are determined by combining the calculated asymmetry of each individual data run. Each data run lasted for less than 24 hours.

asymmetries for radioactivity in five different regions of the detector: in the AV hot spot, in a spherical shell around the AV (excluding the hot spot), in the light and heavy water, and near the PMTs. Events used to calculate these asymmetries were selected from an energy region corresponding to $N_{prompt}$ between 25 and 40 (approximately $4.1 < T_{eff} < 6.2$ MeV).

Table XIV shows the asymmetries for each of these background regions. All are consistent with no asymmetry. The analysis was repeated, this time calculating day-night asymmetry ratios for sets of 24-hour periods instead of for each run, and similar results were obtained. The insensitivity to the length of the normalization period of the asymmetry, and the fact that asymmetries in all regions of the detector are consistent with zero, make it very unlikely there are diurnal variations in the detector response.

While the rate asymmetries on radioactivity in the $H_2O$ and near the PMTs have the smallest uncertainties, these regions are far from the fiducial volume of the neutrino analysis. A more representative approach is to base the energy scale and resolution variation estimates on the rate of radioactivity in the spherical shell around the AV. This region has adequate statistics, is at a similar radius compared to neutrino events, and includes a significant fraction of acrylic radioactivity which should be diurnally constant. (This region also contains events from thin shells of $D_2O$ and $H_2O$ adjoining the AV.) Allowing the rate asymmetry for this region to vary within its measured

limits, and assuming that the entire variation is due to changes in energy scale, the diurnal energy scale variation is limited to ±0.4%. Assuming instead that the entire variation is due to changes in energy resolution, the diurnal energy resolution variation can be limited to ±0.5%. These results are consistent with limits derived from the other regions of radioactivity and with the more direct measurements from muon-induced neutrons given in Table XIII.

*In-situ* radioactive background measurements can also place limits on diurnal variations in event isotropy. Comparison of the mean day and night $\beta_{14}$ values for events in the spherical shell around the AV results in the limit $|\beta_{14,night} - \beta_{14,day}| < 0.006$. This limit is comparable to the independent limit of 0.0064 derived from muon-induced neutrons (Table XIII), and the two limits may be combined to limit the diurnal shift in the mean $\beta_{14}$ value to $< 0.0043$.

### B. Directional Systematics

As described near the start of this section, variations in detector response with the direction of the event can produce a day-night systematic for neutrino signals that have different directional distributions for night and day. The PDFs for the direction of electrons produced by CC and ES interactions with respect to the Sun's direction are shown in Fig. 23(b). Because the $\gamma$-rays emitted by neutron captures have random directions, detector asymmetries produce no day-night variations for NC events.

Variations in detector response with direction are measured with 6.13-MeV $\gamma$-rays from the $^{16}$N source. Events are grouped by bins in $\cos\theta$ and $\phi$ in detector coordinates. For each bin, the means of each of the eight event variables listed in Table XV are calculated. $^{16}$N calibration runs at different positions in the heavy water are combined in a volume-weighted average. The result is a map of the detector response versus directional bin for each systematic.

Monte Carlo calculations predict how many CC and ES events fall in each directional bin for SNO's live time exposure for both night and day. By convolving the MC prediction for the directional distribution in both time bins with the measured detector asymmetry, the mean value of a detector response function is calculated for the night and day data sets. The volume-weighted difference between the night and day values gives a measure of the directional systematic for each neutrino signal.

Table XV gives the limits on the effective day-night difference in detector response for CC and ES events resulting from directional asymmetries.

### C. Miscellaneous Systematics

The uncertainties on the day and night live times are calculated to be ±0.021%. These result in a 0.03% uncertainty on the day-night asymmetry.

The cuts used to reject instrumental backgrounds are described in Sec. III B. The time variability in the fraction of

TABLE XV: Directional day-night systematics for CC and ES events. The day-night effect of directional systematics for NC and background events is zero.

| Systematic | Limit for CC events | Limit for ES events |
|---|---|---|
| Energy scale | ±0.09% | ±0.79% |
| Energy resolution | ±0.13% | ±1.3% |
| Radial shift | ±0.02% | ±0.15% |
| Vertex resolution | ±0.13% | ±1.4% |
| Angular resolution, $\alpha_M$ | ±1.4% | ±11.6% |
| Angular resolution, $\beta_M$ | ±0.7% | ±6.1% |
| Angular resolution, $\beta_S$ | ±0.6% | ±5.2% |
| Isotropy | ±0.09% | ±0.82% |

good events removed can be measured by applying the cuts to muon-induced secondary neutrons. The day-night asymmetry of the fraction of good events removed by the cuts is measured to be $A = 0.18 \pm 0.33$. Note that this is an asymmetry on a very small loss fraction.

In addition to diurnal variations in detector response (see Sec. VIII A), variations on longer timescales could exist. Such variations can indirectly introduce differences in the day-night detector response if they correlate with seasonal variations in the day-night live time exposure. For example, if the energy scale were slightly mis-calibrated during the winter months, this miscalibration would affect the night data set more than the day data, since during the winter more night data is collected than day data due to the seasonal variation in the lengths of night and day. The effects of these variations can be constrained by constructing worst-case models that systematically over-estimate the measured response in summer and under-estimate it during the winter, or vice versa. These worst-case models were constructed for energy scale and isotropy variations using the regular calibration points taken with the $^{16}$N source and their effect is shown in Tables XXV and XXVII as long term variations in these parameters.

### D. Day-Night Background Systematics

Uncertainties in backgrounds to the neutrino signals can produce day-night systematics in two ways. First, there may be uncertainty in the day-night variation of the background (i.e., an uncertainty on the rate asymmetry $A$ of the background). This uncertainty will differentially affect the amounts of background subtracted from the night and day data sets. Second, the uncertainty on the total amount of background (night+day) results in an uncertainty on the average neutrino flux, which enters into the denominator of the day-night ratio. Generally, the uncertainty on the asymmetry is a larger effect than the uncertainty on the amount of background, but both contribute.

Details of the day-night calculations of the background totals have been given previously. The reader is referred to the discussion of the individual backgrounds in Sec. VII.

## IX. NEUTRINO SIGNAL DECOMPOSITION

Extraction of the electron energy spectrum, flux and day-night asymmetry of the $^8$B solar neutrinos is carried out via an extended maximum likelihood fit of the event variables in the 4722-event data set by MC generated PDFs. The data variables utilized are $T_{\text{eff}}$, $\rho$, $\cos\theta_\odot$, and $\beta_{14}$, and their distributions are shown in Figs. 22 and 23.

In order to obtain the electron energy spectra of CC and ES interactions, PDFs were created for $T_{\text{eff}}$ intervals which spanned the range from 5.5 MeV to 13.5 MeV in 0.5 MeV steps. For $T_{\text{eff}}$ values between 13.5 and 20 MeV, a single bin was used. Minor adjustments were applied to the PDFs to take into account signal loss due to instrumental cuts not modeled by the simulation (Fig. 2). PDF normalizations for CC and ES components were separately allowed to vary in each $T_{\text{eff}}$ bin to obtain model-independent spectra. Only the overall normalizations of NC and external neutron components were allowed to vary since their $T_{\text{eff}}$ spectra are simply determined by the energy release following neutron capture on $^{35}$Cl or $^2$H.

The parameter $\beta_{14}$ is correlated with $T_{\text{eff}}$ and, to a lesser extent, with $\rho$. Similarly, $\cos\theta_\odot$ is weakly correlated with $T_{\text{eff}}$ and $\rho$. These dependencies were taken into account through the use of a multi-dimensional PDF $P(T_{\text{eff}}, \beta_{14}, \rho, \cos\theta_\odot)$ factorized as follows:

$$P(T_{\text{eff}}, \beta_{14}, \rho, \cos\theta_\odot) = P(T_{\text{eff}}, \beta_{14}, \rho) \times P(\cos\theta_\odot | T_{\text{eff}}, \rho), \quad (12)$$

where the first factor is just the 3-dimensional PDF for the variables $T_{\text{eff}}$, $\beta_{14}$, and $\rho$, while the second factor is the conditional PDF for $\cos\theta_\odot$ given $T_{\text{eff}}$ and $\rho$. This approach explicitly preserves all correlations between the four relevant parameters with the exception of the correlation between $\cos\theta_\odot$ and $\beta_{14}$, which is assumed to be linked only through $T_{\text{eff}}$ and $\rho$.

To confirm our understanding of these correlations and to verify the results with an independent approach, extraction of solar neutrino results has also been performed with the 3-dimensional PDF in Eq. 12 further reduced to the following formulation:

$$P(T_{\text{eff}}, \beta_{14}, \rho, \cos\theta_\odot) = P(T_{\text{eff}}, \beta_{14}) \times P(\cos\theta_\odot) \times P(\rho). \quad (13)$$

The signal extraction procedure was applied to 100 simulated data sets each generated to simulate the expected characteristics of the data. It was found that the parameterization in Eq. (13), which ignored the correlations with $\rho$ and $\cos\theta_\odot$, resulted in a small bias compared with the approach in Eq. (12). As a further cross-check, both approaches were applied to the data and yielded results that were consistent with this interpretation. After applying corrections for the expected bias, the results were found to be nearly identical. The average difference in the extracted CC signal between the two factorization approaches, after corrections, is less than 1%.

In the flux measurement, a "constrained" fit, in which the CC energy spectral shape is fixed as an undistorted $^8$B spectrum [38], and an "unconstrained" fit, in which this constraint is removed, are carried out. The constrained analysis is useful in testing the null hypothesis of neutrino flavor transformation under the assumption of an undistorted $^8$B solar neutrino
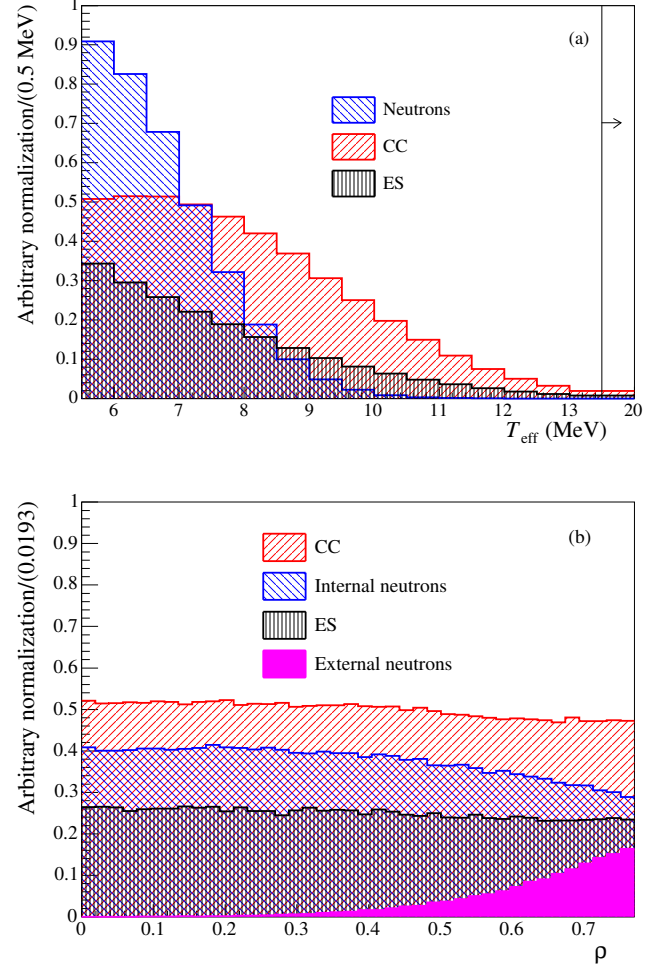


FIG. 22: (a) $T_{\text{eff}}$ and (b) $\rho$ distributions for CC, ES, NC and external neutron events. Where internal and external neutron distributions are identical the distribution is simply labeled neutrons. Note that the distribution normalizations are arbitrary and chosen to allow the shape differences to be seen clearly. The CC energy spectrum shape corresponds to an undistorted $^8$B model.

spectrum. The unconstrained analysis has the advantage that this model assumption is removed.

Compared to the pure $D_2O$ phase, the addition of salt increases the sensitivity at large radius to neutron capture (see Fig. 14) making it possible to detect background neutrons originating at or near the AV. As shown in Fig. 22(b), the differing radial profiles allow external neutrons to be separated from neutrons generated within the $D_2O$ volume. In the pure $D_2O$ phase analysis [4], the amplitudes of the photodisintegration neutron backgrounds from internal radioactivity in the AV and the $H_2O$ were fixed in neutrino signal decomposition. In the current analysis, the $\rho$ distribution provides discrimination between the external neutron and the signal flux contributions. The external neutron component is measured simultaneously with the flux signals from the likelihood fit.
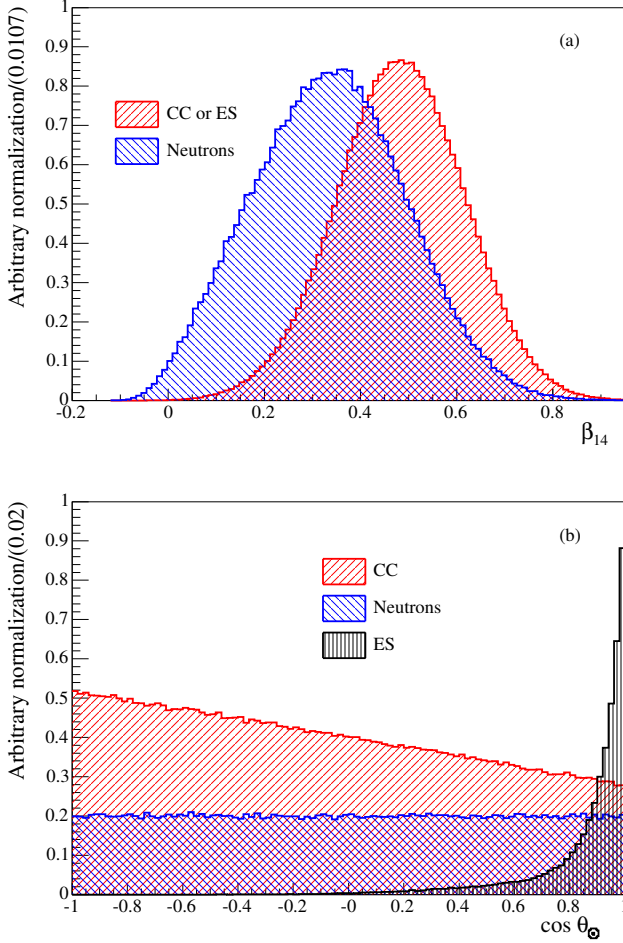
In the salt phase analysis, the amplitude of the $\rho$ PDF of

FIG. 23: (a) $\beta_{14}$ and (b) $\cos\theta_\odot$ distributions for CC, ES, NC and external neutron events. Where internal and external neutron distributions are identical the distribution is simply labeled neutrons. Note that the distribution normalizations are arbitrary and chosen to allow the shape differences to be seen clearly.

the external source neutrons is allowed to vary in the maximum likelihood fit. If the production rates of these external neutron backgrounds were constant, they would contribute an amount smaller than the systematic uncertainties reported in the earlier pure $D_2O$ phase analysis.

Results from the measurements of the radioactive backgrounds (Sec. VII) were incorporated in the extraction of solar neutrino signals. The internal photodisintegration neutron backgrounds are subtracted from the fitted NC event total. A separate PDF for internal $\gamma$-rays from atmospheric neutrino interactions was included with a normalization fixed to 3.2 events (in accordance with Table X) and with a shape based on events generated by the $^{16}$N calibration source because of their similarity. Other backgrounds, listed in Table XVI, were treated as systematic uncertainties applied to the appropriate $T_{\rm eff}$ intervals for CC and NC components following signal extraction. The distinctive dependence of ES events on $\cos\theta_\odot$ was assumed to reduce the effect of these backgrounds on the

TABLE XVI: Additional background contributions treated as systematic uncertainties applied to appropriate $T_{\rm eff}$ intervals in the CC and NC spectra. Note that the $T_{\rm eff}$ range for the first bin is 5.5-6.0 MeV.

| Systematic parameter | $1\sigma$ limits |
|---|---|
| Internal $\gamma$ bkgd. | $\pm$ 2.2 events |
| Internal Cherenkov bkgd. - Tl | $\leq$ 0.53 events (1st CC bin) |
| Internal Cherenkov bkgd. - Bi | $\leq$ 2.29 events (1st CC bin) |
| Internal Cherenkov bkgd. - Na | $\leq$ 0.90 events (1st CC bin) |
| External Cherenkov bkgd.- PMT | $\leq$ 11.0 events (1st CC bin) |
| External Cherenkov bkgd.- $H_2O$ | $\leq$ 3.0 events (1st CC bin) |
| External Cherenkov bkgd.- AV | $\leq$ 7.0 events (1st CC bin) |
| AV events | $\leq \frac{6.55}{2}$ events (1st CC bin) |
| | $\leq \frac{6.55}{2}$ events ($T_{\rm eff}$ >6.5 MeV) |
| Instrumental bkgd. | $\leq$ 3 events (across $T_{\rm eff}$ range) |

ES results to negligible levels.

Day-night asymmetries are determined for both the constrained and unconstrained fit cases. As described below, asymmetries are calculated both allowing all signal fluxes to vary and with the NC asymmetry constrained to zero.

The maximum likelihood fit returns the estimated numbers of CC, NC, ES, and external neutron events, with statistical uncertainties. Final fluxes are determined by normalizing to the solar-model prediction calculated by MC simulation with several correction factors, summarized in Table XVII, applied. Additional corrections are applied to adjust the predicted event rates as a result of CC interactions on $^{17}$O, $^{18}$O, $^{23}$Na, and $^{35,37}$Cl, which are not modeled in the MC simulation. The MC model uses the Effective Field Theory (EFT) calculation in Ref. [39] to obtain the neutrino-deuteron cross sections. This EFT calculation is normalized to the standard potential-model calculation [40, 41] by fixing the two-body axial exchange-current counter term $L_{1,A}$. Corrections are applied to the flux results to account for small differences in the choices of the axial coupling constant $g_A$ [42] that were used in the theoretical calculations, and for normalization to the improved potential-model calculation [41] (the EFT calculation was done with $L_{1,A}$ = 5.6 fm$^3$). The values of the fundamental constants [43] used in the present calculations of the cross sections, together with correction factors derived to bring the cross section calculations in accordance with those constants, are listed in Table XVII. Radiative corrections included in [41] were taken out, and the corrections of Kurylov *et al.* [44], parametrized as follows, were applied to the CC, NC and ES cross sections:

$$\omega_{\rm CC} = 1.0318 - 7.45 \times 10^{-4} E_e + 4.72 \times 10^{-6} E_e^2 \quad (14)$$

$$\omega_{\rm NC} = 1.0154 \quad (15)$$

$$\omega_{\rm ES} = 0.9764 - 7.81 \times 10^{-4} T_{\rm eff}$$
$$- 1.31 \times 10^{-4} T_{\rm eff}^2 + 3.64 \times 10^{-6} T_{\rm eff}^3, \quad (16)$$

where $E_e$ is the true total energy of the electron. Table XVII also includes the corrections to the CC, ES, and NC fluxes from CC interactions on oxygen, sodium, and chlorine, by which, together with the radiative corrections, the EFT and ES cross sections were multiplied before comparing with the data to extract the fluxes.

TABLE XVII: Fundamental constants used in the MC and post-fit correction factors to the neutrino flux in different reaction channels. The radiative correction functions are discussed in the text.

| Constants used | | | |
|---|---|---|---|
| $g_A$ | 1.2670(30) | | |
| $G_F$ | $1.16639(1) \ 10^{-5} \ \text{GeV}^{-2}$ | | |
| $L_{1,A}$ | $4.0 \ \text{fm}^3$ | | |
| $\sin^2 \theta_W(\overline{\text{MS}})$ | 0.23113(15) | | |
| Correction | CC | ES | NC |
| CC on O, Na and Cl | 1.0081 | 1.0 | 1.0 |
| Radiative corrections | $\omega_{\text{CC}}$ | $\omega_{\text{ES}}$ | $\omega_{\text{NC}}$ |



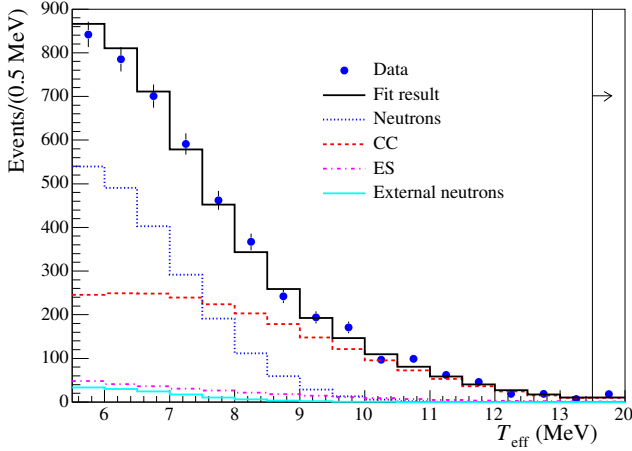FIG. 24: Data $T_{\text{eff}}$ spectrum with statistical uncertainties. Included are MC spectra for neutron, CC, ES, and external neutron distributions. Note that an undistorted $^8$B spectral shape has been assumed and each MC contribution has been normalized to the number of corresponding fit events measured by the energy-constrained signal extraction.

The flux measurements are presented in terms of the CC, NC, and ES signals and as the flux of electron type ($\phi_e$) and non-electron type ($\phi_{\mu\tau}$) active neutrinos. In general, the effects of systematic uncertainties are evaluated by re-fitting the data after perturbing the model PDFs by the $1\sigma$ uncertainties determined from calibration and background measurements. The differences between the nominal flux fit values and those obtained with the systematically shifted PDFs are quoted as 68% C.L. uncertainties.

Figure 24 shows the energy spectrum, with statistical uncertainties, of the data that passes all selection cuts. Included in the figure are MC generated spectra for CC, ES, internal neutron, external neutron components, and their sum. Note that the MC generated distributions correspond to an undistorted $^8$B neutrino spectrum and each spectrum has been normalized to correspond to the total number of fit events for the given component as extracted by the energy-constrained fit.





FIG. 25: (a) Extracted CC $T_{\text{eff}}$ spectrum. Systematic uncertainties have been combined in quadrature and include only the effect of PDF shape change. (b) Extracted CC $T_{\text{eff}}$ spectrum with statistical error bars compared to predictions for an undistorted $^8$B shape with combined systematic uncertainties, including both shape and acceptance components. The systematic error bands represent the fraction of the total uncertainty attributable to the given quantity.

## X. SPECTRUM

Figure 25(a) shows the CC energy spectrum extracted from the energy-unconstrained fit. The PDF shape change component (see below) of the systematic uncertainties is added in quadrature with the statistical error to provide a combined error for each bin. The analogous ES spectrum is presented in Fig. 26(a).

Systematic uncertainties on the extracted CC energy spectrum are calculated by separately varying the PDFs according to the estimated $1\sigma$ uncertainties on the detector parameters. Signal extraction is then repeated and the differences between the nominal fit values and shifted PDF fit values taken as the spectrum systematic uncertainties.

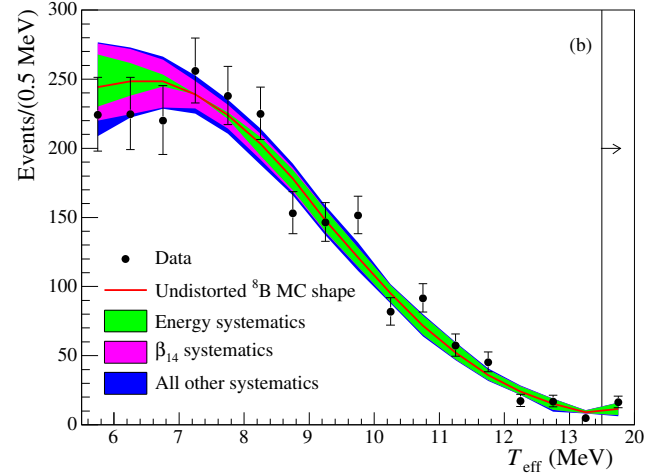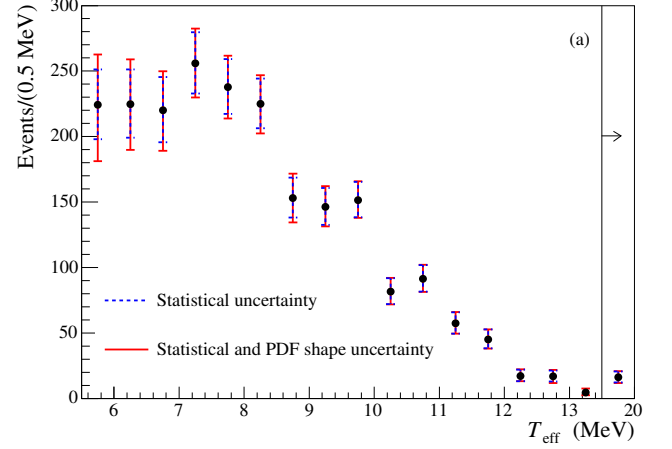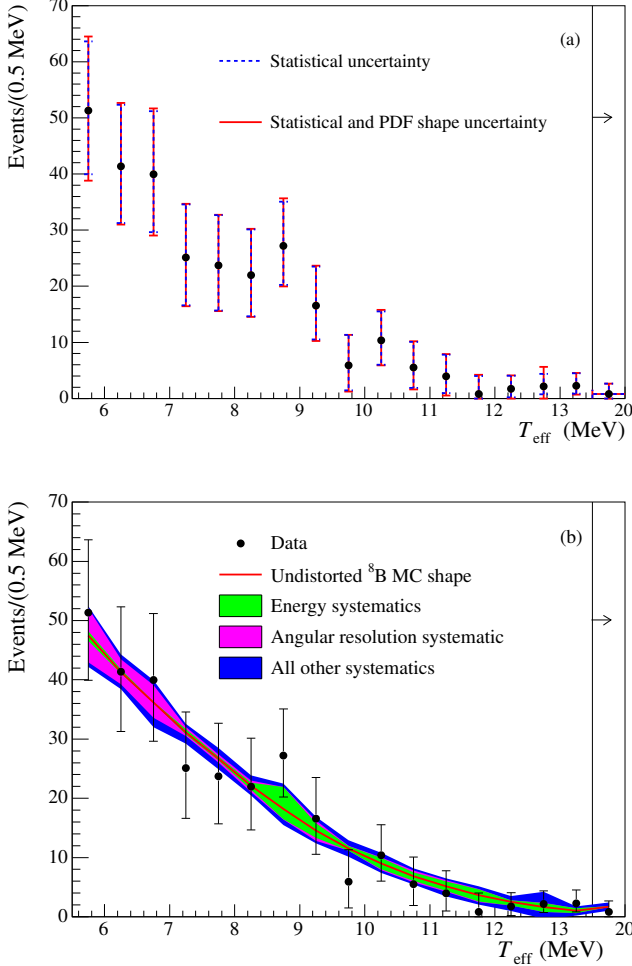Systematic uncertainties on the spectrum are divided into

FIG. 26: (a) Extracted ES $T_{\rm eff}$ spectrum. Systematic uncertainties have been combined in quadrature and include only the effect of PDF shape change. (b) Extracted ES $T_{\rm eff}$ spectrum with statistical error bars compared to predictions for an undistorted $^8$B shape with combined systematic uncertainties, including both shape and acceptance components. The systematic error bands represent the fraction of the total uncertainty attributable to the given quantity.

those caused by changes to the PDF shapes, and those resulting from uncertainties in overall acceptance. The former lead to errors in the fitted number of charged current events in each spectral bin, while the latter lead to errors in the translation of differential event counts into differential neutrino fluxes. For example, shifting the energy scale alters both the PDF shapes and the acceptance in each bin, while a change in the radial scale (and hence the effective fiducial volume) primarily affects the acceptance. For a particular neutrino spectrum model, the fitting uncertainties from the PDFs shapes and the uncertainties on the acceptance have correlations with each other which must be taken into account when calculating bin-by-bin neutrino fluxes. A list of these uncertainties is given in Table XVIII for the $T_{\rm eff}$ intervals $5.5 - 6.0$ MeV, $7.0 - 7.5$ MeV and $9.0 - 9.5$ MeV. Note that an undistorted $^8$B shape

TABLE XVIII: CC spectrum combined shape and acceptance systematic uncertainties for three sample energy ranges. An undistorted $^8$B shape has been assumed. Note that the full table is given in the Appendix.

| Source | CC differential uncertainty (%) | | |
|---|---|---|---|
| | (5.5–6.0 MeV) | (7.0–7.5 MeV) | (9.0–9.5 MeV) |
| Energy scale (const.) | -8.0, 9.5 | 0.6, 0.0 | 4.7, -5.0 |
| Energy scale (E dep.) | -1.5, 1.6 | -0.4, 0.6 | 1.3, -0.4 |
| Energy radial bias | -5.7, 6.1 | 0.1, -0.1 | 3.8, -2.9 |
| Energy resolution | 4.9, -4.9 | -0.1, 0.1 | -2.6, 2.6 |
| $\beta_{14}$ scale | 7.1, -8.4 | 4.4, -4.6 | 1.1, -1.7 |
| $\beta_{14}$ width | -0.9, -0.1 | 0.0, -0.2 | 0.3, -0.2 |
| Radial scale (const.) | -2.6, 2.5 | -2.4, 2.6 | -2.5, 2.8 |
| Radial scale (E dep.) | 0.2, -0.2 | -1.2, 1.2 | -2.1, 2.1 |
| Vertex $x$ | -0.3, 0.0 | -0.5, 0.0 | 0.1, -0.1 |
| Vertex $y$ | -0.2, -0.3 | -0.2, 0.0 | 0.1, 0.4 |
| Vertex $z$ | -0.4, -0.2 | 0.2, -0.6 | -0.3, -0.1 |
| Vertex resolution | -0.4, 0.4 | -0.3, 0.3 | 0.4, -0.4 |
| Angular resolution | -0.2, 0.2 | 0.1, -0.1 | -0.6, 0.6 |
| Internal $\gamma$ | 0.4, -0.6 | 0.1, -0.1 | 0.0, 0.0 |
| Selection efficiency | -0.2, 0.2 | -0.1, 0.2 | -0.1, 0.2 |
| Backgrounds | -8.5, 0.0 | -0.1, 0.0 | -0.1, +0.0 |

has been assumed for generation of these uncertainties. The complete table of uncertainties for all energy bins is included in the Appendix.

Figure 27 shows the CC spectrum PDF shape systematic effects and combined systematics for each of the four energy-related systematic uncertainties versus $T_{\rm eff}$ under the assumption of an undistorted $^8$B shape. Figures 25(b) and 26(b) show the extracted CC and ES spectra as a functions of $T_{\rm eff}$, with statistical error bars on the data, and combined systematic uncertainty error bands centered on the prediction for an undistorted $^8$B shape (normalized to the data). Note that the error bands correspond to the fraction of the total error, calculated as the ratio of the square of the given uncertainty to the square of the total, attributed to the indicated source (e.g., $\beta_{14}$ systematic errors).

## XI. SOLAR NEUTRINO FLUX RESULTS

As described in a previous section, a statistical analysis to separate the neutrino candidate events into CC, NC, ES, and external-source neutrons was performed using an extended maximum likelihood technique using the $\beta_{14}$, $\cos\theta_\odot$ and $\rho$ distributions. The extended maximum likelihood analysis yielded $2176\pm78$ CC, $279\pm26$ ES, $2010\pm85$ NC, and $128\pm42$ external-source neutron events (recall that 125.4 internal neutrons and 3.5 internal $\gamma$-ray events have been subtracted off). Note that a fixed *hep* contribution of $9.3 \times 10^3$ cm$^{-2}$ s$^{-1}$ has been assumed. The systematic uncertainties on the derived fluxes for this "energy-unconstrained" fit are shown in Table XIX. The $\beta_{14}$, $\cos\theta_\odot$, and $\rho$ distributions for the selected events are presented in Fig. 28 with only statistical uncertainties shown.

For the unconstrained analysis, the quoted CC and ES fluxes are the equivalent fluxes of $^8$B electron-neutrinos, assuming an undistorted $^8$B energy spectral shape, that would
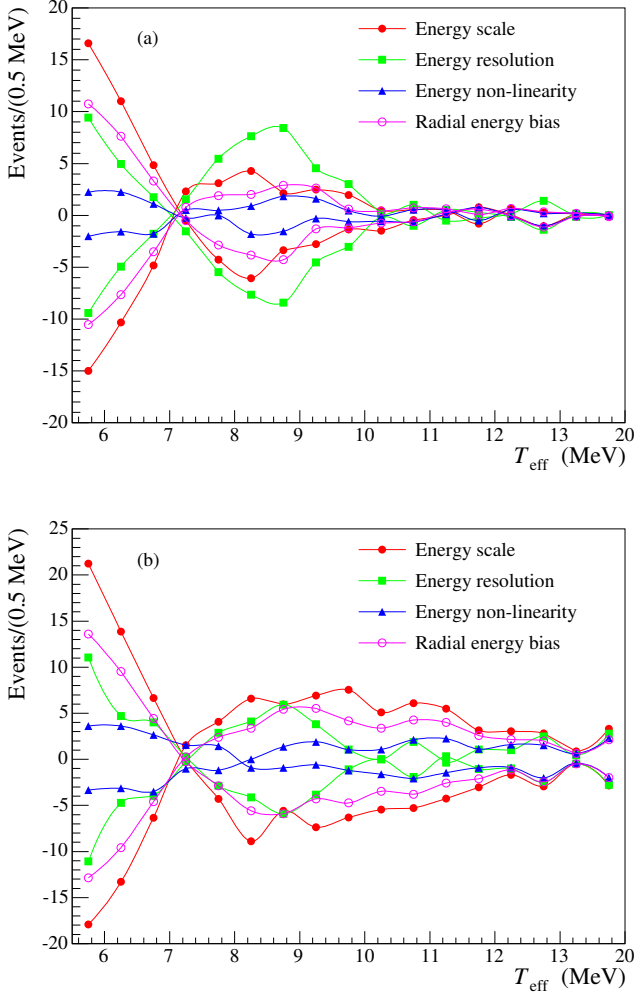
FIG. 27: (a) PDF shape change contributions and (b) total contributions from energy-related systematic energy uncertainties to the extracted CC spectrum assuming an underlying, undistorted $^8$B shape.

produce the same CC and ES event rates above the analysis threshold of $T_{\rm eff}$ = 5.5 MeV. For the NC case, the quoted flux is the flux of all active neutrino types that would produce the same NC rate above the reaction threshold of 2.2 MeV. The fitted numbers of events give the equivalent $^8$B fluxes [46, 47] (in units of $10^6$ cm$^{-2}$s$^{-1}$)

$$\phi_{\rm CC}^{\rm uncon} = 1.68^{+0.06}_{-0.06}({\rm stat})^{+0.08}_{-0.09}({\rm syst})$$

$$\phi_{\rm ES}^{\rm uncon} = 2.35^{+0.22}_{-0.22}({\rm stat})^{+0.15}_{-0.15}({\rm syst})$$

$$\phi_{\rm NC}^{\rm uncon} = 4.94^{+0.21}_{-0.21}({\rm stat})^{+0.38}_{-0.34}({\rm syst}),$$

and the ratios of the CC flux to NC and ES respectively are

$$\frac{\phi_{\rm CC}^{\rm uncon}}{\phi_{\rm NC}^{\rm uncon}} = 0.340 \pm 0.023 \ ({\rm stat})^{+0.029}_{-0.031} \ ({\rm syst})$$

$$\frac{\phi_{\rm CC}^{\rm uncon}}{\phi_{\rm ES}^{\rm uncon}} = 0.712 \pm 0.075 \ ({\rm stat})^{+0.045}_{-0.044} \ ({\rm syst}).$$
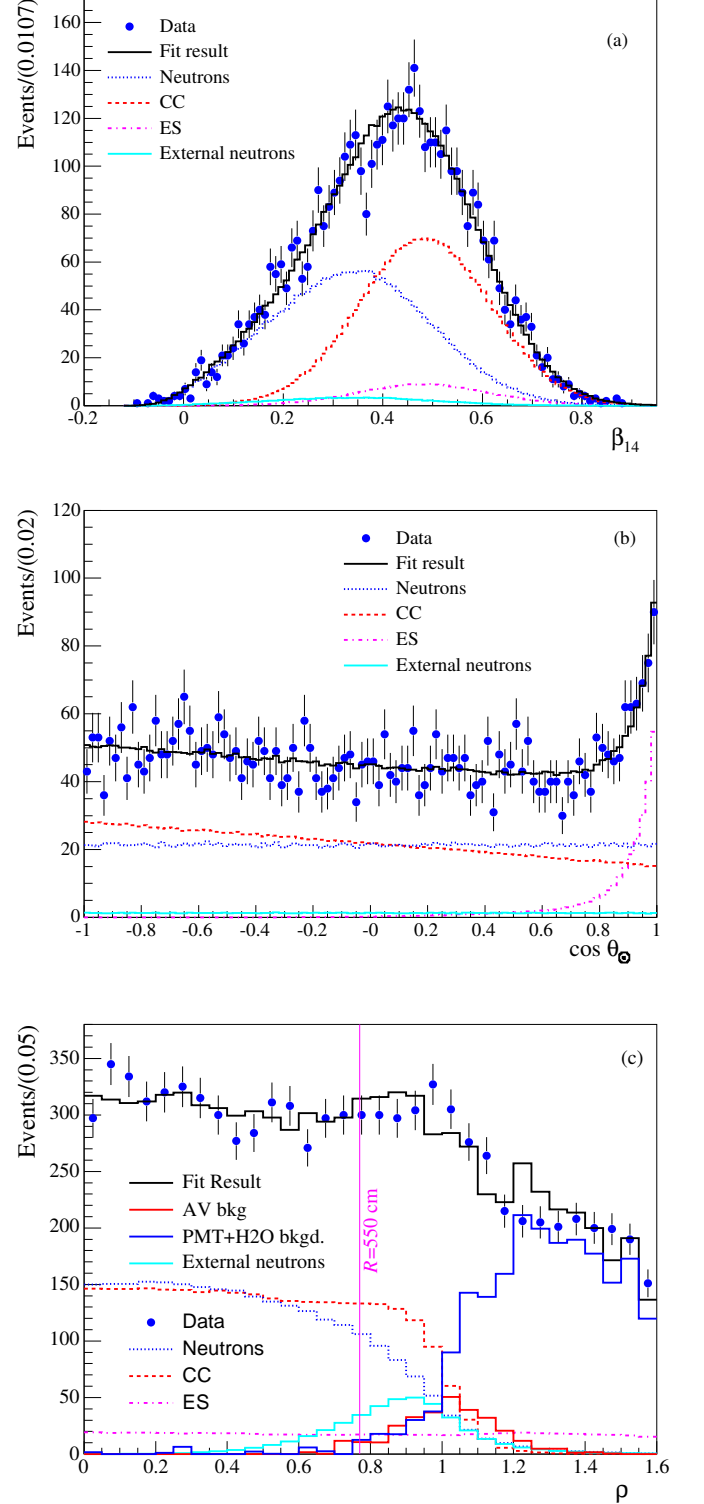


FIG. 28: Distribution of (a) $\beta_{14}$, (b) $\cos\theta_\odot$ and (c) volume-weighted radius $\rho$. Points with error bars represent data while the MC predictions for CC, ES, NC + internal and external-source neutron events, all scaled to the energy-unconstrained fit results, are as indicated in the legend. The dark solid lines represent the summed components. The (a) and (b) distributions are for events with $T_{\rm eff} \geq 5.5$ MeV and $R_{\rm fit} \leq 550$ cm, and are averaged assuming an undistorted $^8$B spectrum. The same energy cut has been applied for (c) but events are shown out to $\rho < 1.6$, where $\rho = 1.0$ is the edge of the heavy water volume. The dashed vertical line represents the 550 cm fiducial volume cut.

TABLE XIX: Systematic uncertainties (%) on fluxes for the energy-unconstrained analysis of the salt data set. Note that "const." denotes an energy-independent systematic component and "E dep" an energy-dependent part.

| Source | NC uncert. (%) | CC uncert. (%) | ES uncert. (%) |
|---|---|---|---|
| Energy scale (const.) | -3.3, +3.8 | -0.9, +1.0 | -1.6, +1.9 |
| Energy scale (E dep.) | -0.1, +0.1 | -0.1, +0.1 | -0.1, +0.1 |
| Energy radial bias | -2.0, +2.1 | -0.6, +0.7 | -1.1, +1.2 |
| Energy resolution | -0.8, +0.8 | -0.2, +0.2 | -0.7, +0.7 |
| $\beta_{14}$ mean (const.) | -3.6, +4.5 | -4.0, +3.7 | -1.2, +1.3 |
| $\beta_{14}$ mean (E dep.) | -0.1, +0.2 | -0.2, +0.0 | -0.0, +0.1 |
| $\beta_{14}$ width | -0.0, +0.0 | -0.2, +0.2 | -0.2, +0.2 |
| Radial scale (const.) | -3.0, +3.3 | -2.6, +2.5 | -2.6, +3.0 |
| Radial scale (E dep.) | -0.6, +0.5 | -0.9, +0.8 | -0.7, +0.8 |
| Vertex $x$ | -0.0, +0.0 | -0.0, +0.0 | -0.1, +0.1 |
| Vertex $y$ | -0.1, +0.0 | -0.0, +0.0 | -0.1, +0.1 |
| Vertex $z$ | -0.2, +0.2 | -0.1, +0.1 | -0.0, +0.0 |
| Vertex resolution | -0.1, +0.1 | -0.1, +0.1 | -0.1, +0.1 |
| Angular resolution | -0.2, +0.2 | -0.4, +0.4 | -5.1, +5.1 |
| Internal neutron bkgd. | -1.9, +1.6 | -0.0, +0.0 | -0.0, +0.0 |
| Internal $\gamma$ bkgd. | -0.1, +0.1 | -0.1, +0.1 | -0.0, +0.0 |
| Internal Cherenkov bkgd. | -0.9, +0.0 | -0.9, +0.0 | -0.0, +0.0 |
| External Cherenkov bkgd. | -0.2, +0.0 | -0.2, +0.0 | -0.0, +0.0 |
| Instrumental bkgd. | -0.4, +0.0 | -0.3, +0.0 | -0.0, +0.0 |
| Neutron capture eff. | -2.3, +2.1 | -0.0, +0.0 | -0.0, +0.0 |
| Total systematic | -6.9, +7.6 | -5.1, +4.7 | -6.2, +6.5 |
| Cross section [45] | ±1.1 | ±1.2 | ±0.5 |
| Total statistical | ±4.2 | ±3.7 | ±9.3 |

TABLE XX: Systematic uncertainties (%) on fluxes for the energy-constrained analysis of the salt data set. Note that "const." denotes an energy-independent systematic component and "E dep" an energy-dependent part.

| Source | NC uncert. (%) | CC uncert. (%) | ES uncert. (%) |
|---|---|---|---|
| Energy scale (const.) | -0.3, +0.7 | -3.7, +3.9 | -1.8, +1.6 |
| Energy scale (E dep.) | -0.9, +1.0 | -1.0, +1.0 | -0.2, +0.2 |
| Energy radial bias | -0.1, +0.1 | -2.5, +2.6 | -1.0, +0.9 |
| Energy resolution | -2.1, +2.1 | -1.1, +1.1 | -0.6, +0.6 |
| $\beta_{14}$ mean (const.) | -2.2, +3.0 | -2.4, +2.0 | -0.5, +2.3 |
| $\beta_{14}$ mean (E dep.) | -0.2, +0.2 | -0.2, +0.2 | -0.7, +0.7 |
| $\beta_{14}$ width | -0.0, +0.0 | -0.1, +0.1 | -0.8, +0.8 |
| Radial scale (const.) | -3.0, +3.3 | -2.7, +2.6 | -1.9, +2.9 |
| Radial scale (E dep.) | -0.2, +0.2 | -1.3, +1.2 | -0.8, +0.8 |
| Vertex $x$ | -0.0, +0.1 | -0.0, +0.0 | -0.1, +0.1 |
| Vertex $y$ | -0.1, +0.0 | -0.0, +0.0 | -0.2, +0.2 |
| Vertex $z$ | -0.1, +0.1 | -0.1, +0.0 | -0.0, +0.0 |
| Vertex resolution | -0.1, +0.1 | -0.2, +0.2 | -0.7, +0.7 |
| Angular resolution | -0.2, +0.2 | -0.4, +0.4 | -4.9, +4.9 |
| Internal neutron bkgd. | -1.9, +1.6 | -0.0, +0.0 | -0.0, +0.0 |
| Internal $\gamma$ bkgd. | -0.2, +0.1 | -0.1, +0.0 | -0.0, +0.1 |
| Internal Cherenkov bkgd. | -0.9, +0.0 | -0.8, +0.0 | -0.0, +0.0 |
| External Cherenkov bkgd. | -0.2, +0.0 | -0.2, +0.0 | -0.0, +0.0 |
| Instrumental bkgd. | -0.4, +0.0 | -0.3, +0.0 | -0.0, +0.0 |
| Neutron capture eff. | -2.3, +2.1 | -0.0, +0.0 | -0.0, +0.0 |
| Total systematic | -5.4, +5.7 | -6.2, +6.0 | -5.9, +6.6 |
| Cross section [45] | ±1.1 | ±1.2 | ±0.5 |
| Total Statistical | ±3.9 | ±3.1 | ±9.8 |

Note that the uncertainties on the ratios are not normally distributed.

The non-$\nu_e$ active neutrino component ($\phi_{\mu\tau}$) of the $^8$B flux can be determined by subtracting the $\phi_e$ component, as measured by the CC flux, from the NC and ES fluxes. Whereas the NC measurement is equally sensitive to all active neutrinos, the ES measurement has reduced sensitivity to non-electron neutrinos in the form $\phi_{ES} = \phi_e + 0.1553\phi_{\mu\tau}$. The resulting $\phi_{\mu\tau}$
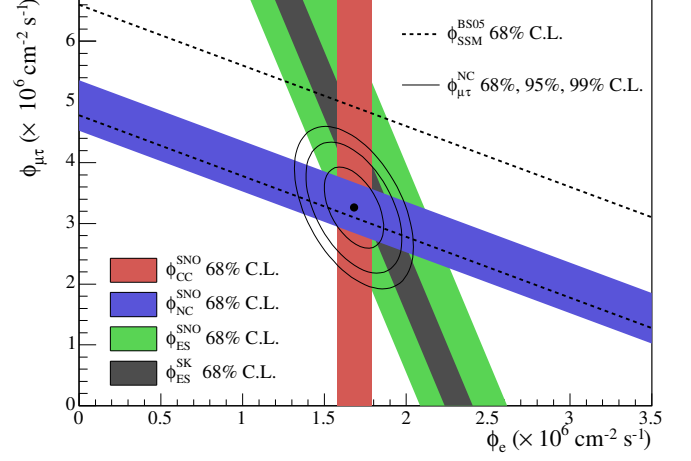


FIG. 29: Flux of $\mu + \tau$ neutrinos versus flux of electron neutrinos. CC, NC and ES flux measurements are indicated by the filled bands. The total $^8$B solar neutrino flux predicted by the Standard Solar Model [13] is shown as dashed lines, and that measured with the NC channel is shown as the solid band parallel to the model prediction. The narrow band parallel to the SNO ES result correponds to the Super-Kamiokande result in [9]. The intercepts of these bands with the axes represent the $\pm 1\sigma$ uncertainties. The non-zero value of $\phi_{\mu\tau}$ provides strong evidence for neutrino flavor transformation. The point represents $\phi_e$ from the CC flux and $\phi_{\mu\tau}$ from the NC-CC difference with 68%, 95%, and 99% C.L. contours included.

fluxes, in units of $10^6$ cm$^{-2}$ s$^{-1}$, are

$$\phi_{\mu\tau}^{\text{NC,uncon}} = 3.26 \pm 0.25 \,(\text{stat}) \,^{+0.40}_{-0.35} \,(\text{syst})$$
$$\phi_{\mu\tau}^{\text{ES,uncon}} = 4.36 \pm 1.52 \,(\text{stat}) \,^{+0.90}_{-0.87} \,(\text{syst}).$$

Figure 29 shows the flux of non-electron flavor active neutrinos ($\phi_{\mu\tau}$) versus the flux of electron neutrinos ($\phi_e$). The error ellipses shown are the 68%, 95% and 99% joint probability contours for $\phi_{\mu\tau}$ and $\phi_e$.

Adding the constraint of an undistorted $^8$B energy spectrum to the signal extraction yields, for comparison with earlier results (in units of $10^6$ cm$^{-2}$s$^{-1}$):

$$\phi_{\text{CC}}^{\text{con}} = 1.72^{+0.05}_{-0.05}(\text{stat})^{+0.11}_{-0.11}(\text{syst})$$
$$\phi_{\text{ES}}^{\text{con}} = 2.34^{+0.23}_{-0.23}(\text{stat})^{+0.15}_{-0.14}(\text{syst})$$
$$\phi_{\text{NC}}^{\text{con}} = 4.81^{+0.19}_{-0.19}(\text{stat})^{+0.28}_{-0.27}(\text{syst}),$$

with corresponding ratios

$$\frac{\phi_{\text{CC}}^{\text{con}}}{\phi_{\text{NC}}^{\text{con}}} = 0.358 \pm 0.021 \,(\text{stat}) \,^{+0.028}_{-0.029} \,(\text{syst})$$
$$\frac{\phi_{\text{CC}}^{\text{con}}}{\phi_{\text{ES}}^{\text{con}}} = 0.736 \pm 0.079 \,(\text{stat}) \,^{+0.050}_{-0.049} \,(\text{syst}),$$

TABLE XXI: Correlation matrix for the constrained fit. External neutrons component is labeled EN.

|    | NC     | CC     | ES     | EN    |
|----|--------|--------|--------|-------|
| NC | 1.000  |        |        |       |
| CC | -0.400 | 1.000  |        |       |
| ES | -0.073 | -0.168 | 1.000  |       |
| EN | -0.472 | -0.039 | -0.012 | 1.000 |

and $\phi_{\mu\tau}$ values, in units of $10^6$ cm$^{-2}$ s$^{-1}$,

$$\phi_{\mu\tau}^{NC,con} = 3.09 \pm 0.22 \text{ (stat)} {}^{+0.30}_{-0.27} \text{ (syst)}$$

$$\phi_{\mu\tau}^{ES,con} = 3.97 \pm 1.56 \text{ (stat)} {}^{+0.92}_{-0.89} \text{ (syst)}.$$

The "energy-constrained" fit is sensitive to somewhat different systematic uncertainties than the unconstrained fit as shown in Table XX. The correlation matrix for the constrained fit, including correlations with the external-neutron component, is given in Table XXI.

Compared to the initial salt phase results [12], some systematic uncertainties have slightly increased. In particular, more detailed analyis of calibration source data during the full salt data set has generated larger systematic uncertainty estimates on mean $\beta_{14}$ and its energy dependence, and on angular resolution. The combined systematic uncertainties for the CC and NC fluxes have not increased. The ES flux systematic uncertainties have increased, but the ES measurement is still dominated by statistical uncertainty which has decreased with the increased statistics. For the $\phi_{CC}/\phi_{NC}$ ratios, however, the effects of $\beta_{14}$ systematic uncertainties are highly anticorrelated, and consequently the $\phi_{CC}/\phi_{NC}$ systematic uncertainties are larger than that reported in [12].

As shown in Fig. 30 and Table XXII, these results are consistent with the pure D$_2$O phase results [3, 4]. Comparisons with the 254-day salt data measured fluxes [12], also given in Table XXII, show some small differences for the unconstrained fit case. The differences are consistent with $\sim 1\sigma$ statistical fluctuations, including covariances, between the 254-day data set of Ref. [12] and the additional 137-day data set included here. Part of the difference may also be attributed to uncorrelated components of the systematic uncertainties between the 254-day and 137-day data sets.

## XII. DAY-NIGHT ASYMMETRIES OF SOLAR NEUTRINO FLUX

For certain ranges of mixing parameters, matter-enhanced neutrino oscillations predict $\nu_e$ regeneration inside the Earth [48–54]. This effect would manifest itself as a day-night asymmetry in the charged current and elastic scattering rates in SNO. For standard neutrino oscillations between active flavors, the neutral current rate should not vary between day and night. An observation of a day-night asymmetry in the neutral
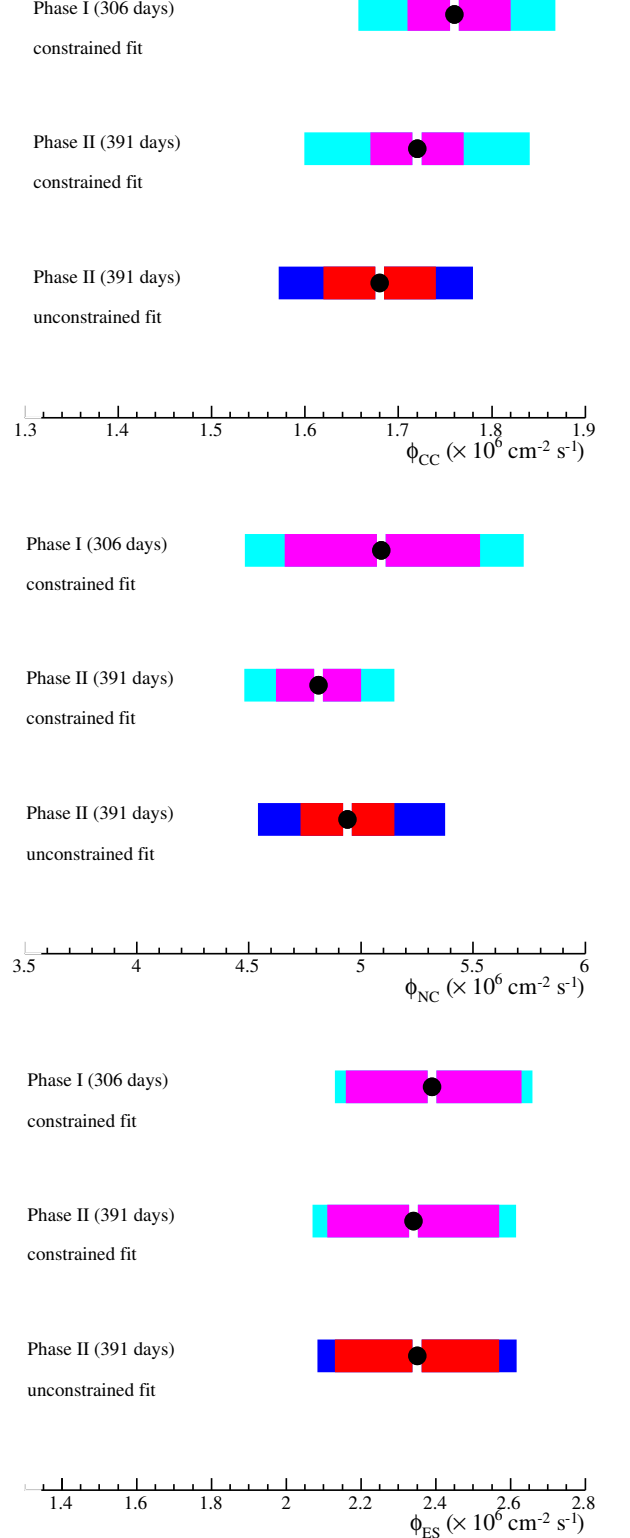


FIG. 30: Comparison of phase I (306 days) and phase II (391 days) flux results. For each case the inner error bar represents the statistical uncertainty while the full error bar represents the combined statistical and systematic uncertainty.

TABLE XXII: Constrained and unconstrained flux results from phase I and phase II SNO data sets in units of $10^6$ cm$^{-2}$s$^{-1}$. Note that the phase I $T_{\rm eff}$ threshold was lower than the phase II threshold.

| Constrained fit | | | |
|---|---|---|---|
| Data Set | $\phi_{\rm CC}^{\rm con}$ | $\phi_{\rm NC}^{\rm con}$ | $\phi_{\rm ES}^{\rm con}$ |
| Phase I (306 days)[4] | $1.76^{+0.06+0.09}_{-0.05-0.09}$ | $5.09^{+0.44+0.46}_{-0.43-0.43}$ | $2.39^{+0.24+0.12}_{-0.23-0.12}$ |
| Phase II (254 days)[12] | $1.70^{+0.07+0.09}_{-0.07-0.10}$ | $4.90^{+0.24+0.29}_{-0.24-0.27}$ | $2.13^{+0.29+0.15}_{-0.28-0.08}$ |
| Phase II (391 days) | $1.72^{+0.05+0.11}_{-0.05-0.11}$ | $4.81^{+0.19+0.28}_{-0.19-0.27}$ | $2.34^{+0.23+0.15}_{-0.23-0.14}$ |
| Unconstrained Fit | | | |
| Data Set | $\phi_{\rm CC}^{\rm uncon}$ | $\phi_{\rm NC}^{\rm uncon}$ | $\phi_{\rm ES}^{\rm uncon}$ |
| Phase I (306 days)[4] | | $6.42^{+1.57+0.55}_{-1.57-0.58}$ | |
| Phase II (254 days)[12] | $1.59^{+0.08+0.06}_{-0.07-0.08}$ | $5.21^{+0.27+0.38}_{-0.27-0.38}$ | $2.21^{+0.31+0.10}_{-0.26-0.10}$ |
| Phase II (391 days) | $1.68^{+0.06+0.08}_{-0.06-0.09}$ | $4.94^{+0.21+0.38}_{-0.21-0.34}$ | $2.35^{+0.22+0.15}_{-0.22-0.15}$ |

TABLE XXIII: Event totals and rates for the day and night data sets.

| | Events | Rate (day$^{-1}$) |
|---|---|---|
| Day | 2134 | $12.09 \pm 0.26$ |
| Night | 2588 | $12.04 \pm 0.24$ |

TABLE XXIV: Day-night integral fluxes and asymmetries from a shape-unconstrained signal extraction. Fluxes are in units of $10^6$ neutrinos cm$^{-2}$ sec$^{-1}$. The systematic uncertainties on the day and night fluxes include large correlated systematics that cancel in the day-night asymmetry ratio $A$.

| Signal | Day flux | Night flux | $A$ |
|---|---|---|---|
| CC | $1.73 \pm 0.09 \pm 0.10$ | $1.64 \pm 0.08 \pm 0.09$ | $-0.056 \pm 0.074 \pm 0.053$ |
| NC | $4.81 \pm 0.31 \pm 0.39$ | $5.02 \pm 0.29 \pm 0.41$ | $0.042 \pm 0.086 \pm 0.072$ |
| ES | $2.17 \pm 0.34 \pm 0.14$ | $2.52 \pm 0.32 \pm 0.16$ | $0.146 \pm 0.198 \pm 0.033$ |

current rate could be evidence for an admixture of sterile neutrinos, or for unexpected matter interactions inside the earth. To search for day-night asymmetries in solar neutrino reaction rates, the day-night asymmetry ratio $A = 2(\phi_N - \phi_D)/(\phi_N + \phi_D)$ is constructed using the day and night fluxes $\phi_D$ and $\phi_N$ for each reaction. The day and night neutrino fluxes at SNO can be measured either allowing for a neutral current day-night asymmetry, or constraining $A_{\rm NC} = 0$ as predicted by standard neutrino oscillations with only active flavors.

SNO's data set was divided into day and night portions, defined by the Sun being above or below the horizon respectively. Separate day and night signal probability distributions were built for CC, ES, and NC events from Monte Carlo simulations that properly included the live time exposure of the data set. The day-night analysis used the same event selection, analysis cuts, and background estimates as the integral flux and energy spectral analyses. Each background was divided between the day and night data sets according to its measured diurnal rate asymmetry. Fits of the signal and background PDFs to the data sets determined the night and day neutrino fluxes for each type of interaction. In addition to day and night live time corrections, the fluxes were corrected for seasonal variations in the neutrino rate due to the eccentricity of the Earth's orbit. The eccentricity corrections were determined from Monte Carlo simulations.

Because most systematics cancel when forming a day-night ratio, the dominant uncertainties on day-night ratios are statistical. To avoid introducing statistical biases into the analysis, the entire data set was divided into a 20% "open" portion and an 80% "closed" portion. The 20% open fraction was sampled uniformly from each run. All analysis cuts and procedures were developed and tested based on measurement of day-night ratios on only the 20% open data set. Then the analysis procedures were frozen, and day-night asymmetries were calculated for the 391-day data set. Day-night results for the 20% open data set and for the full data set are statistically consistent. Only results for the total data set are reported here.

Systematic uncertainties on the day-night asymmetries are described in Sec. VIII. The effects of day-night differences in

detector response have been determined by perturbing the day and night signal PDFs by the detector response uncertainty for each systematic. This perturbation technique is described in Sec. IX. Uncertainties in backgrounds have been propagated by varying the amplitude and the day-night rate asymmetry of each background in the flux fits.

### A. Total Event Rate

The simplest day-night analysis is to compare the total event rates (signals + backgrounds) between day and night. Table XXIII shows these results. The day and night rates are statistically consistent. Because the external neutron background is determined from fits to the data itself, backgrounds cannot be subtracted from the raw event rates without doing a full signal extraction fit.

### B. Model-Independent Day-Night Asymmetries

The most general day-night analysis is to fit for the day and night neutrino fluxes separately, placing no constraint on $A_{\rm NC}$ and making no assumption about the energy dependence of the $\nu_e$ oscillation probability. The results include day and night NC fluxes, and separate day and night CC energy spectra.

Table XXIV presents the day and night integral fluxes from the shape-unconstrained analysis. Each pair of day-night fluxes shares some large common systematics, as calculated for the integral flux analysis in Sec. XI. The day and night fluxes are statistically independent, however. The asymmetry ratio $A$ for each flux includes a statistical uncertainty, and a systematic uncertainty due to day-night specific effects as described in Sec. VIII. All asymmetries are consistent with zero.

Figure 31(a) shows the value of $A_{\rm CC}$ in each energy bin $A_{{\rm CC},i}$. Overlaid is the expectation for the previous best-fit mix-
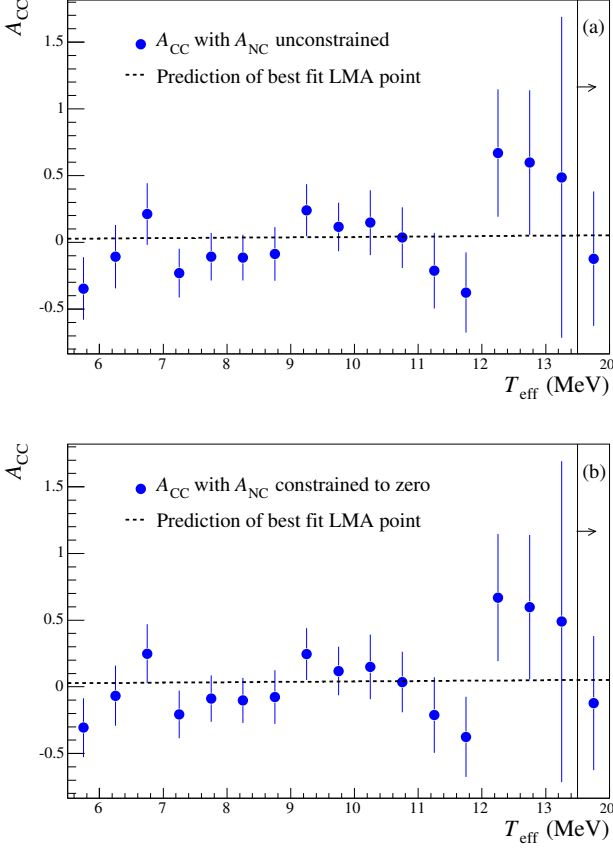
FIG. 31: Day-night asymmetries on each CC energy bin as a function of electron energy. Panel (a) shows the case in which no constraint is made on $A_{NC}$. Panel (b) shows the case in which $A_{NC}$ is constrained to zero. Uncertainties are statistical only. The vertical lines in each figure show the expectation for $\Delta m^2 = 7 \times 10^{-5}$ eV$^2$ and $\tan^2 \theta = 0.40$.

ing parameters $\Delta m^2 = 7 \times 10^{-5}$ eV$^2$ and $\tan^2 \theta = 0.40$ [12]. The dependence of $A_{CC}$ on CC electron energy is consistent with this expectation, but is also consistent with no day-night asymmetries.

Although the day and night fluxes are statistically independent, the CC, ES, and NC fluxes for either day or night are statistically correlated since they are produced from a common fit. As a result, $A_{CC}$, $A_{NC}$, and $A_{ES}$ are statistically correlated, with correlation coefficients given by:

$$\rho(CC, NC) = -0.532$$
$$\rho(CC, ES) = -0.147$$
$$\rho(ES, NC) = -0.064.$$

Similarly, the $A_{CC,i}$ are modestly correlated between different energy bins at lower energies due to their common covariance with $A_{NC}$. Figure 32 is a contour plot of $A_{NC}$ versus $A_{CC}$, illustrating the covariances.

Table XXV lists each systematic uncertainty on the integral flux asymmetries from the shape-unconstrained day-night analysis. The largest systematics are uncertainties on diurnal
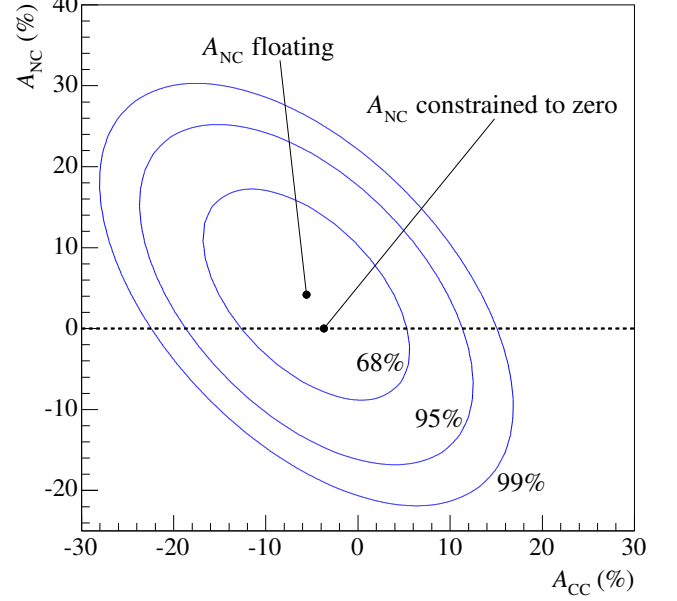


FIG. 32: Joint probability contours for $A_{NC}$ versus $A_{CC}$ (as %), statistical uncertainties only. The points indicate the results when $A_{NC}$ is allowed to float and when it is constrained to zero.

TABLE XXV: Systematic uncertainties on day-night asymmetries for the shape-unconstrained signal extraction. For presentation, uncertainties have been symmetrized and rounded.

| Systematic | $A_{CC}$ uncert. | $A_{NC}$ uncert. | $A_{ES}$ uncert. |
|---|---|---|---|
| Diurnal energy scale | 0.004 | 0.015 | 0.007 |
| Directional energy scale | 0.001 | 0.000 | 0.014 |
| Long-term energy scale variation | 0.002 | 0.010 | 0.001 |
| Diurnal energy resolution | 0.003 | 0.006 | 0.004 |
| Directional energy resolution | 0.001 | 0.001 | 0.003 |
| Diurnal vertex shift | 0.008 | 0.012 | 0.007 |
| Directional vertex shift | 0.000 | 0.000 | 0.003 |
| Diurnal vertex resolution | 0.002 | 0.006 | 0.002 |
| Directional vertex resolution | 0.000 | 0.000 | 0.001 |
| Diurnal isotropy | 0.050 | 0.064 | 0.017 |
| Directional isotropy | 0.002 | 0.002 | 0.004 |
| Long-term isotropy variation | 0.014 | 0.015 | 0.006 |
| Directional angular resolution | 0.001 | 0.001 | 0.020 |
| Live time | 0.000 | 0.000 | 0.000 |
| Cut acceptance | 0.003 | 0.004 | 0.003 |
| External Cherenkov tail bkgd. amplitude | 0.002 | 0.003 | 0.000 |
| External Cherenkov tail bkgd. asymmetry | 0.003 | 0.004 | 0.000 |
| Internal Cherenkov tail bkgd. amplitude | 0.001 | 0.000 | 0.000 |
| Internal Cherenkov tail bkgd. asymmetry | 0.001 | 0.001 | 0.000 |
| Internal neutron bkgd. amplitude | 0.000 | 0.003 | 0.000 |
| Internal neutron bkgd. asymmetry | 0.000 | 0.015 | 0.000 |
| Internal $\gamma$ bkgd. amplitude | 0.000 | 0.000 | 0.000 |
| Internal $\gamma$ bkgd. asymmetry | 0.000 | 0.000 | 0.000 |
| Isotropic AV bkgd. amplitude | 0.001 | 0.001 | 0.000 |
| Isotropic AV bkgd. asymmetry | 0.002 | 0.002 | 0.000 |
| Instrumental bkgd. amplitude | 0.000 | 0.001 | 0.000 |
| Instrumental bkgd. asymmetry | 0.001 | 0.002 | 0.000 |
| Total | 0.053 | 0.072 | 0.033 |

TABLE XXVI: Day-night integral fluxes from a shape-unconstrained signal extraction, with the constraint $A_{NC} \equiv 0$. Fluxes are in units of $10^6$ neutrinos cm$^{-2}$ sec$^{-1}$.

| Signal | Day flux | Night flux | Asymmetry |
|--------|----------|------------|-----------|
| CC | $1.71 \pm 0.08 \pm 0.09$ | $1.65 \pm 0.08 \pm 0.09$ | $-0.037 \pm 0.063 \pm 0.032$ |
| ES | $2.18 \pm 0.34 \pm 0.14$ | $2.53 \pm 0.32 \pm 0.16$ | $0.153 \pm 0.198 \pm 0.030$ |
| NC | | $4.93 \pm 0.21 \pm 0.36$ | $A_{NC} \equiv 0$ |

variations of the isotropy parameter $\beta_{14}$, and diurnal variations in energy scale and vertex shift. For the ES rate, directional systematics are significant. However, the overall uncertainties on all asymmetries are ultimately limited by statistics.

### C. Shape-Constrained Day-Night Asymmetries

A variant of the preceding analysis is to constrain the day and night $\nu_e$ energy spectra to follow an undistorted $^8$B shape. This corresponds to an energy-independent oscillation probability that varies between night and day. The NC rate was again allowed to vary in the fit. It should be noted that standard neutrino oscillations with mixing parameters in the LMA region do not predict energy-independent day-night asymmetries. The derived asymmetries under the assumption that the CC and ES energy spectra are undistorted, but allowing them to have different normalizations between night and day, are

$$A_{CC} = -0.021 \pm 0.063 \pm 0.035$$
$$A_{NC} = 0.018 \pm 0.079 \pm 0.052$$
$$A_{ES} = 0.066 \pm 0.198 \pm 0.057. \quad (17)$$

### D. Day-Night Asymmetries with the Constraint $A_{NC} \equiv 0$

In the previous two subsections the NC flux was allowed to vary in the fit between the day and night data sets. Under the standard picture of matter-enhanced neutrino oscillations, $A_{NC}$ should be zero. This prediction has been confirmed by the results of the previous two subsections. When determining the best estimate of the day-night asymmetry on the electron neutrino flux, *assuming standard neutrino oscillations*, it is appropriate to constrain $A_{NC}$. This constraint has been applied by simultaneously fitting the day and night data sets, not allowing $\phi_{NC}$ to vary between night and day.

The additional constraint of $A_{NC} \equiv 0$ reduces the statistical uncertainties on $A_{CC}$ and $A_{ES}$. It also produces a modest covariance between the day and night fluxes, due to their common covariance with $\phi_{NC}$. In contrast, without a constraint on $A_{NC}$ the day and night neutrino fits are statistically independent.

The day and night neutrino fluxes were fit in a shape-unconstrained analysis, requiring $A_{NC} \equiv 0$. Table XXVI gives the day and night integral fluxes from this fit, and the NC flux. No statistically significant asymmetries are observed. Forcing $A_{NC} \equiv 0$ results in some reduction in $|A_{CC}|$, as expected from
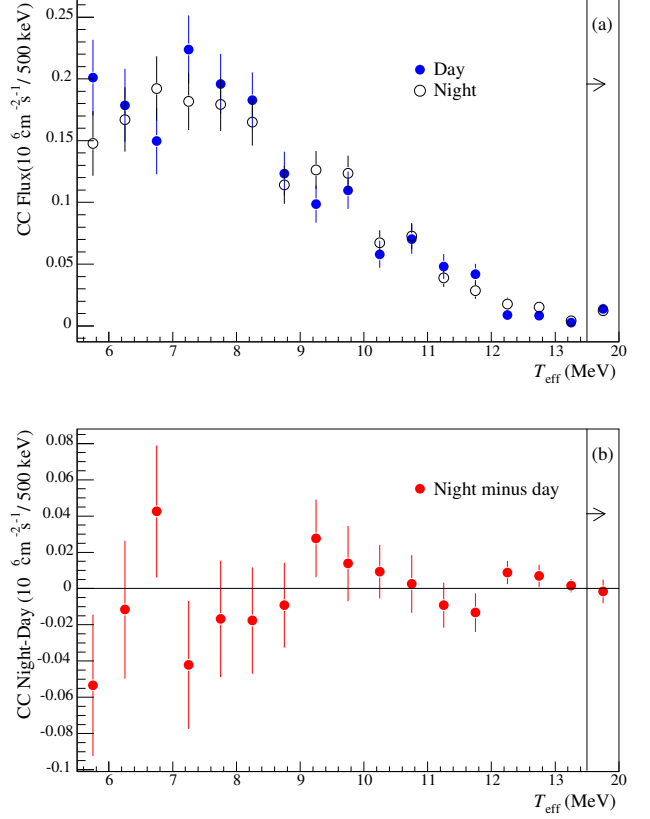


FIG. 33: (a) Day and night extracted CC energy spectra with statistical uncertainties only. Bin values are expressed in units of equivalent $^8$B flux, normalized such that the sum of the flux bin values above 5.5 MeV equals the total integral $^8$B neutrino flux above 0 MeV, as determined for the day and night integral fluxes quoted in section XII(D) (see Appendix A). (b) Difference *night - day* between the spectra. In both figures, the final bin extends to 20 MeV.

the anti-correlation of CC and NC event totals in the signal extraction.

Figures 31(b) and 33 show the CC asymmetry as a function of electron energy and the day and night CC energy spectra, binned by electron energies. The additional constraint does not significantly change the results. Table XXVII presents the systematic uncertainties on $A_{CC}$ and $A_{ES}$ for this analysis.

### E. Shape-Constrained Day-Night Asymmetries with the Constraint $A_{NC} \equiv 0$

For the sake of completeness the analysis of Sec. XII C has been repeated with the additional constraint that $A_{NC} \equiv 0$. The results are

$$A_{CC} = -0.015 \pm 0.058 \pm 0.027$$
$$A_{ES} = 0.070 \pm 0.197 \pm 0.054. \quad (18)$$

TABLE XXVII: Systematic uncertainties on day-night asymmetries for the shape-unconstrained signal extraction, with the constraint $A_{NC} \equiv 0$. For presentation, uncertainties have been symmetrized and rounded.

| Systematic | $A_{CC}$ uncert. | $A_{ES}$ uncert. |
|---|---|---|
| Diurnal energy scale | 0.009 | 0.009 |
| Directional energy scale | 0.001 | 0.014 |
| Long-term energy scale variation | 0.006 | 0.002 |
| Diurnal energy resolution | 0.002 | 0.004 |
| Directional energy resolution | 0.001 | 0.002 |
| Diurnal vertex shift | 0.013 | 0.009 |
| Directional vertex shift | 0.000 | 0.003 |
| Diurnal vertex resolution | 0.001 | 0.002 |
| Directional vertex resolution | 0.000 | 0.001 |
| Diurnal isotropy | 0.022 | 0.009 |
| Directional isotropy | 0.001 | 0.005 |
| Long-term isotropy variation | 0.013 | 0.003 |
| Directional angular resolution | 0.002 | 0.019 |
| Live time | 0.000 | 0.000 |
| Cut acceptance | 0.003 | 0.003 |
| External Cherenkov tail bkgd. amplitude | 0.002 | 0.000 |
| External Cherenkov tail bkgd. asymmetry | 0.003 | 0.000 |
| Internal Cherenkov tail bkgd. amplitude | 0.001 | 0.000 |
| Internal Cherenkov tail bkgd. asymmetry | 0.001 | 0.000 |
| Internal neutron bkgd. amplitude | 0.002 | 0.001 |
| Internal neutron bkgd. asymmetry | 0.007 | 0.002 |
| Internal $\gamma$ bkgd. amplitude | 0.000 | 0.000 |
| Internal $\gamma$ bkgd. asymmetry | 0.000 | 0.000 |
| Isotropic AV bkgd. amplitude | 0.001 | 0.000 |
| Isotropic AV bkgd. asymmetry | 0.002 | 0.000 |
| Instrumental bkgd. amplitude | 0.001 | 0.000 |
| Instrumental bkgd. asymmetry | 0.001 | 0.000 |
| Total | 0.032 | 0.030 |

## F. Combined Day-Night Asymmetries from the Salt and $D_2O$ Data Sets

During the first phase of the SNO experiment, the asymmetry on the electron neutrino flux was measured to be $A_e = 0.070 \pm 0.049^{+0.013}_{-0.012}$, assuming a standard $^8$B shape and constraining $A_{NC} = 0$. Although an asymmetry ratio formed from two normally-distributed variables is not necessarily normally distributed, for the case of SNO's day and night fluxes a normal distribution is an excellent approximation for the true distribution we calculate for $A_{CC}$ or $A_e$. The asymmetry results from SNO's first phase are statistically independent of the results from the salt data set and statistical uncertainties dominate over systematics for the asymmetries. Hence, combining values and uncertainties for $A_{CC}$ from Sec. XII E and $A_e$ from above can be done trivially to produce a combined, albeit model-dependent, day-night asymmetry of $A_{e,combined} = 0.037 \pm 0.040$. A future SNO analysis will address the issue of doing a joint shape-unconstrained fit to the $D_2O$ and salt data sets.

The Super-Kamiokande collaboration has measured the day-night rate asymmetry of ES interactions above 5 MeV to be $A_{ES} = 0.021 \pm 0.020^{+0.012}_{-0.013}$ [55]. Because ES interactions can be initiated by either $\nu_e$ or $\nu_{\mu\tau}$, the day-night asymmetry for ES events is diluted by a factor of $(\phi_e + 0.1576(\phi_{tot} - \phi_e))/((1 - 0.1576)\phi_e) = 1.55$. Assuming an energy-independent conversion mechanism and only active neutrinos, the Super-Kamiokande result scales to a $\phi_e$ asymmetry of $A_{e,SK} = 0.033 \pm 0.031^{+0.019}_{-0.020}$. Combining the SNO

$D_2O$ and SNO salt values for $A_e$ with the equivalent Super-Kamiokande value $A_{e,SK}$ gives $A_{e,combined} = 0.035 \pm 0.027$. This result explicitly assumes a shape-constrained $^8$B spectrum for SNO and ignores energy dependence of the oscillation probability over the energy range in question.

## XIII. MSW INTERPRETATION OF RESULTS

The observation of a substantially suppressed $\nu_e$ flux with the CC reaction in SNO compared to the total active flux measured by the NC reaction in SNO provides clear evidence for neutrino flavor change that can be analyzed in terms of neutrino oscillations. Constraints on neutrino mixing parameters can be derived by comparing neutrino oscillation model predictions with experimental data, as has been done in, for example, [53, 56–60] and in previous SNO analyses [5, 12].

A two-flavor, active neutrino oscillation model has two parameters: $\Delta m^2$, the difference between the square of the masses of the relevant eigenstates of propagation for the neutrinos, and $\tan^2 \theta$ that quantifies the strength of the mixing between flavor and mass eigenstates. Note that the three-flavor mixing matrix element $U_{e2}$ can be written as $\cos \theta_{13} \sin \theta_{12}$ [15], which is approximately equal to $\sin \theta$ for two-flavor solar neutrino oscillations when $\theta_{13}$ is small and when $\Delta m^2_{sol} \ll \Delta m^2_{atm}$. The MSW effect [16] can result in neutrinos above a few MeV emerging from the Sun essentially as a pure $\nu_2$ state (e.g. for oscillation parameters in the Large Mixing Angle region). To the degree to which this statement is true, SNO's $\phi_{CC}/\phi_{NC}$ ratio, a direct measure of the $\nu_e$ survival probability, is also a direct measure of $|U_{e2}|^2$ and thus should be approximately equal to $\sin^2 \theta$. For the sake of comparison with other past and present oscillation analyses, this present work still employs $\tan^2 \theta$ to quantify the mixing angle for solar neutrino oscillations.

For each pair of parameters, the oscillation model predicts the expected rates in the Cl [6] and Ga experiments [7, 8], Super-Kamiokande zenith spectra [9], and SNO rates and spectra. The model prediction accounts for MSW propagation of neutrino states through dense matter in the Sun and the Earth and so allows for the regeneration of $\nu_e$ flavor for neutrinos passing through the Earth at night. A global $\chi^2$ calculation can be performed; best-fit parameters can be determined and allowed parameter regions can be identified using $\Delta\chi^2$ confidence levels for two degrees of freedom. The same neutrino oscillation model can also predict rates and spectra for the KamLAND experiment [17, 61], assuming CPT invariance (since KamLAND detects $\bar{\nu}_e$). The likelihood values from a KamLAND oscillation analysis can be easily combined with that from the global solar neutrino analysis to further restrict the allowed oscillation parameter space.

For the analysis presented in this paper, earlier data from SNO-I (pure $D_2O$ phase) have been included. SNO-I day and night spectra have been interpreted in a similar manner as before [5, 12, 62]. Summed spectra (CC+ES+NC+background) predictions were compared to the number of counts in each spectral bin from the SNO-I data, for both day and night. A minor improvement in the analysis of this earlier data is that

this part of the calculation now includes energy-dependent $\nu$-$d$ radiative corrections for the CC reaction. Previously the CC radiative correction was included as an energy-independent factor.

In [12], salt phase "fluxes" (i.e., CC, NC and ES fluxes inferred from rates) were added to the global $\chi^2$ analysis. The present work has a new oscillation analysis using data from the 391-day data set of the salt phase which have been analyzed and extracted as CC spectra and NC and ES integrated fluxes, separately for day and night. This information is included in the global $\chi^2$ analysis in lieu of just salt phase fluxes inferred from rates. This allows CC spectral shape information and day-night rate asymmetry information from the salt phase to be included in the global oscillation analysis. CC-NC separation is preserved in this analysis since the SNO unconstrained signal extraction utilized information from event isotropy $\beta_{14}$ and angular correlation $\cos\theta_\odot$ distributions for separating the salt NC and ES fluxes from the CC spectra.

SNO's unconstrained signal extraction produced two 19×19 statistical covariance matrices (one for day and one for night) for 17 spectral bins of the CC spectrum, starting from 5.5 MeV kinetic energy up to 13.5 MeV, in 0.5 MeV steps, with one extra bin integrating from 13.5–20.0 MeV, plus the NC and ES fluxes. These statistical covariance matrices are required in the calculation of $\chi^2$ and are available in Appendix A. Day and night data are statistically independent from each other and the results with no constraint on $A_{NC}$ were used.

Systematic uncertainties also have bin-to-bin correlations and unlike the statistical correlations from SNO's signal extraction may also include correlations that extend across day and night spectra. Experimental spectral shape systematic uncertainties were described in Section X and were included in this oscillation analysis. The uncertainty in the shape of the $^8$B neutrino spectrum has also been included in this $\chi^2$ analysis. The $^8$B spectrum used in our model is the one from [38]; however, the more generous uncertainties from [63] were employed in the systematics calculation in our $\chi^2$ analysis.

Day-night systematics, though small, were also included in the global $\chi^2$ analysis. The significant day-night systematics are diurnal energy scale, long-term energy scale variation, diurnal vertex shift, diurnal isotropy variation, long-term isotropy variation, and internal neutron background asymmetry. Other day-night systematics discussed in this paper are smaller in magnitude and were averaged together in the $\chi^2$ calculation. Note that some directional systematics have a non-negligible effect on the day-night asymmetry of ES events; however, the impact of the day-night asymmetry of ES events in SNO on the oscillation analysis is not that significant so combining these systematics is also reasonable. The technique for including systematic uncertainties and bin-to-bin correlations in the $\chi^2$ analysis is the conventional one, as in [64]. Thus $\chi^2_{SNO-II}$ from SNO's 391-day data set is defined as:

$$\chi^2_{SNO-II} = \sum_{i,j=1}^{38} (Y_i^{data} - Y_i^{model})[\sigma^2_{ij}(tot)]^{-1}(Y_j^{data} - Y_j^{model}), \quad (19)$$

where $Y_i^{data}$ is the SNO experimental value in one of the 17 CC spectral bins, or the NC or ES flux, day or night, and $Y_i^{model}$ is

the model predicted value for bin $i$ based on the neutrino oscillation hypothesis and the set of parameters being evaluated.

The error matrix for the calculation $\sigma^2_{ij}(tot)$, is composed of statistical and systematic components:

$$\sigma^2_{ij}(tot) = \sigma^2_{ij}(stat) + \sigma^2_{ij}(syst), \quad (20)$$

with $\sigma^2_{ij}(stat)$ containing the elements from the statistical covariance matrices from SNO's unconstrained signal extraction and $\sigma^2_{ij}(syst)$ containing contributions from systematic uncertainties. The spectral systematics error matrix is formed from the partial derivatives that relate the rate $Y^{model}$ in the $i$th bin to the uncertainty in each one of the $K$ spectral systematics $S_k$:

$$\sigma^2_{ij}(syst) = \sum_{k=1}^{K} \frac{\partial Y_i}{\partial S_k} \frac{\partial Y_j}{\partial S_k} (\Delta S_k)^2, \quad (21)$$

where $\Delta S_k$ is the uncertainty estimated for spectral systematic $S_k$. Note that all systematic uncertainties have an effect on the extracted CC spectra, and possibly an energy-dependent effect; thus, all systematics are spectral systematics. In this standard $\chi^2$ treatment, bin-to-bin correlations are included for the systematics; however, possible correlations among the various systematic uncertainties were neglected.
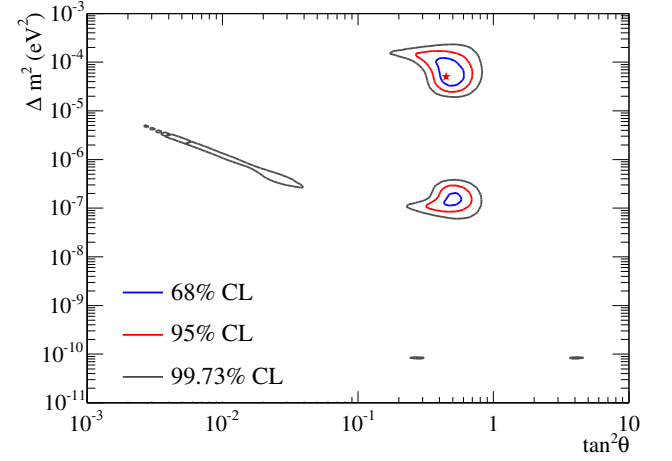


FIG. 34: SNO-only neutrino oscillation analysis, including pure D$_2$O phase day and night spectra, and salt extracted CC spectra, NC and ES fluxes, day and night. The $^8$B flux was free in the fit; *hep* solar neutrinos were fixed at $9.3 \times 10^3$ cm$^{-2}$ s$^{-1}$. The star is plotted at the best-fit parameters from the $\chi^2$ analysis, listed in Table XXVIII.

Figure 34 shows the allowed regions for neutrino oscillation parameters when only SNO data (SNO-I and SNO-II) are analyzed. The inclusion of CC spectral data, improved measurement of the NC flux from the larger data set, and the addition of separate day and night results compared with [12] produce slightly smaller allowed ranges of parameters. The best-fit parameters from a SNO-only analysis are: $\Delta m^2 = 5.0 \times 10^{-5}$ eV$^2$, $\tan^2\theta = 0.45$, $f_B = 5.11 \times 10^6$ cm$^{-2}$ s$^{-1}$, which is the total active $^8$B solar neutrino flux, a free parameter during $\chi^2$ minimization. The best-fit $\chi^2$ is 68.9 for 69 degrees of freedom in the SNO-only oscillation analysis.

but this shift is perfectly consistent with the global solar neutrino constraints and gives a $\chi^2 = 113.6$ for the solar neutrino part of the calculation. A summary of the best-fit oscillation parameters and their ranges within the allowed LMA regions appears in Table XXVIII. SNO data are providing strong constraints on the mixing angle.

TABLE XXVIII: Best-fit neutrino oscillation parameters. Uncertainties listed are $\pm 1\sigma$ for the 2-D parameter regions (and only within the LMA region for the SNO-only analysis).

| Oscillation analysis | $\Delta m^2$ ($10^{-5}$ eV$^2$) | $\tan^2 \theta$ |
|---|---|---|
| SNO-only | $5.0^{+6.2}_{-1.8}$ | $0.45^{+0.11}_{-0.10}$ |
| Global solar | $6.5^{+4.4}_{-2.3}$ | $0.45^{+0.09}_{-0.08}$ |
| Solar plus KamLAND | $8.0^{+0.6}_{-0.4}$ | $0.45^{+0.09}_{-0.07}$ |

Compared to [12] the inclusion of the 391-day salt data set (with spectral and day-night information) in the oscillation analysis moves the allowed oscillation region to slightly larger mixing angles. This is due to the larger central value of the $\phi_{CC}/\phi_{NC}$ ratio found in the present analysis. The 2004 KamLAND data [61] have already tightly constrained the parameter $\Delta m^2$. In terms of individual uncertainties the results become $\Delta m^2 = 8.0^{+0.4}_{-0.3} \times 10^{-5}$ eV$^2$ and $\theta = 33.9^{+1.6}_{-1.6}$ degrees, where the uncertainties were obtained as 1-dimensional projections of the respective parameter while marginalizing the uncertainties in the other.

TABLE XXIX: Comparison of SNO total active $^8$B solar neutrino flux measurements and solar model predictions.

| Source | Total $^8$B Flux ($10^6$ cm$^{-2}$ s$^{-1}$) |
|---|---|
| SNO pure D$_2$O phase NC | $5.09^{+0.44}_{-0.43}$(stat.)$^{+0.46}_{-0.43}$(syst.) |
| above, energy unconstrained | $6.42 \pm 1.57$(stat.)$^{+0.55}_{-0.58}$(syst.) |
| SNO salt phase NC | $4.94 \pm 0.21$(stat.)$^{+0.34}_{-0.38}$(syst.) |
| SNO salt day NC | $4.81 \pm 0.31$(stat.) $\pm 0.39$(syst.) |
| SNO salt night NC | $5.02 \pm 0.29$(stat.) $\pm 0.41$(syst.) |
| SNO-only oscillation fit | 5.11 |
| global solar fit | 5.06 |
| solar plus KamLAND fit | 4.93 |
| BS05(OP) [13] | $5.69 \pm 0.91$ |
| BS05(AGS,OP) [13] | $4.51 \pm 0.72$ |
| BP04 [11] | $5.79 \pm 1.33$ |
| BP2000 [10] | $5.05^{+1.01}_{-0.81}$ |
| TC04 tac A [14] | 4.25 |
| TC04 seismic [14] | $5.31 \pm 0.6$ |

The total active $^8$B solar neutrino flux, measured by the NC reaction, has been presented in several ways in SNO analyses. Table XXIX lists SNO measured (or fit) values and fluxes predicted by solar models. In the first row, the SNO NC flux was extracted assuming an undistorted $^8$B spectrum (for the null hypothesis test). All subsequent values in the table are free from that assumption. The salt phase NC value (this work) is the most precise and appropriate one to compare with solar models. The agreement between solar models and this measurement is good.

Based on the best-fit parameters from the global solar plus KamLAND analysis, the predicted CC electron energy spectrum is determined. In Fig. 36, this prediction is compared



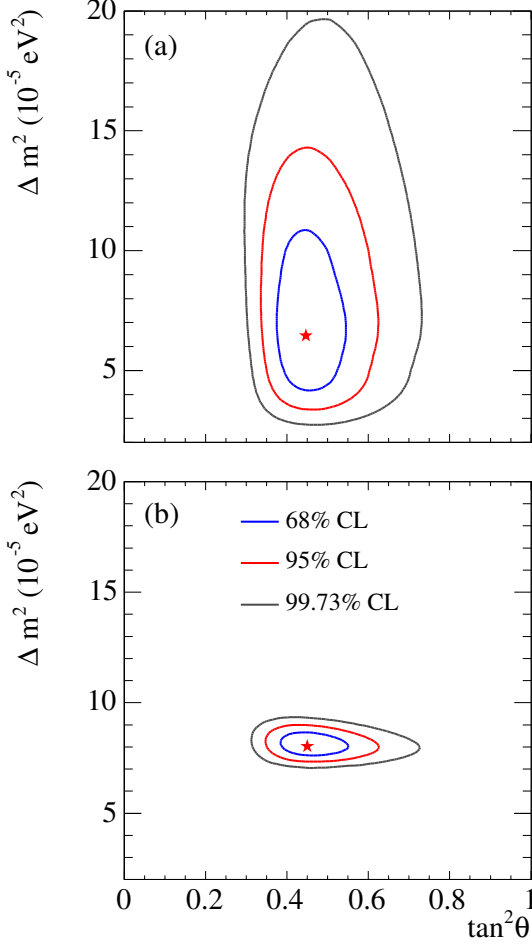FIG. 35: (a) Global neutrino oscillation analysis using only solar neutrino data, and (b) including KamLAND 766 ton-year data. The solar neutrino data included SNO's pure D$_2$O phase day and night spectra, SNO's salt phase extracted day and night CC spectra and ES and NC fluxes, the rate measurements from the Cl, SAGE, Gallex/GNO, and SK-I zenith spectra. The $^8$B flux was free in the fit; *hep* solar neutrinos were fixed at $9.3 \times 10^3$ cm$^{-2}$ s$^{-1}$. The stars are plotted at the best-fit parameters from the $\chi^2$ analysis, listed in Table XXVIII.

The top panel in Fig. 35 shows the allowed region for a global oscillation analysis that included data from all solar neutrino experiments. The best-fit oscillation parameters, with $1\sigma$ uncertainties on the 2-dimensional parameter region given, are $\Delta m^2 = 6.5^{+4.4}_{-2.3} \times 10^{-5}$ eV$^2$, $\tan^2 \theta = 0.45^{+0.09}_{-0.08}$, with a best-fit $\chi^2 = 113.1$ for 116 degrees of freedom in the global solar $\chi^2$ analysis. The lower panel shows the results of the analysis when the 766 ton-year data from KamLAND [61] were also included. The best-fit parameters from the global solar plus KamLAND analysis are: $\Delta m^2 = 8.0^{+0.6}_{-0.4} \times 10^{-5}$ eV$^2$, $\theta = 33.9^{+2.4}_{-2.2}$ degrees, $f_B = 4.93 \times 10^6$ cm$^{-2}$ s$^{-1}$, where the $1\sigma$ uncertainties on the 2-dimensional parameter region are given. The inclusion of KamLAND data shifts the best-fit $\Delta m^2$ value

to the measured CC spectrum. The $\chi^2$ between the extracted spectrum and the expected shape for the best-fit LMA parameters, calculated with all statistical correlations and systematic uncertainties as described above for the global oscillation analysis, is 27.2 for 16 degrees of freedom (17 spectral bins minus a floating normalization factor). The probability of observing a $\chi^2 > 27.2$ under the assumption that the data are drawn from the expected LMA spectrum is 3.9%.
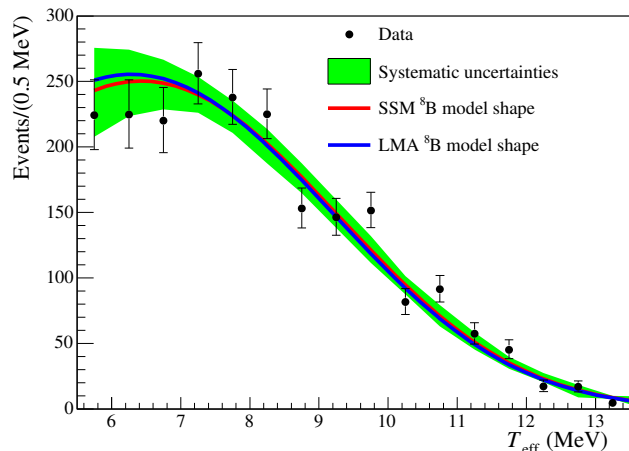


FIG. 36: Extracted CC $T_{\text{eff}}$ spectrum compared to that predicted with the best-fit LMA parameters. Only statistical uncertainties are shown in the data spectrum. The band on the undistorted $^8$B model shape represents the $1\sigma$ uncertainty determined from detector systematic uncertainties. The predicted spectrum is normalized to the same number of counts as the data spectrum. Note that the data points, especially the first three points, are statistically correlated as well as having correlated systematics as indicated by the error band.

## XIV. SUMMARY

An extensive analysis of the data from the full running period with salt added to the heavy water in SNO has been pre-sented. The salt additive enables a statistical separation of NC events from CC and ES events by measuring event isotropy. In addition to new results for integral fluxes, energy spectral information from the CC reaction is presented, with complete statistical and systematic uncertainties. Separate day and night spectra and day-night integrated-flux asymmetries are also presented. The flux measurements are in agreement with, and slightly more precise than, previous measurements [12]. The energy spectrum derived from the CC reaction is consistent with the expected spectrum assuming an undistorted $^8$B shape and also with the predicted spectrum corresponding to the best-fit LMA parameters for a global oscillation analysis with solar neutrino and KamLAND reactor neutrino data included. Within uncertainties, no significant day-night asymmetries are observed as expected for the best-fit LMA solution. Detailed MSW fits find a single allowed region in oscillation parameter space and tightly constrained values for $\Delta m^2$ and the mixing angle $\theta$. These data provide further confirmation of flavor change for solar neutrinos and for the oscillation of massive neutrinos as the dominant flavor change mechanism. The total flux of all active neutrino types for $^8$B solar neutrinos is in agreement with the most recent solar model calculations [13, 14].

[a] Present Address: US Department of Energy, Germantown, MD
[b] Present address: Stanford Linear Accelerator Center, Menlo Park, CA
[c] Present address: Department of Physics, University of California, Irvine, CA
[d] Present address: Department of Physics, Osaka University, Osaka, Japan
[e] Present Address: Department of Physics and Astronomy, Indiana University, South Bend, IN
[f] Present address: Laboratório de Instrumentação e Física Experimental de Partículas, Lisboa, Portugal
[g] Present address: Fermilab, Batavia, IL
[h] Present address: Department of Physics, University of California at San Diego, La Jolla, CA

[i] Present address: Lawrence Livermore National Laboratory, Livermore, CA
[j] Present address: Pacific Northwest National Laboratory, Richland, WA
[k] Present address: Department of Physics, McMaster University, Hamilton, ON
[l] Present address: Lund University, Sweden
[m] Present address: Department of Physics, University of Chicago, Chicago, IL
[n] Present Address: René J.A. Lévesque Laboratory, Université de Montréal, Montreal, PQ
[o] Present Address: TRIUMF, 4004 Wesbrook Mall, Vancouver, BC V6T 2A3, Canada
[p] Present Address: Kamioka Observatory, Institute for Cosmic

Ray Research, University of Tokyo, Kamioka, Gifu, 506-1205, Japan

q  Additional Address: Imperial College, London SW7 2AZ, UK

r  Present address: Department of Physics and Astronomy, University of Sussex, Brighton BN1 9QH, UK

[1] SNO Collaboration, Nucl. Instr. and Meth. **A449**, 172 (2000).

[2] In Ref. [1], the proposal of adding $MgCl_2$, instead of NaCl, to the $D_2O$ target to enhance the neutrino detection efficiency is discussed.

[3] SNO Collaboration, Phys. Rev. Lett. **87**, 071301 (2001).

[4] SNO Collaboration, Phys. Rev. Lett. **89**, 011301 (2002).

[5] SNO Collaboration, Phys. Rev. Lett. **89**, 011302 (2002).

[6] B. Cleveland *et al.*, Astrophys. J. **496**, 505(1998).

[7] V. Gavrin, *Results from the Russian American Gallium Experiment (SAGE)*, VIIIth International Conference on Topics in Astroparticle and Underground Physics (TAUP 2003), Seattle, September 5–9, 2003; J.N. Abdurashitov *et al.*, J. Exp. Theor. Phys. **95**, 181 (2002); the latest SAGE results were presented by C. Cattadori, *Results from Radiochemical Solar Neutrino Experiments*, XXIst International Conference on Neutrino Physics and Astrophysics (Neutrino 2004), Paris, June 14–19, 2004.

[8] E. Bellotti, *The Gallium Neutrino Observatory (GNO)*, VIIIth International Conference on Topics in Astroparticle and Underground Physics (TAUP 2003), Seattle, September 5–9, 2003; M. Altmann *et al.*, Phys. Lett. B **490**, 16 (2000); W. Hampel *et al.*, Phys. Lett. B **447**, 127 (1999).

[9] S. Fukuda *et al.*, Phys. Lett. **B539**, 179 (2002).

[10] J. N. Bahcall, M. Pinsonneault, and S. Basu, Astrophys. J. **555**, 990 (2001).

[11] J. N. Bahcall and M. H. Pinsonneault , Phys. Rev. Lett. **92**, 121301 (2004).

[12] SNO Collaboration, Phys. Rev. Lett. **92**, 181301 (2004).

[13] J. N. Bahcall, A. M. Serenelli, and S. Basu, astro-ph/0412440.

[14] S. Turck-Chièze *et al.*, Phys. Rev. Lett. **93**, 221102 (2004). The tac A model flux has been re-scaled using the updated cross section, as described for the seismic model in this reference.

[15] Z. Maki, N. Nakagawa, and S. Sakata, Prog. Theor. Phys. **28** 870 (1962); V. Gribov and B. Pontecorvo, Phys. Lett. **B28** 493 (1969).

[16] S. P. Mikheyev and A. Yu. Smirnov, Sov. J. Nucl. Phys. **42** 913 (1985); L. Wolfenstein, Phys. Rev. **D17** 2369 (1978).

[17] K. Eguchi *et al.*, Phys. Rev. Lett. **90**, 021802 (2003).

[18] H. H. Chen, Phys. Rev. Lett. **55**, 1534 (1985).

[19] W. R. Nelson, H. Hirayama and D. W. O. Rogers, *The EGS4 Code System*, SLAC report 265 (1985).

[20] *MCNP4A, A Monte Carlo N-Particle Transport Code System*, Radiation Shielding Information Center, Los Alamos National Laboratory, Los Alamos, Nov. 1993 (unpublished).

[21] A. Fasso, A. Ferrari, J. Ranft, P. R. Sala, in the Proceedings of the International Conference on Advanced Monte Carlo for Radiation Physics, Particle Transport Simulation and Applications (MC 2000) Conference, Lisbon, October 23–26 2000, A. Kling, F. Barao, M. Nakagawa, L. Tavora, P. Vaz eds., Springer-Verlag Berlin, p. 955-960 (2001).

[22] N. J. Tagg *et al.*, Nucl. Instr. and Meth. **A489**, 178 (2002).

[23] M. R. Dragowsky *et al.*, Nucl. Instr. and Meth. **A481**, 284 (2002).

[24] A. W. P. Poon *et al.*, Nucl. Instr. and Meth. **A452**, 115 (2000).

[25] J. C. Zwinkels, W. F. Davidson and C. X. Dodd, Applied Optics **29** 3240 (1990)

[26] E. D. Earle, Summary Report on Acrylic Vessel, SNO Internal Report **005** (1998)

[27] H. A. Bethe, Phys. Rev. **89**, 1256 (1953).

[28] N. F. Mott, Proc. Roy. Soc. **A 124**, 425 (1929).

[29] W. A. McKinley and H. Feshbach, Phys. Rev. **74**, 1759 (1948).

[30] I. Kawrakow and D. W. O. Rogers, *The EGSnrc Code System: Monte Carlo simulation of electron and photon transport*, Technical Report PIRS-701, National Research Council of Canada, Ottawa, Canada (2000). We thank Dave Rogers for running the EGSnrc code.

[31] E. J. Axton, BCNM Report GE/PH/01/86, June (1986); Nucl. Stand. Ref. Data, **214** (1985).

[32] An example of using bifurcated analysis in a rare decay search can be found in P. C. Bergbusch, Ph.D. dissertation, University of British Columbia (2000).

[33] T. C. Andersen *et al.*, Nucl. Instr. and Meth. **A501**, 399 (2003).

[34] T. C. Andersen *et al.*, Nucl. Instr. and Meth. **A501**, 386 (2003).

[35] I. Blevis *et al.*, Nucl. Instr. and Meth. **A517**, 139 (2004).

[36] D. Casper, Nucl. Phys. Proc. Suppl. **112**, 161 (2002).

[37] L. C. Stonehill, J. A. Formaggio and R. G. H. Robertson, Phys. Rev. **C69**, 015801 (2004).

[38] C. E. Ortiz *et al.*, Phys. Rev. Lett. **85**, 2909 (2000).

[39] M. Butler, J. W. Chen and X. Kong, Phys. Rev. **C63**, 035501 (2001).

[40] S. Nakamura, T. Sato, V. Gudkov and K. Kubodera, Phys. Rev. **C63**, 034617 (2001).

[41] S. Nakumura *et al.*, Nucl. Phys. **A707**, 561 (2002).

[42] J. F. Beacom and S. J. Parke, Phys. Rev. **D64**, 091302 (2001).

[43] K. Hagiwara *et al.*, Phys. Rev. **D66**, 010001 (2002).

[44] A. Kurylov *et al.*, Phys. Rev. **C65**, 055501 (2002).

[45] Cross section uncertainty includes: $g_A$ (0.5%), theoretical cross section (1% for CC and NC, 0.3% for CC/NC [41]) and radiative corrections (0.3% for CC, 0.1% for NC).

[46] *hep* neutrinos could also be present in the measured fluxes; a contribution of $9.3 \times 10^3$ cm$^{-2}$ s$^{-1}$ has been assumed here.

[47] Electron neutrino cross sections are used to calculate all fluxes.

[48] S. P. Mikheyev and A. Y. Smirnov, in '*86 Massive Neutrinos in Astrophysics and in Particle Physics, Proceedings of the Moriond Workshop*, edited by O. Fackler and J. Tran Thanh Van (1986), vol. Editions Frontières, Gif-sur-Yvette, 1986, p. 335.

[49] A. J. Baltz and J. Weneser, Phys. Rev. **D37**, 3364 (1988).

[50] E. Kh. Akhmedov, M. A. Tortola, and J. W. F. Valle, JHEP **05**, 057 (2004).

[51] M. Blennow, T. Ohlsson, and H. Snellman, Phys. Rev. **D69**, 073006 (2004).

[52] M. C. Gonzalez-Garcia, C. Peña-Garay and A. Y. Smirnov, Phys. Rev. **D63**, 113004 (2001).

[53] A. Bandyopadhyay, S. Choubey, S. Goswami, S. T. Petcov, and D. P. Roy, Phys. Lett. **B583**, 134 (2004).

[54] E. Lisi, and D. Montanino, Phys. Rev. **D56**, 1792 (1803).

[55] M. Smy *et al.*, Phys. Rev. **D69**, 011104 (2004).

[56] J.N. Bahcall and C. Peña-Garay, JHEP **11**, 004 (2003); J.N. Bahcall, M.C. Gonzalez-Garcia and C. Peña-Garay, JHEP **08**, 016 (2004).

[57] A. B. Balantekin and H. Yüksel, Phys. Rev. **D68**, 113002 (2003).

[58] G. L. Fogli *et al.*, Phys. Rev. **D66**, 053010 (2002).

[59] P.C. de Holanda and A.Yu. Smirnov, Astropart. Phys. **21**, 287 (2004).

[60] P. Aliani *et al.*, Phys. Rev. D **69**, 013005 (2004).

[61] T. Araki *et al.*, arXiv:hep-ex/0406035.

[62] http://sno.phy.queensu.ca/sno/prlwebpage/

[63] J.N. Bahcall *et al.*, Phys. Rev. C **54**, 411 (1996).

[64] G. L. Fogli and E. Lisi, Astropart. Phys. **3**, 185 (1995).

## APPENDIX A: SNO DATA IN AN OSCILLATION ANALYSIS

The following tables contain a subset of SNO's salt phase results and some supporting information that may be needed in a neutrino oscillation analysis. The values in these tables include outputs from the signal extraction (described earlier in this paper) and results from systematic uncertainty studies. Day and night values were extracted separately without any constraints on the NC rate asymmetry or energy spectrum shapes.

Table XXX contains day and night CC spectra, expressed as fluxes. The meaning of these fluxes (for example the day flux in the 6.0–6.5 MeV bin of $0.182 \times 10^6$ cm$^{-2}$ s$^{-1}$) is that the number of events SNO observed in the salt day data set attributed to CC interactions by the signal extraction, with an electron kinetic energy between 6.0–6.5 MeV, is equal to the number of all CC events that would be observed above kinetic energy 5.5 MeV, if the integral flux (from zero to endpoint) of $\nu_e$ had the value of $0.182 \times 10^6$ cm$^{-2}$ s$^{-1}$ and had an undistorted $^8$B spectral shape [38]. The $^8$B spectral shape aspect of this definition is only for normalization. There is no assumption of any spectral shape when extracting the actual number of events in each bin for SNO's salt phase. This normalization was chosen so that the sum of the values for all bins equals the integral day and night $^8$B fluxes quoted in Section XII B.

When calculating the theoretical CC flux and spectra for a set of oscillation parameters, for comparison with SNO data, one should be aware of the above definition. Thus, a model prediction for the value in the above mentioned example bin would be:

$$\int_0^\infty \phi(E_\nu)\, dE_\nu \; \frac{\int_0^\infty \int_0^\infty \int_{6.0}^{6.5} \phi(E_\nu) P_{ee}(E_\nu)\frac{d\sigma}{dT_e}(E_\nu, T_e)R(T_e, T_{\text{eff}})\, dE_\nu\, dT_e\, dT_{\text{eff}}}{\int_0^\infty \int_0^\infty \int_{5.5}^\infty \phi(E_\nu)\frac{d\sigma}{dT_e}(E_\nu, T_e)R(T_e, T_{\text{eff}})\, dE_\nu\, dT_e\, dT_{\text{eff}}} \tag{A1}$$

where $P_{ee}$ is the survival probability for a $\nu_e$ produced in the Sun to be detected as a $\nu_e$, $\phi(E_\nu)$ is the flux of $^8$B solar neutrinos as a function of neutrino energy, $\frac{d\sigma}{dT_e}$ is the differential cross section for the CC reaction and $R(T_e, T_{\text{eff}})$ is the energy response function,

$$R(T_e, T_{\text{eff}}) = \frac{1}{\sqrt{2\pi}\sigma_T} \exp\left[-\frac{(T_e - T_{\text{eff}})^2}{2\sigma_T^2}\right], \tag{A2}$$

and $T_e$ is the true recoil electron kinetic energy and $T_{\text{eff}}$ is the observed electron kinetic energy, with resolution,

$$\sigma_T(T_e) = -0.131 + 0.383\sqrt{T_e} + 0.03731\, T_e \tag{A3}$$

in units of MeV.

Tables XXXII and XXXIII contain the statistical correlation coefficients from SNO signal extraction, for salt phase day and night data respectively. The numbering of the CC spectral bins listed in these tables follows the ordering of energy bins as listed in Table XXX. These correlation coefficients are necessary to include in an oscillation analysis that includes SNO CC spectral information.

The systematic uncertainties for the SNO extracted CC spectrum are listed in Table XXXIV. These uncertainties (in percent) can be used as the partial derivatives in a bin-to-bin correlated systematics part of a $\chi^2$ calculation, as described in Section XIII. The spectral shape of these uncertainties can also be used as the shape of the related day-night asymmetry systematic. The magnitude of a day-night spectral systematic can be estimated by taking the ratio of the size of the day-night flux asymmetry uncertainty and the total flux uncertainty, for each relevant systematic, and using this ratio in each bin to scale that spectral systematic. Note that NC-only systematics (internal neutron background and neutron capture efficiency uncertainties) are not listed in Table XXXIV since they do not affect the CC spectrum, but are necessary to include in an oscillation analysis and can be found in Table XIX.

Table XXXI contains the live time distribution for SNO's 391-day salt data set as a function of cosine of the zenith angle of the Sun. For detailed calculations of neutrino survival probabilities including propagation through the Earth, the live times at different zenith angles can be used as weighting factors.

TABLE XXX: Charged-current reaction recoil electron kinetic energy spectra from the 391-day SNO salt phase, expressed in units of equivalent $^8$B fluxes. The normalization is such that the sum over all bins equals the day or night integral $^8$B solar neutrino flux above 0 MeV, as determined and quoted in Section XII B. Day and night extracted values are listed with their statistical uncertainties from SNO's signal extraction.

| CC electron kinetic energy bin (MeV) | salt phase day $(10^6 \text{ cm}^{-2} \text{ s}^{-1})$ | salt phase night $(10^6 \text{ cm}^{-2} \text{ s}^{-1})$ |
|---|---|---|
| 5.5–6.0 | 0.205 ± 0.032 | 0.145 ± 0.027 |
| 6.0–6.5 | 0.182 ± 0.030 | 0.164 ± 0.027 |
| 6.5–7.0 | 0.153 ± 0.028 | 0.190 ± 0.026 |
| 7.0–7.5 | 0.226 ± 0.028 | 0.180 ± 0.024 |
| 7.5–8.0 | 0.198 ± 0.025 | 0.178 ± 0.022 |
| 8.0–8.5 | 0.184 ± 0.023 | 0.164 ± 0.019 |
| 8.5–9.0 | 0.124 ± 0.018 | 0.114 ± 0.015 |
| 9.0–9.5 | 0.099 ± 0.015 | 0.126 ± 0.015 |
| 9.5–10.0 | 0.110 ± 0.015 | 0.124 ± 0.014 |
| 10.0–10.5 | 0.058 ± 0.011 | 0.067 ± 0.010 |
| 10.5–11.0 | 0.070 ± 0.012 | 0.073 ± 0.011 |
| 11.0–11.5 | 0.048 ± 0.010 | 0.039 ± 0.007 |
| 11.5–12.0 | 0.042 ± 0.008 | 0.029 ± 0.007 |
| 12.0–12.5 | 0.0088 ± 0.0038 | 0.018 ± 0.005 |
| 12.5–13.0 | 0.0082 ± 0.0040 | 0.015 ± 0.005 |
| 13.0–13.5 | 0.0025 ± 0.0028 | 0.0042 ± 0.0025 |
| 13.5–20.0 | 0.014 ± 0.005 | 0.012 ± 0.004 |

TABLE XXXI: Zenith-live time distribution for the 391-day SNO salt phase data set. There are sixty equally-spaced bins in $\cos \theta_z$ with $\theta_z$ being the zenith angle of the Sun (e.g., $\cos \theta_z = -1$ would be the value if the Sun was directly below the SNO detector). The amount of live time in each bin is listed in seconds. The bins start from $\cos \theta_z = -1$ to -0.9667 at the top left of the table and increase going down the column. Continuing at the top of the second column, the top bin has $\cos \theta_z = -0.5$ to -0.4667. The first two columns contain night live times while the final two columns are day live times.

| $\cos \theta_z$ | | | |
|---|---|---|---|
| −1.0 to −0.5 | −0.5 to 0.0 | 0.0 to 0.5 | 0.5 to 1.0 |
| 0 | 705975 | 606806 | 493795 |
| 0 | 743962 | 608735 | 471616 |
| 432202 | 761182 | 606873 | 447927 |
| 545975 | 814881 | 607682 | 445073 |
| 592399 | 1107970 | 616573 | 473089 |
| 566033 | 887601 | 617365 | 491700 |
| 570422 | 777241 | 625955 | 453238 |
| 539112 | 728515 | 651235 | 458976 |
| 527208 | 698101 | 682766 | 466092 |
| 571086 | 672856 | 752869 | 449265 |
| 594019 | 652494 | 844742 | 433395 |
| 613845 | 639256 | 633145 | 388327 |
| 622530 | 624127 | 576052 | 255268 |
| 672151 | 615141 | 570776 | 0 |
| 684213 | 608656 | 521223 | 0 |

TABLE XXXII: Statistical correlation coefficients from SNO's signal extraction for the salt phase day data. The numbering of the CC spectral bins follows the ordering of energy bins in Table XXX.

| | NC | CC1 | CC2 | CC3 | CC4 | CC5 | CC6 | CC7 | CC8 | CC9 | CC10 | CC11 | CC12 | CC13 | CC14 | CC15 | CC16 | CC17 | ES |
|---|---|---|---|---|---|---|---|---|---|---|---|---|---|---|---|---|---|---|---|
| NC | 1.0000 | -0.3478 | -0.3320 | -0.3281 | -0.2488 | -0.2000 | -0.1555 | -0.0877 | -0.0618 | -0.0329 | -0.0152 | -0.0063 | -0.0025 | 0.0003 | -0.0000 | -0.0000 | -0.0000 | -0.0000 | -0.0610 |
| CC1 | -0.3478 | 1.0000 | 0.1528 | 0.1440 | 0.1124 | 0.0865 | 0.0676 | 0.0425 | 0.0272 | 0.0135 | 0.0061 | 0.0030 | 0.0011 | 0.0001 | 0.0000 | -0.0000 | 0.0000 | 0.0000 | -0.0695 |
| CC2 | -0.3320 | 0.1528 | 1.0000 | 0.1459 | 0.1147 | 0.0873 | 0.0684 | 0.0440 | 0.0275 | 0.0135 | 0.0061 | 0.0031 | 0.0011 | 0.0001 | 0.0000 | -0.0000 | 0.0000 | 0.0000 | -0.0507 |
| CC3 | -0.3281 | 0.1440 | 0.1459 | 1.0000 | 0.1073 | 0.0824 | 0.0644 | 0.0407 | 0.0259 | 0.0129 | 0.0058 | 0.0029 | 0.0010 | 0.0001 | 0.0000 | -0.0000 | 0.0000 | 0.0000 | -0.0525 |
| CC4 | -0.2488 | 0.1124 | 0.1147 | 0.1073 | 1.0000 | 0.0643 | 0.0503 | 0.0322 | 0.0202 | 0.0100 | 0.0045 | 0.0023 | 0.0008 | 0.0001 | -0.0000 | -0.0000 | 0.0000 | -0.0000 | -0.0556 |
| CC5 | -0.2000 | 0.0865 | 0.0873 | 0.0824 | 0.0643 | 1.0000 | 0.0387 | 0.0243 | 0.0155 | 0.0078 | 0.0035 | 0.0017 | 0.0006 | 0.0000 | -0.0000 | 0.0000 | 0.0000 | 0.0000 | -0.0637 |
| CC6 | -0.1555 | 0.0676 | 0.0684 | 0.0644 | 0.0503 | 0.0387 | 1.0000 | 0.0190 | 0.0122 | 0.0061 | 0.0027 | 0.0014 | 0.0005 | 0.0000 | 0.0000 | 0.0000 | 0.0000 | 0.0000 | -0.0648 |
| CC7 | -0.0877 | 0.0425 | 0.0440 | 0.0407 | 0.0322 | 0.0243 | 0.0190 | 1.0000 | 0.0077 | 0.0037 | 0.0017 | 0.0009 | 0.0003 | 0.0000 | 0.0000 | 0.0000 | 0.0000 | 0.0000 | -0.0595 |
| CC8 | -0.0618 | 0.0272 | 0.0275 | 0.0259 | 0.0202 | 0.0155 | 0.0122 | 0.0077 | 1.0000 | 0.0024 | 0.0011 | 0.0005 | 0.0002 | 0.0000 | 0.0000 | 0.0000 | 0.0000 | 0.0000 | -0.0430 |
| CC9 | -0.0329 | 0.0135 | 0.0135 | 0.0129 | 0.0100 | 0.0078 | 0.0061 | 0.0037 | 0.0024 | 1.0000 | 0.0006 | 0.0003 | 0.0001 | 0.0000 | 0.0000 | 0.0000 | 0.0000 | -0.0000 | -0.0495 |
| CC10 | -0.0152 | 0.0061 | 0.0061 | 0.0058 | 0.0045 | 0.0035 | 0.0027 | 0.0017 | 0.0011 | 0.0006 | 1.0000 | 0.0001 | 0.0000 | 0.0000 | 0.0000 | -0.0000 | -0.0000 | 0.0000 | -0.0466 |
| CC11 | -0.0063 | 0.0030 | 0.0031 | 0.0029 | 0.0023 | 0.0017 | 0.0014 | 0.0009 | 0.0005 | 0.0003 | 0.0001 | 1.0000 | 0.0000 | 0.0000 | 0.0000 | 0.0000 | 0.0000 | 0.0000 | -0.0487 |
| CC12 | -0.0025 | 0.0011 | 0.0011 | 0.0010 | 0.0008 | 0.0006 | 0.0005 | 0.0003 | 0.0002 | 0.0001 | 0.0000 | 0.0000 | 1.0000 | 0.0000 | 0.0000 | 0.0000 | -0.0000 | 0.0000 | -0.0570 |
| CC13 | 0.0003 | 0.0001 | 0.0001 | 0.0001 | 0.0001 | 0.0000 | 0.0000 | 0.0000 | 0.0000 | 0.0000 | 0.0000 | 0.0000 | 0.0000 | 1.0000 | 0.0000 | -0.0000 | -0.0000 | -0.0000 | 0.0000 |
| CC14 | -0.0000 | 0.0000 | 0.0000 | 0.0000 | -0.0000 | -0.0000 | 0.0000 | 0.0000 | 0.0000 | 0.0000 | 0.0000 | 0.0000 | 0.0000 | 0.0000 | 1.0000 | -0.0000 | -0.0000 | -0.0000 | -0.0000 |
| CC15 | -0.0000 | -0.0000 | -0.0000 | -0.0000 | -0.0000 | 0.0000 | 0.0000 | 0.0000 | 0.0000 | 0.0000 | -0.0000 | 0.0000 | 0.0000 | -0.0000 | -0.0000 | 1.0000 | 0.0000 | 0.0000 | -0.0163 |
| CC16 | -0.0000 | 0.0000 | 0.0000 | 0.0000 | 0.0000 | 0.0000 | 0.0000 | 0.0000 | 0.0000 | 0.0000 | -0.0000 | 0.0000 | -0.0000 | -0.0000 | -0.0000 | 0.0000 | 1.0000 | -0.0000 | -0.0379 |
| CC17 | -0.0000 | 0.0000 | 0.0000 | 0.0000 | -0.0000 | 0.0000 | 0.0000 | 0.0000 | 0.0000 | -0.0000 | 0.0000 | 0.0000 | 0.0000 | -0.0000 | -0.0000 | 0.0000 | -0.0000 | 1.0000 | 0.0000 |
| ES | -0.0610 | -0.0695 | -0.0507 | -0.0525 | -0.0556 | -0.0637 | -0.0648 | -0.0595 | -0.0430 | -0.0495 | -0.0466 | -0.0487 | -0.0570 | 0.0000 | -0.0000 | -0.0163 | -0.0379 | 0.0000 | 1.0000 |

TABLE XXXIII: Statistical correlation coefficients from SNO's signal extraction for the salt phase night data. The numbering of the CC spectral bins follows the ordering of energy bins in Table XXX.

| | NC | CC1 | CC2 | CC3 | CC4 | CC5 | CC6 | CC7 | CC8 | CC9 | CC10 | CC11 | CC12 | CC13 | CC14 | CC15 | CC16 | CC17 | ES |
|---|---|---|---|---|---|---|---|---|---|---|---|---|---|---|---|---|---|---|---|
| NC | 1.0000 | -0.3485 | -0.3437 | -0.3060 | -0.2669 | -0.2089 | -0.1571 | -0.1034 | -0.0545 | -0.0317 | -0.0138 | -0.0067 | -0.0010 | -0.0008 | 0.0001 | 0.0000 | 0.0000 | 0.0000 | -0.0693 |
| CC1 | -0.3485 | 1.0000 | 0.1580 | 0.1400 | 0.1201 | 0.0967 | 0.0671 | 0.0477 | 0.0237 | 0.0143 | 0.0085 | 0.0027 | 0.0017 | 0.0003 | 0.0000 | -0.0000 | -0.0000 | -0.0000 | -0.0684 |
| CC2 | -0.3437 | 0.1580 | 1.0000 | 0.1379 | 0.1183 | 0.0952 | 0.0661 | 0.0469 | 0.0234 | 0.0141 | 0.0084 | 0.0027 | 0.0016 | 0.0003 | 0.0000 | -0.0000 | -0.0000 | -0.0000 | -0.0463 |
| CC3 | -0.3060 | 0.1400 | 0.1379 | 1.0000 | 0.1048 | 0.0843 | 0.0586 | 0.0416 | 0.0207 | 0.0125 | 0.0074 | 0.0024 | 0.0014 | 0.0002 | 0.0000 | -0.0000 | -0.0000 | -0.0000 | -0.0743 |
| CC4 | -0.2669 | 0.1201 | 0.1183 | 0.1048 | 1.0000 | 0.0723 | 0.0505 | 0.0357 | 0.0178 | 0.0107 | 0.0062 | 0.0020 | 0.0012 | 0.0002 | 0.0000 | -0.0000 | -0.0000 | -0.0000 | -0.0527 |
| CC5 | -0.2089 | 0.0967 | 0.0952 | 0.0843 | 0.0723 | 1.0000 | 0.0404 | 0.0287 | 0.0143 | 0.0086 | 0.0051 | 0.0016 | 0.0010 | 0.0002 | 0.0000 | -0.0000 | -0.0000 | -0.0000 | -0.0483 |
| CC6 | -0.1571 | 0.0671 | 0.0661 | 0.0586 | 0.0505 | 0.0404 | 1.0000 | 0.0199 | 0.0101 | 0.0060 | 0.0033 | 0.0012 | 0.0006 | 0.0001 | -0.0000 | 0.0000 | -0.0000 | 0.0000 | -0.0489 |
| CC7 | -0.1034 | 0.0477 | 0.0469 | 0.0416 | 0.0357 | 0.0287 | 0.0199 | 1.0000 | 0.0070 | 0.0042 | 0.0025 | 0.0008 | 0.0005 | 0.0001 | 0.0000 | 0.0000 | 0.0000 | 0.0000 | -0.0417 |
| CC8 | -0.0545 | 0.0237 | 0.0234 | 0.0207 | 0.0178 | 0.0143 | 0.0101 | 0.0070 | 1.0000 | 0.0021 | 0.0012 | 0.0004 | 0.0002 | 0.0000 | 0.0000 | 0.0000 | -0.0000 | 0.0000 | -0.0692 |
| CC9 | -0.0317 | 0.0143 | 0.0141 | 0.0125 | 0.0107 | 0.0086 | 0.0060 | 0.0042 | 0.0021 | 1.0000 | 0.0007 | 0.0002 | 0.0001 | 0.0000 | 0.0000 | 0.0000 | -0.0000 | 0.0000 | -0.0410 |
| CC10 | -0.0138 | 0.0085 | 0.0084 | 0.0074 | 0.0062 | 0.0051 | 0.0033 | 0.0025 | 0.0012 | 0.0007 | 1.0000 | 0.0001 | 0.0001 | 0.0000 | 0.0000 | -0.0000 | -0.0000 | -0.0000 | 0.0016 |
| CC11 | -0.0067 | 0.0027 | 0.0027 | 0.0024 | 0.0020 | 0.0016 | 0.0012 | 0.0008 | 0.0004 | 0.0002 | 0.0001 | 1.0000 | 0.0000 | 0.0000 | -0.0000 | -0.0000 | -0.0000 | -0.0000 | -0.0359 |
| CC12 | -0.0010 | 0.0017 | 0.0016 | 0.0014 | 0.0012 | 0.0010 | 0.0006 | 0.0005 | 0.0002 | 0.0001 | 0.0001 | 0.0000 | 1.0000 | 0.0000 | -0.0000 | -0.0000 | -0.0000 | -0.0000 | 0.0003 |
| CC13 | -0.0008 | 0.0003 | 0.0003 | 0.0002 | 0.0002 | 0.0002 | 0.0001 | 0.0001 | 0.0000 | 0.0000 | 0.0000 | 0.0000 | 0.0000 | 1.0000 | 0.0000 | 0.0000 | -0.0000 | 0.0000 | -0.0229 |
| CC14 | 0.0001 | 0.0000 | 0.0000 | 0.0000 | 0.0000 | 0.0000 | -0.0000 | 0.0000 | 0.0000 | 0.0000 | 0.0000 | -0.0000 | 0.0000 | 0.0000 | 1.0000 | -0.0000 | -0.0000 | -0.0000 | -0.0139 |
| CC15 | 0.0000 | -0.0000 | -0.0000 | -0.0000 | -0.0000 | -0.0000 | 0.0000 | 0.0000 | 0.0000 | 0.0000 | -0.0000 | -0.0000 | -0.0000 | 0.0000 | -0.0000 | 1.0000 | -0.0000 | -0.0000 | -0.0188 |
| CC16 | 0.0000 | -0.0000 | -0.0000 | -0.0000 | -0.0000 | -0.0000 | -0.0000 | 0.0000 | -0.0000 | -0.0000 | -0.0000 | -0.0000 | -0.0000 | -0.0000 | -0.0000 | -0.0000 | 1.0000 | 0.0000 | -0.0085 |
| CC17 | 0.0000 | -0.0000 | -0.0000 | -0.0000 | -0.0000 | -0.0000 | 0.0000 | 0.0000 | 0.0000 | 0.0000 | -0.0000 | -0.0000 | -0.0000 | 0.0000 | -0.0000 | -0.0000 | 0.0000 | 1.0000 | -0.0183 |
| ES | -0.0693 | -0.0684 | -0.0463 | -0.0743 | -0.0527 | -0.0483 | -0.0489 | -0.0417 | -0.0692 | -0.0410 | 0.0016 | -0.0359 | 0.0003 | -0.0229 | -0.0139 | -0.0188 | -0.0085 | -0.0183 | 1.0000 |

TABLE XXXIV: Complete CC spectrum systematic uncertainties (in percent) from SNO's unconstrained fit signal extraction of the 391-day salt phase data set. The numbering of the CC spectral bins follows the ordering of energy bins in Table XXX.

| Uncertainty | NC | ES | CC1 | CC2 | CC3 | CC4 | CC5 | CC6 | CC7 | CC8 |
|---|---|---|---|---|---|---|---|---|---|---|
| Energy scale (const.) | 3.8, -3.3 | 1.9, -1.6 | -8.0, 9.5 | -5.9, 6.2 | -2.9, 3.0 | 0.6, 0.0 | 1.7, -1.8 | 2.9, -3.9 | 3.9, -3.6 | 4.7, -5.0 |
| Energy scale (E dep.) | 0.1, -0.1 | 0.1, -0.1 | -1.5, 1.6 | -1.4, 1.6 | -1.6, 1.2 | -0.4, 0.6 | -0.5, 0.6 | 0.0, -0.4 | 0.9, -0.6 | 1.3, -0.4 |
| Energy radial bias | 2.1, -2.0 | 1.2, -1.1 | -5.7, 6.1 | -4.3, 4.2 | -2.1, 2.0 | 0.1, -0.1 | 1.0, -1.2 | 1.5, -2.5 | 3.6, -3.9 | 3.8, -2.9 |
| Energy resolution | 0.8, -0.8 | 0.7, -0.7 | 4.9, -4.9 | 2.1, -2.1 | 1.8, -1.8 | 0.1, -0.1 | -1.2, 1.2 | -1.8, 1.8 | -3.9, 3.9 | -2.6, 2.6 |
| $\beta_{14}$ mean | -3.6, 4.5 | 1.3, -1.2 | 7.1, -8.4 | 7.0, -8.3 | 6.3, -7.9 | 4.4, -4.6 | 3.3, -4.0 | 2.3, -2.9 | 2.6, -2.9 | 1.1, -1.7 |
| $\beta_{14}$ width | 0.0, 0.0 | 0.2, -0.2 | -0.9, -0.1 | -0.7, 0.0 | -0.8, -0.3 | 0.0, -0.2 | -0.2, -0.2 | 0.0, -0.2 | -0.1, 0.3 | 0.3, -0.2 |
| Radial scale (const.) | -3.0, 3.3 | -2.6, 3.0 | -2.6, 2.5 | -3.4, 2.3 | -1.7, 2.4 | -2.4, 2.6 | -2.5, 2.3 | -2.8, 2.4 | -2.6, 2.9 | -2.5, 2.8 |
| Radial scale (E dep.) | -0.6, 0.5 | -0.7, 0.8 | 0.2, -0.2 | -0.4, 0.4 | -0.9, 0.9 | -1.2, 1.2 | -1.5, 1.5 | -1.7, 1.7 | -2.0, 2.0 | -2.1, 2.1 |
| Vertex $x$ | 0.0, -0.0 | 0.1, -0.1 | -0.3, 0.0 | -0.2, -0.5 | -0.3, 0.0 | -0.5, 0.0 | -0.1, 0.0 | -0.2, -0.1 | -0.1, -0.1 | 0.1, -0.1 |
| Vertex $y$ | 0.0, -0.1 | 0.1, -0.1 | -0.2, -0.3 | 0.0, -0.2 | 0.1, -0.1 | -0.2, 0.0 | 0.1, 0.0 | -0.3, 0.0 | 0.0, -0.3 | 0.1, 0.4 |
| Vertex $z$ | -0.2, 0.2 | 0.0, 0.0 | -0.4, -0.2 | -0.9, -0.6 | 0.4, 0.1 | 0.2, -0.6 | 0.0, -0.3 | 0.0, -0.1 | 0.5, -0.2 | -0.3, -0.1 |
| Vertex resolution | 0.1, -0.1 | 0.1, -0.1 | -0.4, 0.4 | -0.2, 0.2 | 1.4, -1.4 | -0.3, 0.3 | 0.1, -0.1 | -0.6, 0.6 | 0.0, 0.0 | 0.4, -0.4 |
| Angular resolution | -0.2, 0.2 | 5.1, -5.1 | -0.2, 0.2 | 0.4, -0.4 | 0.2, -0.2 | 0.1, -0.1 | -0.2, 0.2 | 0.0, 0.0 | 0.0, 0.0 | -0.6, 0.6 |
| Internal $\gamma$ | 0.0, -0.1 | 0.0, -0.0 | 0.4, -0.6 | 0.3, -0.4 | 0.2, -0.2 | 0.1, -0.1 | 0.0, 0.0 | 0.0, 0.0 | 0.0, 0.0 | 0.0, 0.0 |
| Selection efficiency | -0.1, 0.2 | -0.2, 0.2 | -0.2, 0.2 | -0.1, 0.2 | -0.1, 0.2 | -0.1, 0.2 | -0.1, 0.2 | -0.1, 0.2 | -0.1, 0.2 | -0.1, 0.2 |
| Backgrounds | -1.0, 0.0 | -0.0, 0.0 | -8.5, 0.0 | -0.1, 0.0 | -0.1, 0.0 | -0.1, 0.0 | -0.1, 0.0 | -0.1, 0.0 | -0.1, 0.0 | -0.1, 0.0 |

| | CC9 | CC10 | CC11 | CC12 | CC13 | CC14 | CC15 | CC16 | CC17 |
|---|---|---|---|---|---|---|---|---|---|
| Energy scale (const.) | 5.0, -4.2 | 6.2, -6.7 | 6.7, -5.8 | 9.6, -7.4 | 7.0, -6.7 | 17.6, -9.7 | 16.6, -17.4 | 18.2, -10.2 | 20.5, -17.5 |
| Energy scale (E dep.) | 0.7, -0.8 | 1.3, -2.0 | 2.3, -2.3 | 3.9, -2.5 | 2.5, -2.0 | 9.3, -5.1 | 9.1, -11.9 | 13.8, -8.8 | 14.1, -12.2 |
| Energy radial bias | 2.8, -3.1 | 4.1, -4.3 | 4.7, -4.2 | 7.0, -4.5 | 5.7, -4.7 | 12.4, -6.6 | 11.8, -14.6 | 13.5, -10.3 | 13.2, -12.3 |
| Energy resolution | -0.7, 0.7 | 0.0, 0.0 | -2.1, 2.1 | 0.6, -0.6 | -2.3, 2.3 | -5.8, 5.8 | -14.8, 14.8 | -9.9, 9.9 | -17.2, 17.2 |
| $\beta_{14}$ mean | 0.6, -0.4 | 0.2, 0.4 | -0.1, -0.1 | 1.4, -0.1 | 0.3, 0.1 | -1.0, 4.4 | 2.2, -1.4 | -5.9, 9.0 | 3.8, -2.1 |
| $\beta_{14}$ width | 0.0, -0. | -0.3, 0.6 | 0.0, 0.2 | 0.0, 0.2 | -0.4, 0.0 | -0.5, 1.9 | 0.5, -0.1 | -0.1, 6.5 | -0.2, -0.2 |
| Radial scale (const.) | -2.8, 3.5 | -2.0, 2.0 | -2.2, 1.9 | -1.7, 2.4 | -2.4, 3.7 | -2.5, 5.6 | -12.6, 3.9 | -0.4, -1.4 | -2.8, 2.9 |
| Radial scale (E dep.) | -2.2, 2.2 | -2.3, 2.5 | -2.5, 2.7 | -2.7, 2.9 | -2.9, 3.1 | -3.1, 3.3 | -3.3, 3.5 | -3.6, 3.8 | -3.9, 4.3 |
| Vertex $x$ | -0.1, -0.1 | 0.0, -0.5 | -0.1, 0.3 | -0.2, 0.0 | 0.7, -0.4 | 0.2, -0.2 | -1.2, 0.0 | -0.9, -0.6 | -0.2, 0.5 |
| Vertex $y$ | 0.0, 0.1 | 0.5, -0.2 | 0.0, 0.0 | 0.5, 0.0 | 0.0, 0.3 | 0.5, -0.1 | -0.5, 0.2 | -1.3, -0.4 | -0.1, 0.1 |
| Vertex $z$ | 0.7, 0.0 | -0.2, -0.3 | 0.1, -0.3 | 0.7, 0.1 | 0.8, -1.0 | 0.5, 1.3 | -1.2, 1.0 | -2.4, 1.0 | 0.1, -0.9 |
| Vertex resolution | 0.0, 0.0 | -0.2, 0.2 | 0.1, -0.1 | -0.1, 0.1 | 1.0, -1.0 | 3.3, -3.3 | -8.7, 8.7 | -4.1, 4.1 | 0.8, -0.8 |
| Angular resolution | 0.0, 0.0 | -0.6, 0.6 | -0.7, 0.7 | -0.8, 0.8 | -0.8, 0.8 | 0.3, -0.3 | 0.5, -0.5 | 0.4, -0.4 | 0.0, 0.0 |
| Internal $\gamma$ | 0.0, 0.0 | 0.0, 0.0 | 0.0, 0.0 | 0.0, 0.0 | 0.0, 0.0 | 0.0, 0.0 | 0.0, 0.0 | 0.0, 0.0 | 0.0, 0.0 |
| Selection efficiency | -0.1, 0.2 | -0.2, 0.2 | -0.2, 0.2 | -0.2, 0.2 | -0.2, 0.2 | -0.2, 0.2 | -0.2, 0.2 | -0.2, 0.2 | -0.3, 0.3 |
| Backgrounds | -0.1, 0.0 | -0.2, 0.0 | -0.2, 0.0 | -0.3, 0.0 | -0.3, 0.0 | -0.9, 0.0 | -0.9, 0.0 | -3.2, 0.0 | -12.3, 0.0 |